

Analysis of the flight characteristics of a highly swept cranked flying wing by means of an experimental test

Thesis Report

R.A. Viet

Delft University of Technology



Analysis of the flight characteristics of a highly swept cranked flying wing by means of an experimental test

Thesis Report

by

R.A. Viet

in partial fulfilment of the requirements for the degree of

Master of Science
in Aerospace Engineering

at the Delft University of Technology,
to be defended publicly on Thursday the 28th of March, 2019 at 1:00 PM.

Student number: 4142004

Project duration: March, 2018 – March, 2019

Supervisors: Dr. ir. R. Vos, Delft University of Technology
Ir. A. Raju Kulkarni, Delft University of Technology

Thesis committee: Prof. dr. ing. G. Eitelberg, Delft University of Technology
Dr. ir. R. Vos, Delft University of Technology
Ir. W.A. Timmer, Delft University of Technology

An electronic version of this thesis is available at <http://repository.tudelft.nl/>.

Abstract

The Flying V is a concept proposed and patented by Benad and Airbus Operations GmbH, which is a flying wing aircraft in the shape of the letter V. Multiple researches already showed promising results, with a 25% increased lift over drag ratio compared to conventional aircraft like the Airbus A350-900. Before research of sub-scale flight testing can be conducted, research into the flight characteristics is necessary. Based on the identification of the problems, the research question for the thesis research is defined as: "What are the flight characteristics of the Flying V sub-scale model at approach speed and high angles of attack?".

In total, three different wind tunnel campaigns were conducted at the Open Jet Facility of the Delft University of Technology. During the wind tunnel campaigns, experiments were conducted to acquire data through balance measurements and flow visualisation techniques by means of oil, tufts and smoke. The untrimmed maximum lift coefficient was estimated to be 1.09 at 41 degrees angle of attack and positive stability was found up to 20 degrees angle of attack. Flow visualisation results showed that large leading edge vortices acted on the surface of the wing, originating from the root towards the crank of the wing. A leading edge separated vortex spread over the wingtip, which originated at the kink of the leading edge.

Investigations into the trimmed flight of the aircraft concluded that due to trim limitations the centre of gravity is bound between 1.345 and 1.425 meter behind the nose. The centre of gravity has an optimal location at 1.365 meter behind the nose, providing a static margin of about 9%. With the trimmed lift curve and the optimal centre of gravity location, the flight speed of 35 meter per second can be flown at 3.6 degrees angle of attack.

Due to limitation in maximum deflection of the control surfaces, the maximum lift coefficient is estimated at 0.95, at 28.5 degrees angle of attack at a stall speed of 14.8 meter per second. At 20 degrees angle of attack, where the static stability switches from positive to negative, the lift coefficient is estimated at 0.73 at 17.2 meter per second and is defined as the 'safe' stall speed. Taking the FAA and ICAO regulations into account, the approach speed is estimated at 19.2 meter per second, at an angle of attack of 15.9 degrees at a lift coefficient of 0.58.

Acknowledgements

With the completion of my Master of Science (MSc) at the faculty of Aerospace Engineering, my time as a student comes to an end. With lots of pleasure, gratification and positive energy, I look back at an awesome chapter of my life. After more than seven years of gaining knowledge in my passion of aerospace engineering, it is time to find closure to this chapter with the finalisation of my Master's thesis project.

My thanks go to Roelof Vos, who supported and guided me throughout the thesis research project. Furthermore, I would like to thank Akshay Raju Kulkarni, who has always challenged me to critically examine this research from all perspectives and who supported me throughout the project. Malcom Brown, Marco Palermo and Alberto Ruiz Garcia, this project I will always remember as to have been part of the most driven and committed project team at the university, a team that never knew how to give up. Biagio Della Corte and Tomas Sinnige, my thanks for your help and advice during the wind tunnel experiments.

On a personal level, I would like to thank my girlfriend and family, for the many years of unconditional support and love during my studies.

*Rob Alexander Viet
Delft, March 2019*

Contents

List of Figures	ix
List of Tables	xiii
Nomenclature	xvii
1 Introduction	1
1.1 Flying Wings	1
1.2 The Flying V	3
1.2.1 Initial Proposal	3
1.2.2 Previous Work	4
1.3 Problem Statement	4
1.3.1 Angle of Attack and Speed Constraints	5
1.3.2 Centre of Gravity Positioning	5
1.3.3 Control Surface Usage	6
1.4 Research Objective and Questions	7
1.5 Thesis Report Outline	7
2 Model and Experiment	9
2.1 Manufacturing	9
2.1.1 Design	9
2.1.2 Materials	12
2.1.3 Vacuum Assisted Resin Transfer Moulding	12
2.1.4 Assembly	14
2.2 Wind Tunnel Testing	16
2.2.1 Goals of Wind Tunnel Experiment	16
2.2.2 Wind Tunnel Set-Up	16
2.2.3 Flow Measurement Techniques	21
2.2.4 Expected Results	22
3 Verification and Validation	23
3.1 Wind Tunnel Corrections	23
3.1.1 Bias Corrections	23
3.1.2 Open Wind Tunnel Corrections	24
3.2 Verification	28
3.2.1 Tufts and Oil Flow Comparison	28
3.2.2 Reynolds Number Effects	29
3.3 Validation	31
4 Wind Tunnel Results	33
4.1 Balance Results	33
4.1.1 Lift Results	33
4.1.2 Pitching Moment Results	37
4.2 Flow Visualisation Interpretation	44
4.2.1 List of Definitions	44
4.2.2 Oil Flow	45
4.2.2.1 Topology Layouts for Low Angles of Attack (5 - 9 degrees)	46
4.2.2.2 Topology Layouts for Medium Angles of Attack (11 - 17 degrees)	50
4.2.2.3 Topology Layouts for High Angles of Attack (19 - 23 degrees)	54
4.2.2.4 Topology Layouts for Very High Angles of Attack (25 - 50 degrees)	59
4.2.3 Tufts	67
4.2.4 Smoke	72

5 Preliminary Flight Discussion	77
5.1 Stall Behaviour	77
5.2 Trimmed Flight	80
5.3 Approach Implications.	88
6 Conclusions	91
6.1 Recommendations and Future Work	92
Bibliography	93
A Original Oil Flow Visualisation Pictures	97
B Additional Moment Curve Figures	119

List of Figures

1.1	Impression of various flying wings	1
1.2	Impression of the initially proposed Flying V aircraft	3
1.3	Optimised planform of the Flying V	4
2.1	Planform of the scaled half model of the Flying V	10
2.2	Isometric view of the CATIA design	11
2.3	Infusion of the upper wing skin	13
2.4	Spars and ribs fitted in the lower wing skin	14
2.5	Closed wing skin	14
2.6	Cut out of the control surfaces	15
2.7	Control surface with a balsa wood leading edge	15
2.8	Impression of the Open Jet Facility	16
2.9	Set-up for the wind tunnel experiment with the half-model mounted	17
2.10	First campaign support set-up	18
2.11	Second and third campaign support set-up	18
2.12	Lower view of the set-up for the wind tunnel experiment	19
2.13	Upper view of the set-up for the wind tunnel experiment	19
2.14	Schematic isometric view of the set-up used during the wind tunnel experiments	19
2.15	Schematic side view of the set-up used during the wind tunnel experiments	20
2.16	Schematic top view of the set-up used during the wind tunnel experiments	20
2.17	Schematic rear view of the set-up used during the wind tunnel experiments	20
2.18	Measurement techniques of flow visualisation around a test object in a wind tunnel	21
3.1	Impression of the symmetry plane of the tunnel and wing (not to scale)	25
3.2	Comparison of the wings lift curve with and without tufts equipped	29
3.3	Comparison of the wings lift curve with and without visualisation oil applied on the surface	29
3.4	Comparison for different Reynolds numbers on the lift coefficient	30
3.5	Standard deviation for the lift curve	31
4.1	Lift axis system	34
4.2	Lift coefficient comparison for each wind tunnel campaign	34
4.3	Lift slope comparison for each wind tunnel campaign	36
4.4	Pre-determined centre of gravity location	37
4.5	Moment axis system	38
4.6	Moment coefficient comparison for each wind tunnel campaign	39
4.7	Centre of pressure location comparison for each wind tunnel campaign	39
4.8	Comparison of the stability derivative for each wind tunnel campaign	40
4.9	Comparison of the neutral point for each wind tunnel campaign	42
4.10	MAC and neutral point location visualisation	43
4.11	Oil visualisation for 22 degrees angle of attack	45
4.12	Oil visualisation for 5 degrees angle of attack	46
4.13	Illustration of isobars and streamlines of a backward-swept wing	47
4.14	Oil visualisation for 7 degrees angle of attack	48
4.15	Oil visualisation for 9 degrees angle of attack	49
4.16	Oil visualisation for 11 degrees angle of attack	50
4.17	Oil visualisation for 13 degrees angle of attack	51
4.18	Oil visualisation for 15 degrees angle of attack	52
4.19	Oil visualisation for 17 degrees angle of attack	53
4.20	Oil visualisation for 19 degrees angle of attack	54

4.21 Oil visualisation for 20 degrees angle of attack	55
4.22 Oil visualisation for 21 degrees angle of attack	56
4.23 Oil visualisation for 22 degrees angle of attack	57
4.24 Oil visualisation for 23 degrees angle of attack	58
4.25 Oil visualisation for 25 degrees angle of attack	59
4.26 Oil visualisation for 27 degrees angle of attack	60
4.27 Oil visualisation for 29 degrees angle of attack	61
4.28 Oil visualisation for 31 degrees angle of attack	62
4.29 Oil visualisation for 33 degrees angle of attack	63
4.30 Oil visualisation for 35 degrees angle of attack	64
4.31 Oil visualisation for 41 degrees angle of attack	65
4.32 Oil visualisation for 50 degrees angle of attack	66
4.33 Impression of the tuft configuration at 11 degrees angle of attack	67
4.34 Topology layout of the tuft configuration at 15 degrees angle of attack	68
4.35 Comparison of the tuft configuration and oil visualisation at 15 degrees angle of attack	69
4.36 Topology layout of the tuft configuration at 29 degrees angle of attack	70
4.37 Comparison of the tuft configuration and oil visualisation at 29 degrees angle of attack	71
4.38 Impression of rotating boundary layer	72
4.39 Primary vortex visualisation by means of smoke	73
4.40 Vortex at the suction side of the wing visualised by means of smoke	73
4.41 Vortex at the pressure side of the wing visualised by means of smoke	74
4.42 Counter-rotating vortices at both sides of the wing visualised by means of smoke	74
4.43 Leading edge vortex visualised by means of smoke	75
4.44 Wingtip vortex visualised by means of smoke	75
5.1 Lift and moment curve combined with the streamlines from the oil flow visualisation	79
5.2 Centre of pressure compared to the centre of gravity locations for no control surface deflections	81
5.3 Centre of pressure compared to the centre of gravity locations for multiple control surface deflections	82
5.4 Neutral point compared to the centre of gravity locations	84
5.5 Moment coefficient comparison for the control surface deflections with the CG at 1.345 meters behind the nose	85
5.6 Moment coefficient comparison for the control surface deflections with the CG at 1.425 meters behind the nose	86
5.7 Moment coefficient comparison for the control surface deflections with the CG at 1.365 meters behind the nose	87
5.8 Trimmed lift curve	88
5.9 Overview of the investigated CG locations	90
A.1 Oil flow visualisation at 5 degrees angle of attack	98
A.2 Oil flow visualisation at 7 degrees angle of attack	99
A.3 Oil flow visualisation at 9 degrees angle of attack	100
A.4 Oil flow visualisation at 11 degrees angle of attack	101
A.5 Oil flow visualisation at 13 degrees angle of attack	102
A.6 Oil flow visualisation at 15 degrees angle of attack	103
A.7 Oil flow visualisation at 17 degrees angle of attack	104
A.8 Oil flow visualisation at 19 degrees angle of attack	105
A.9 Oil flow visualisation at 20 degrees angle of attack	106
A.10 Oil flow visualisation at 21 degrees angle of attack	107
A.11 Oil flow visualisation at 22 degrees angle of attack	108
A.12 Oil flow visualisation at 23 degrees angle of attack	109
A.13 Oil flow visualisation at 25 degrees angle of attack	110
A.14 Oil flow visualisation at 27 degrees angle of attack	111
A.15 Oil flow visualisation at 29 degrees angle of attack	112
A.16 Oil flow visualisation at 31 degrees angle of attack	113

A.17 Oil flow visualisation at 33 degrees angle of attack	114
A.18 Oil flow visualisation at 35 degrees angle of attack	115
A.19 Oil flow visualisation at 41 degrees angle of attack	116
A.20 Oil flow visualisation at 50 degrees angle of attack	117
B.1 Moment coefficient comparison for the control surface deflections with the CG at 1.330 meters behind the nose	120
B.2 Moment coefficient comparison for the control surface deflections with the CG at 1.275 meters behind the nose	121
B.3 Moment coefficient comparison for the control surface deflections with the CG at 1.220 meters behind the nose	122

List of Tables

3.1	Summary of dimensions used for boundary correction factor estimation	26
3.2	Summary of boundary correction factors	26
3.3	Summary of open wind tunnel corrections	27
3.4	Standard and maximum deviation of the balance	28
3.5	Reynolds numbers at the MAC of 0.820 meter	30
4.1	Maximum lift coefficient	35
4.2	Lift slope coefficients	36
4.3	Neutral point and static margin overview	42
5.1	Deflection angles for the inputs of the control surfaces	80
5.2	Centre of gravity location investigation	83
5.3	Static margin investigation	84
5.4	Angles of attack during trimmed flight	89
5.5	Flight speed and angle of attack for trimmed approach	90

Nomenclature

List of Abbreviations

AoA	Angle of Attack
BWB	Blended-Wing-Body
CFD	Computational Fluid Dynamics
CG	Centre of Gravity
CoM	Centre of Measurement
CP	Centre of Pressure
MAC	Mean Aerodynamic Chord
OJF	Open Jet Facility
SM	Static Margin
VARTM	Vacuum Assisted Resin Transfer Moulding

List of Greek Symbols

α	Angle of attack of the wing	deg
α_{trim}	Angle of attack at which the aircraft can be trimmed	deg
α_u	Uncorrected angle of attack	deg
$\Delta\alpha_w$	Angle of attack correction for the wing	deg
δ	Boundary correction factor	-
ϵ_{sb}	Solid blockage factor	-
ϵ_t	Total solid blockage factor	-
ϵ_{wb}	Wake blockage factor	-
ρ	Air density	kg/m ³
τ_1	Model test-section to model span-to-tunnel-width ratio factor	-
θ	Angle of the balance and turntable	deg
φ	Angle of the resultant force to the y-axis	deg

List of Roman Symbols

\bar{c}	Mean aerodynamic chord	m
$\Delta C_{L_{vortex}}$	Added lift coefficient due to vortices	-
ΔP	Delta pressure	N/m ²

Re	Reynolds number	-
b	Geometric wingspan	m
b_a	Jet width	m
b_v	Effective vortex span	m
C	Jet test-sectional area	m ²
C_L	Lift coefficient	-
C_{D_0}	Zero lift drag coefficient	-
C_{D_i}	Induced drag coefficient	-
C_D	Drag coefficient	-
C_{L_α}	Lift slope	1/rad
C_{L_w}	Lift coefficient of the wing	-
$C_{L_{trim}}$	Trimmed lift coefficient	-
$C_{M_{\alpha_{c/4}}}$	Stability derivative around the quarter MAC location	1/rad
C_{M_α}	Stability derivative	1/rad
$C_{M_{\bar{c}/4}}$	Moment coefficient around the quarter MAC location	-
$C_{M_{cg}}$	Moment coefficient around the centre of gravity	-
C_M	Moment coefficient	-
F_x	Force in x-direction of the balance	N
F_y	Force in y-direction of the balance	N
F_z	Force in z-direction of the balance	N
F_R	Resultant force of the lift and drag forces	N
h_a	Jet height	m
K_1	Body shape factor	-
L	Lift force	N
M_x	Moment around x-direction of the balance	N · m
M_y	Moment around y-direction of the balance	N · m
M_z	Moment around z-direction of the balance	N · m
M_{cg}	Moment around the centre of gravity	N · m
n	Fan rotational speed	rpm
P	Static pressure	N/m ²
P_0	Total pressure	N/m ²
q	Dynamic pressure	N/m ²
q_a	Dynamic pressure at the nozzle	N/m ²
q_c	Corrected dynamic pressure	N/m ²

S	Wing surface area	m^2
SM	Static Margin	%
t	Time	s
T_0	Total temperature	$^{\circ}\text{C}$
V	Undisturbed air velocity	m/s
$V_{w,s}$	Volume of the wing or shield	m^3
W	Weight of the aircraft	N
$x_{\bar{c}/4}$	Quarter mean aerodynamic chord	m
x_{cg}	Centre of gravity location measured from the nose	m
x_{COM}	Centre of measurement location measured from the nose	m
x_{cp}	Centre of pressure location measured from the nose	m
x_{np}	Neutral point location measured from the nose	m

1

Introduction

During the last five decades, commercial aviation has been based on a “conventional layout”. This layout is based on a tube fuselage with a high aspect ratio wing including podded engines under the wing and aft-tail planes [1]. Due to the fact that its productivity and performance characteristics are reaching an asymptotic limit, the focus has been to design new unconventional configurations for the future. One of the most promising configurations is the flying wing, a configuration which is characterised by a merged fuselage and wing. Examples of these flying wings are concepts like the blended-wing-body, the C-wing, etc [2]. In figure 1.1, impressions of flying wings can be found.



Figure 1.1: Impression of various flying wings

As shown in figure 1.1, flying wings feature a different configuration compared to the conventional tube fuselage aircrafts. The explanation for this unconventional design is found in the planform. The planform allows for that design changes with respect to conventional aircraft can be made, in order to optimise efficiency and reduce the fuel consumption. The impact of the planform on the design is explained in section 1.1. In section 1.2, the Flying V aircraft is discussed, followed by the introduction to the research by the problem statement in section 1.3. Section 1.4 presents the research objective and questions, followed by the thesis report outline in section 1.5.

1.1. Flying Wings

A flying wing is an aircraft where the design configuration merges the main fuselage into the wing. As a result, the fuselage section is increased, reducing the ratio of wetted area towards the wingspan and thus reducing the skin friction drag. Besides the wings, the main body is shaped as an airfoil as well, so compared to conventional aircraft having a tubular fuselage, the flying wing will generate additional

¹The HUULC, Hydrogen-powered Unmanned Ultra Large Cargo aircraft - Platform Unmanned Cargo Aircraft, URL: <https://www.platformuca.org/uav/the-huulc-hydrogen-unmanned-ultralarge-unmanned-aircraft-video/>, visited on: January 24th, 2019

²New Ideas Sharpen Focus for Greener Aircraft - NASA, URL: https://www.nasa.gov/topics/aeronautics/features/greener_aircraft.html, visited on: January 24th, 2019

³B-2 Spirit - U.S. Air Force, URL: <https://www.af.mil/About-Us/Fact-Sheets/Display/Article/104482/b-2-spirit/>, visited on: January 24th, 2019

lift on this section. Due to the increased area on top of the main body, engines can be mounted over the wing and noise levels might be reduced [3].

It was assumed that a flying wing provides a 20-25% advantage in lift over drag, a reduction in direct operational cost by 7-8% and a 30% fuel consumption reduction compared to conventional aircrafts. The explanation was found due to higher Reynolds numbers on wing chords, which were twice as large as those of conventional aircrafts. Besides this, flying wings have an absence of a horizontal tail, which reduced the friction and induced drag, and a reduced static margin in the longitudinal direction [4–6].

Furthermore, the wide airfoil-liked body is intended to obtain an effective spanwise lift distribution. The aerodynamic load on the outboard wings is decreased because of a big central chord bearing the main part of the span loading, which is located in the central body of the aircraft. Because of this configuration, the central body needs a low lift coefficient to induce an elliptical spanwise load distribution. As a result, the central spanwise location can be thickened to achieve the required space for passengers and cargo spacing, without imposing a huge compressibility drag penalty. Furthermore, high lift devices are not necessary because of the low and effective load. At high subsonic speeds, the geometric shape of the planform relatively weakens shock waves over the wings and body. The area behind these shock waves impose the ideal location for the placement of engine installation [7].

However, while the flying wing imposes a higher aerodynamic efficiency, it also has its throwbacks. Due to an absence of a horizontal tail and a relative high pitching moment from its large lifting body, flying wings might have problems with the longitudinal static stability [6]. Furthermore, the rudders and elevators of flying wings might not have the same level of command as they have on conventional aircraft. To overcome this issue, the dimensions of the control surfaces can be increased to give larger moments, but as a result, the hinge moment will increase with the cube of the scale [3].

At the nominal cruise condition, the trim of a flying wing aircraft is considered as trimmed when the aerodynamic centre of pressure is coinciding with the centre of gravity [8]. The nose-up and nose-down pitching moment is required to be minimised by the fact that the aircraft needs to have positive static stability. This limits the use of positive aft camber and conflicts with the cabin deck angle requirement.

Because of the fact that a flying wing has no empennage to trim resulting pitching moments, the aircraft can not use high lift devices such as flaps. As a result, trailing edge control surface deflections are set by trim requirements, rather than maximum lift. Therefore, a flying wing will have both a lower maximum lift coefficient and a lower wing loading compared to conventional aircraft. Examples of the trim on the lift behaviour can be found in AGARD [9]. This implies that the maximum lift coefficient of a flying wing will occur at relatively high angles of attack.

In case of a flying wing with high sweep angle, research performed by Luckring [10] showed that in combination with a blunt leading edge, the range for angles of attack increases due to leading edge vortices rolling over the suction side of the surface. Three examples of blunt leading edge flying wings are given in figure 1.1. Luckring [10] showed that a 50 degrees constant swept chord wing with a blunt ONERA D airfoil had its maximum lift attained at an angle of attack of about 30 degrees. The setup used showed that at a Reynolds number of $2.3 \cdot 10^6$ the maximum lift angle already shifted by more than 10 degrees compared to the study performed on the Boeing 777-200. The influence of the sweep angle changed the relative airfoil shape that the air flow faced, which was different compared to a non-swept wing. In other words, the sweep of the wing made the relative chord length longer and therefore less blunt. As was researched by Luckring [10], the larger the sweep angle of the blunt airfoil wing, the larger the angle of attack of the maximum lift was.

The same pattern occurs to delta wings, where large leading edge vortices are rolling over the wing [11, 12]. Delta wings are aircraft which feature a triangular planform. Examples of such aircraft are the Concorde, the Avro Vulcan and the Eurofighter Typhoon. The leading edge vortices on delta wings characterise the aircrafts flight performance in such a way that the maximum lift coefficient may be around 40 degrees angle of attack [13]. Therefore, close correlation might be found between highly swept flying wings with blunt leading edges and delta wings.

1.2. The Flying V

This section elaborates on the work of the initial proposal of the Flying V aircraft and the research progress made by the Delft University of Technology. The initial proposal can be found in subsection 1.2.1. The research progress made by the Delft University of Technology can be found in subsection 1.2.2. This progress will be, together with the initial proposal, used to identify the problem and give answer to the research questions.

1.2.1. Initial Proposal

Research on flying wings has led to advantages, disadvantages and constraints compared to conventional aircraft. One of the ideas Benad came up with, was an aircraft called the Flying V [14]. In this work, a study was performed to see how the volume inside a pure flying wing for commercial passenger transport was derived. An impression of the Flying V can be found in figure 1.2.

A configuration proposal of two cylindrical pressurised sections for the payload swept-back in the shape of the letter V was made and compared to the reference aircraft, the Airbus A350-900⁴. The two cylindrical pressurised sections were initially designed to hold up to 315 passengers in a two class seat layout throughout the whole cabin. Because the cylinders are put in a swept-back position at the leading-edge, a cut-out in the stream-wise direction results in a flat and elliptical shape, compared to a circular shape if the cut is being made orthogonal to the leading edge. The way of putting the pressurised cylinders in a swept-back position is beneficial to the structural solution of the aircraft itself, as the pressurised cylinders can maintain their original cylindrical shape and no further strengthening is required.

Compared to the Airbus A350-900, the Flying V has the same number of passenger and a cruise speed of $M = 0.85$ which, due to the advantages of the blended-wing-body shape, leads to a 10% higher lift over drag ratio and a 2% lower empty weight of the aircraft. More advantages of the Flying V is that the aircraft is smaller and more compact compared to the Airbus A350-900 and that it has a simpler configuration. This simpler configuration means that the Flying V does not have any high-lift device and fairings equipped.

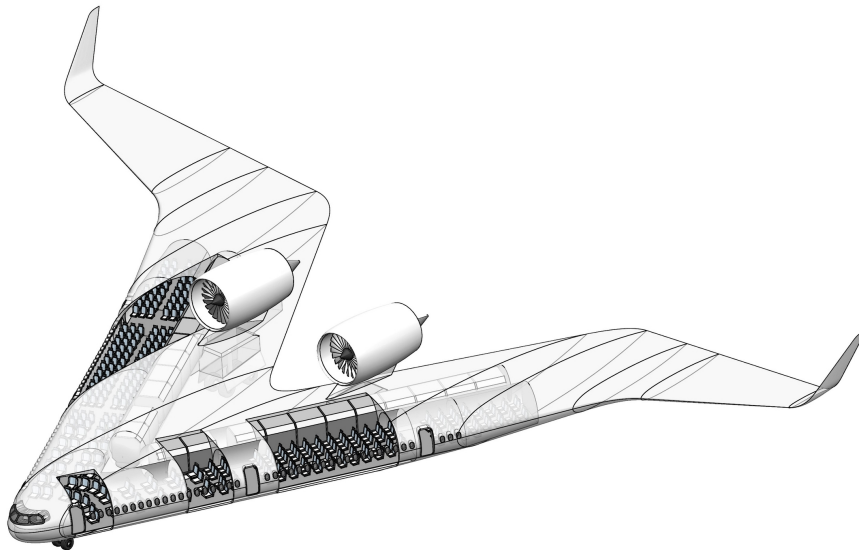


Figure 1.2: Impression of the initially proposed Flying V aircraft⁵

⁴Airbus A350-900, URL: <https://www.airbus.com/aircraft/passenger-aircraft/a350xwb-family/a350-900.html>, visited on: January 28th, 2019

⁵The Flying V, URL: <http://www.jbenad.com/flyingv/>, visited on: January 28th, 2019

As the engines are put over the wing, instead of under the wing, the noise is shielded from the ground and results in less noise [15, 16] compared to the Airbus A350-900. Since the design of the aircraft only uses a moderate wing twist and no reflexed camber lines, the lift distribution of the Flying V is elliptical [17], even though it has an irregular shape. Based on this, along with the aerodynamic and structural advantages, the design of the Flying V is worth-while to continue the investigation. Research done at the Delft University of Technology will be discussed in the next subsection.

1.2.2. Previous Work

A summary of the work done by the researches at the Delft University of Technology is as follows. Faggiano *et al.* [18] performed a research on the aerodynamic design of the Flying V and how the aerodynamic performances during the cruise phase compared to the NASA CRM. Answers were found in how the three-dimensional geometry of the aircraft could be parametrized and what the maximum lift over drag ratio of the aircraft during cruise was. With a lift coefficient of 0.26 during cruise, the multi-fidelity calculations led to a lift over drag ratio of 23.7, which is about 25% higher compared to similar conventional aircraft with the same mission profile. Besides the calculations performed for the lift and drag ratio, the multi-fidelity calculations optimised the design for the Flying V as well. The results of the new planform solution can be found in figure 1.3.

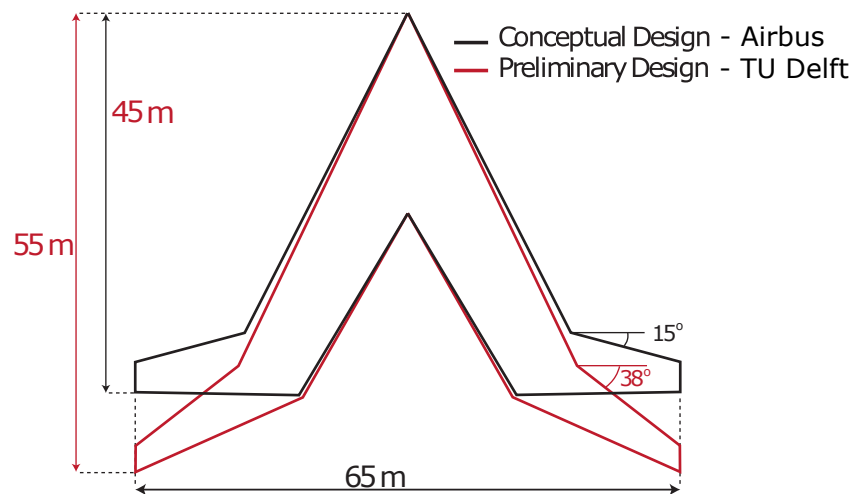


Figure 1.3: Optimised planform of the Flying V

The planform of the Flying V, which can be seen in figure 1.3, was optimised in such a way to lower the super-velocities, local lift coefficient and thus the Mach numbers. The main sweep angle was slightly increased and the sweep angle from the kink till the tip was increased from 15 degrees to 38 degrees. As a result, the Mach numbers over the wing were considerably lower compared to the original design by Benad and Airbus Operations GmbH [14].

1.3. Problem Statement

Based on the advantages, disadvantages, constraints and characteristics of flying wings, Benad and Airbus Operations GmbH [14] came up with a preliminary study which resulted in a concept aircraft called the Flying V. Based on the results of this study, a patent was issued which led to the interest of the Delft University of Technology. Research performed at the Delft University of Technology led to an optimised design from the conceptual design proposed by Benad and Airbus Operations GmbH [14]. Results showed improvements for the structural weight and aerodynamic efficiency of the aircraft, which means that the optimised preliminary aircraft has potential for further research.

The next step in the research performed by the Delft University of Technology is to demonstrate the flight capabilities and airworthiness of the Flying V. This will be done by performing a sub-scale flight test with the optimised preliminary model. Sub-scale flight testing is used to evaluate and demonstrate free flight characteristics of an aircraft [19]. Compared to a full-scale flight test, a sub-scale flight test is

a convenient way to investigate extreme and high risk portions of the flight envelope without exposing a pilot to risk. By using sub-scale flight testing, the risks and costs of a manned full-scaled flight are reduced and it therefore offers an ideal opportunity to demonstrate the feasibility of unconventional and innovative designs such as the Flying V. Examples of sub-scale flight tests performed are for example the PTERA⁶ and MicroCub⁷ from NASA, and the X-48 Blended Wing Body⁸ from NASA and Boeing.

Before the sub-scale flight test can be performed, the entire set of flight characteristics has to be known. Since in the previous work performed at the Delft University of Technology the optimised preliminary aircraft was investigated for cruise only, no research has been performed regarding the flight characteristics during approach speed and high angles of attack. Therefore, research has to be performed into the behaviour of the aircraft and the flow during approach speed and at high angles of attack. Three different scenarios that may cause the sub-scale flight to fail during the test are identified and discussed below in sections 1.3.1, 1.3.2 and 1.3.3.

1.3.1. Angle of Attack and Speed Constraints

During the sub-scale flight test, it is important to know the approach and stall speed of the aircraft. By not knowing these speeds, it may occur that during approach the flight speed of the aircraft drops below the stall speed and the aircraft falls out of the sky. The explanation for this event can be found in equation 1.1 and 1.2.

$$L = W \quad (1.1)$$

$$L = C_L \frac{1}{2} \rho V^2 S \quad (1.2)$$

The relation between these equations is that the weight of the aircraft must be same as the lift produced by the flow over the wings, in order to maintain height during flight. The lift of the aircraft can be changed if required. If it is required for the aircraft to lower its altitude, the lift of the aircraft must be reduced. This can be done by reducing either the angle of attack of the aircraft, which lowers the lift coefficient, or the flight speed. Both the lift coefficient and the flow speed are related to the flow behaviour over the wing.

The flow behaviour over the wing for the approach and stall speed is unknown, as well as for the variation in angle of attack. By not knowing the flow behaviour, it is not possible to set constraints on both the minimal flight speed and the maximum angle of attack. By increasing the angle of attack too much, the flow over the aircraft might separate and loss of lift occurs. By flying below the stall speed, not enough suction force will be produced to generate lift and the aircraft will fall out of the sky. Both of these two scenarios will lead to a loss of the aircraft. Therefore, the pilot has to know these values before the sub-scale flight test can be performed.

1.3.2. Centre of Gravity Positioning

The positioning of the centre of gravity for aircrafts is important for the stability and trim. A statically stable aircraft is able to naturally dampen out any destabilising inputs. An example of the importance of a statically stable aircraft is elaborated in an example below.

“As the pilot of the sub-scale model is performing the flight test, a sudden gust strikes the aircraft. The sudden gust influences the flow behaviour over the wing and increases the suction forces over the wing. As a result, the angle of attack is increased. The angle of attack rises quickly and the pilot loses control over the aircraft, resulting in a loss of the aircraft.”

⁶NASA Armstrong Fact Sheet: Prototype-Technology Evaluation and Research Aircraft (PTERA), URL: <https://www.nasa.gov/centers/armstrong/news/FactSheets/FS-108-AFRC.html>, visited on: February 12th, 2019

⁷NASA Armstrong Successfully Flies a New Subscale Aircraft, URL: https://www.nasa.gov/centers/armstrong/features/microcub_first_flight.html, visited on: February 12th, 2019

⁸X-48 Blended Wing Body Research Aircraft Makes 100th Test Flight, URL: https://www.nasa.gov/centers/dryden/Features/x-48_100th_testFlight.html, visited on: February 12th, 2019

In the example above, the aircraft was statically unstable. This means that the angle of attack exponentially increased and is hard or even impossible to counteract for by the pilot. For a statically stable aircraft, the positive change in angle of attack will naturally be counteracted by the aircraft itself in a damped motion. The aircraft will return to its original angle of attack. For statically neutral aircraft, the positive change in angle of attack leads to significant difference after the gust, meaning the gust changes the attitude of the aircraft into another statically neutral state.

Based on the example given above, it is important for the aircraft to be statically stable. This can be achieved by positioning the centre of gravity in a precise location. The location of the centre of gravity depends on the location of the resultant force. The resultant force is the summed force of the main body lifting forces and the control surfaces lifting forces. The location of the centre of gravity must lie ahead of the resultant force, in order for the aircraft to be statically stable. If the location of the centre of gravity lies on top of the resultant force, the aircraft is statically neutral. For the scenario discussed in the example above, the location of the centre of gravity was aft of the resultant force and the aircraft was statically unstable.

Therefore, the location of the resultant force has to be known in order to position the centre of gravity carefully. By placing the centre gravity carefully ahead of the resultant force, the pilot will be able to fly a statically stable aircraft, with a decreased risk of losing the aircraft due to static instability.

1.3.3. Control Surface Usage

The control surfaces are the most important measure for the attitude change and trim of the aircraft. A positive deflection of the control surfaces (pointing down) results in an increased suction force and therefore an increase in lift force. The other way around, a negative deflection of the control surfaces (pointing up) results in a decrease in suction force and a decrease in lift. By moving the control surfaces up and down, both the strength and the position of the resultant force will change. As a result, the aircraft will pitch up (nose up), or pitch down (nose down).

By a pitch up of the aircraft, the aircraft will increase its angle of attack and therefore increase the generated lift. The other way around, a pitch down motion decreases the angle of attack and the lift coefficient and makes the aircraft decrease its altitude. This way by making use of the control surfaces, the aircrafts attitude and altitude can be controlled by the pilot.

For the pilot it is important that the control surfaces allow for both trim and pitch control at all angles of attack of the flight envelope. Therefore, it is important to know the effectiveness of the control surfaces. For the pilot being able to control the aircraft, it is required to find out what the relation is between the pitching moment and the centre of gravity location. Since the control surfaces were sized and fixed in the design, the amount of control effectiveness can be changed by putting the centre of gravity at a certain percentage ahead of the resultant force. This is defined by the static margin.

It is generally used that the centre of gravity lies between a static margin of 5-15% of the mean aerodynamic chord length ahead of the resultant force location. If the centre of gravity lies close to the resultant force, the control surfaces provide very rapid pitch changes against a low static stability. The other way around, if the centre of gravity lies far ahead of the resultant force, the aircraft shows a high static stability with low control surface effectiveness. By keeping the static margin within the 5-15%, the aircraft will show the best combination between static stability and control effectiveness. This way, the pilot is able to move the control surfaces such that the aircraft is trimmed and can be controlled for pitch.

Not only is it for the pilot important to know how the pitch of the aircraft is handled by the control surface, the pilot also needs to know how what to expect from the control surfaces regarding the lift. As mentioned earlier in this subsection, if the control surfaces are positive deflected, the overall lift of the aircraft is increased and the opposite occurs as the control surfaces are negatively deflected. A certain state of trimmed flight might therefore be different if the centre of gravity was positioned at a different location. Incorrect positioning of the centre of gravity and not knowing the effectiveness of the control surfaces and its impact on the lift, pitch and stability of the aircraft may result in a loss of the aircraft.

1.4. Research Objective and Questions

The objective of the thesis research holds the assessment of the flight characteristics of the Flying V sub-scale model at approach speed and high angles of attack, by performing a wind tunnel test using a self built scale model. As discussed in the problem statement in section 1.3, the flight characteristics during approach speed and high angles of attack are unknown. This is however essential for the pilot to fly a statically stable aircraft and to have constraints on the angle of attack and minimum flight speed to avoid losing the aircraft. The assessment was performed using a scale model of the Flying V, which was built by hand. The research is based on the results of a wind tunnel experiment performed at the Open Jet Facility at the Delft University of Technology.

Based on the initial proposal, the previous work and the problem statement, the main research question of the thesis is defined as:

“What are the flight characteristics of the Flying V sub-scale model at approach speed and high angles of attack?”

To provide information to solve the main research question, sub questions are defined. The sub questions are defined as:

1. What is the lift generation mechanism for the approach speed of the Flying V sub-scale model at varying angles of attack and what is the effect on the lift and pitching moment?
2. What is the optimal centre of gravity location of the Flying V sub-scale model that ensures trimmed flight and a statically stable aircraft?
3. For a given set of the control surface design, what is the estimation for the approach and stall speed for the Flying V sub-scale model?

1.5. Thesis Report Outline

The thesis research report is divided into several chapters. In chapter 1, the introduction of the thesis research is given. In this chapter, a literature review for the initial proposal and the previous work of the Flying V is given. Based on this, the research problem is defined, followed by the research objectives and questions. Chapter 2 elaborates on the model and experiments performed. First, the design, manufacturing and assembly of the sub-scale model is discussed, followed by the goals, experimental set-up and expected results of the wind tunnel experiments. Before the results from the experimental tests are presented and discussed, a discussion towards the wind tunnel corrections, verification and validation of the results is made in chapter 3. In chapter 4, the results of the wind tunnel experiments are presented. This chapter is divided into two sections, the first section presenting and discussing the results of the balance measurements and the second section presenting and discussing the results of the flow visualisations. The interpretation of the wind tunnel experiments towards the sub-scale flight test is discussed in chapter 5. In this chapter, the stall behaviour, trimmed flight and approach implications are discussed. The thesis research report is concluded in chapter 6, in which recommendations and a discussion towards future work is given as well.

2

Model and Experiment

In this chapter the model and the experiment will be discussed. The chapter is started with the manufacturing of the aircraft in section 2.1, where the design, materials, infusions and assembly is discussed. Section 2.2 is about the wind tunnel setup, what to expect during the wind tunnel test and which results are expected from the wind tunnel test.

2.1. Manufacturing

In this section the manufacturing of the Flying V is described. This is done by the design of the Flying V, as presented in subsection 2.1.1. In subsection 2.1.2, the materials for the half model are discussed, followed by the part manufacturing using vacuum assisted resin transfer moulding in subsection 2.1.3. In the last subsection 2.1.4, the assembly of the half model is described.

2.1.1. Design

Using the geometry and aerodynamically optimised design from the research performed by Faggiano [20], the outer dimensions of the full-scale Flying V were known. For the wind tunnel experiment, a scaled version of the Flying V was build. To build this model, a design was made using CATIA V5¹. The scaled version of the aircraft had a 3 meter wingspan and a surface area of 1.86 square meter. The reason for this down-scaling of the full-scale model were limitations of the wind tunnel dimensions and collaboration with research studies into scaling laws. The parameters of the planform of the wing can be found in figure 2.1.

As can be seen from this figure, the half model has a root length of around 1.1 meter, a wingspan of about 1.5 meter, four different airfoil locations (at the root, trailing edge kink, leading edge kink and the tip) and two different sweep angles. The sweep angle of the leading edge between the root and the leading edge kink is about 64.5 degrees, while the sweep angle of the leading edge between the leading edge kink and the wing tip is about 37.9 degrees. The maximum thickness over chord ratio at the root is equal to about 0.16, while at the tip this is equal to 0.10.

From the previous researches, only the outer skin geometry could be used for the scaled version of the Flying V. This led to a complete structural and systems design that was performed to make a complete model. During the design process it was chosen to make the aircraft as stiff as possible. After load and stress tests with different materials were performed, it was chosen to manufacture sandwich parts from fibreglass with a foam core for the ribs, spars and skin. The reason for the sandwich parts was in order to withstand the large amount of stresses and shear forces that led to bending and torsion during the wind tunnel test. The selection of the materials is discussed in section 2.1.2.

During the design process, close relation with respect to the wind tunnel model and the flight model had been made. As the wind tunnel model is a half-model and the flight model is a full wingspan model,

¹CATIA - Dassault Systèmes 3D Software, URL: <https://www.3ds.com/products-services/catia/>, visited on: January 17th, 2019

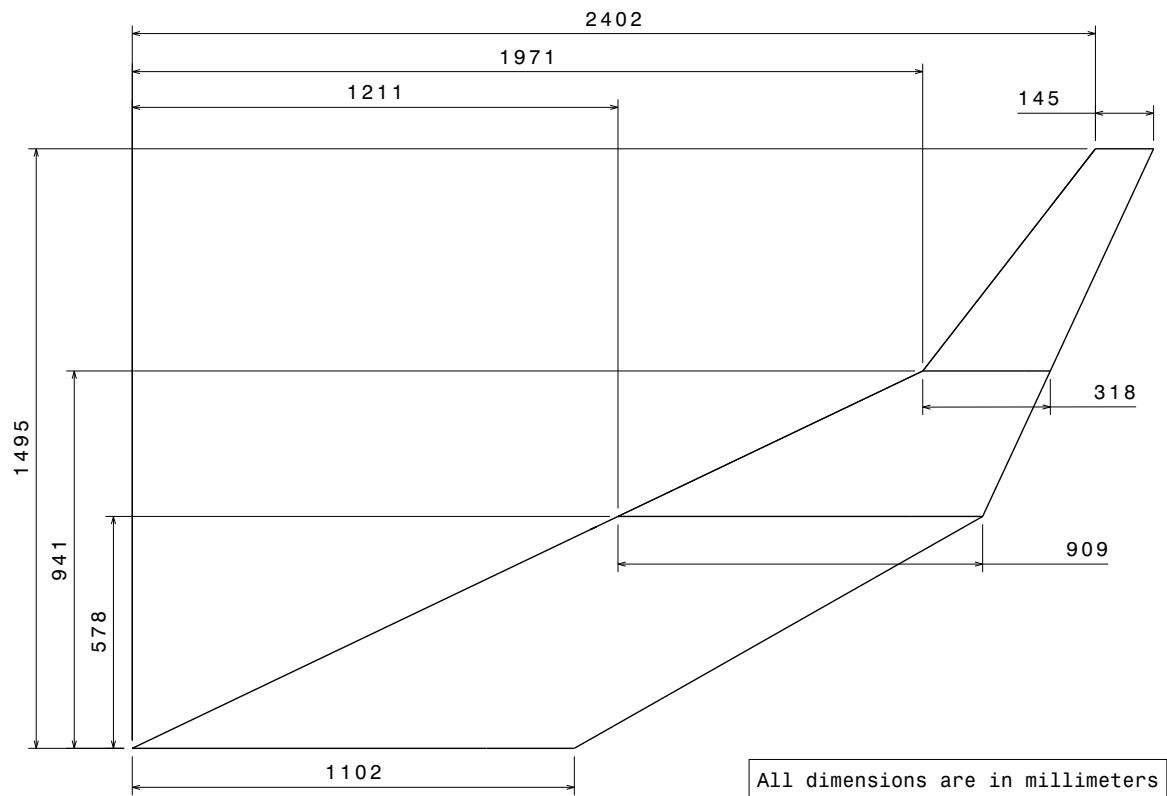


Figure 2.1: Planform of the scaled half model of the Flying V

the wind tunnel model had to consist out of all the equipment that the flight model features as well. Therefore, in the design of the scale model, the flight model was always the standard model to ensure analogy between the wind tunnel and flight test results. In the design, the systems were integrated in the model as well. This included the engines and the design of its support, the winglet and the design of its support, the landing gear integration, the control surfaces, the wiring, the systems integration (e.g. batteries, servos, pitot tube, etc.) and the design of the ribs and spars.

The structural design was performed in the way that the bending and torsion was minimised during the wind tunnel and flight test. A stiff model leads to less aeroelasticity effects for the data obtained from the test. From an experimental test where the buckling load was tested for a panel section, it turned out that a sandwich of three layers of fibreglass, a foam core and another three layers of fibreglass led to the best stiffness versus weight. For the skin it was decided to go for three layers of fibreglass, a foam core in-between the location of the ribs and spars and another three layers of fibreglass.

For the structure of the model, it was chosen to design a wingbox framework inside the skin. This consisted out of a front spar near the leading edge, an aft spar at the trailing edge, twelve ribs in each half wing and three ribs with two spars in the winglet. In the root section of the aircraft, it was chosen to place two ribs perpendicular to the flight direction. This in order to withstand the high stresses and forces in the root of the aircraft. The remaining ribs were placed perpendicular to the front spar for torsional stiffness of the wingbox.

The engines selected for the Flying V are the DS-86-AXI HDS from Schübeler Jets². The engines have a 120 millimetre diameter fan, producing 101 Newton of thrust with an exhaust speed of 99

²Schübeler Jets - HDS Fans, URL: <https://www.schuebeler-jets.de/en/products/hds-en>, visited on: January 18th, 2019

meter per second. One engine would be equipped at either side of the wing, at around 240 millimetres measured in spanwise direction from the root. The support of the engine consisted out of three lightweight aluminium parts. The support for the engines featured an attachment point for the main landing gear as well. This way, the support was optimised to be multi-functional and lightweight for the integration of both the engine and the landing gear. The parts of the support were connected to the aft spar and were both glued and bolted to ensure the connection holds during all flight conditions.

At the wingtip, a support was designed which was able connect the winglet with the wingtip and to carry the loads from the winglet to the wingtip. A curved aluminium piece was designed in order for the winglet to get the correct spacing from the wingtip and for the winglet to have the correct sweep angle. Inside the winglet, a control surface was designed to control the slip angle of the aircraft.

At the trailing edge of the wing between the trailing edge kink and the wingtip, three independently controlled control surfaces were designed to control the pitch and roll of the aircraft. Three independent servos drive the angle of attack for each of the control surfaces. The control surfaces were sized in a research performed by CFD, which determined the required sizes and expected responses from the elevators and ailerons.

An isometric view of the design made in CATIA can be found in figure 2.2. In here, the skin was made transparent to show the inner structure of the aircraft. Next to this, the landing gear, the engines and the support are visualised in the figure as well. The winglet is mounted on the aircraft as well and a cover for the transition between wingtip and winglet had been made. The battery placement is also visualised in the model, but this is only a visualisation, as for the flying model the location will be determined based on the centre of gravity estimate performed in section 5.2.

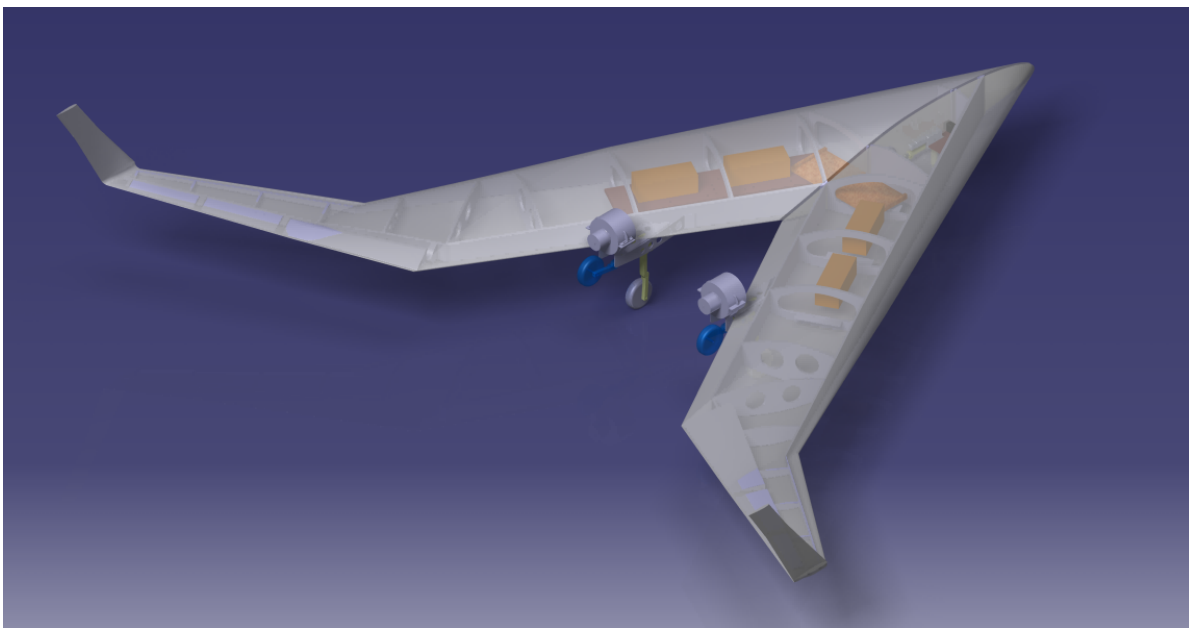


Figure 2.2: Isometric view of the CATIA design

Due to timing towards the wind tunnel experiment, it was chosen to manufacture a simplified model of the full designed aircraft for the half-model of the Flying V. The half-model of the Flying V did not feature the landing gear, the engine and the winglet. Making this decision had multiple implications with respect to the results. The result of the wind tunnel model were based on a half-wing without any off-surface influences, like the engine and landing gear. Therefore, the lift, drag and moment results would be different compared to the full functional flight model. On the other hand, the simplification of the half-model made it easier to understand the flow behaviour over the wing and it made it easier to interpret the result as well.

2.1.2. Materials

For the materials chosen for the manufacturing of the Flying V, testing of sample panels led to the decision for specific materials. An experiment performed for the shear forces of a square sandwich panel showed that the panels could handle over one thousand Newton. These shear forces resulted in shear stresses and strains, which led to the panel to buckle and fail. Besides the buckling of the panel, more tests have been performed based on part bonding, panel manufacturing and bending.

Based on these results, for the skin of the wing a combination of fibreglass with AIREX C70.75 foam panels³ had been chosen. The combination of both the materials led to the possibility of creating a sandwich panel to prevent buckling during the wind tunnel tests. At the location where ribs and spars are positioned, no foam was located to increase the bonding possibilities of the parts. At the leading and trailing edges, no foam panels had been used as well, as no buckling was expected here. AIREX foam had been chosen, because this foam offers closed cells that do not collapse under vacuum during the resin infusion. For the skin, the layup is divided into three layers of fibreglass, followed by the 2 millimetres AIREX panel plates and another three layers of fibreglass.

For the spars and ribs, it was decided to manufacture one large and one small sandwich panel. These sandwich panels were waterjet cutted to get the correct dimensions for the spars and ribs during the assembly. To make all the ribs and spars, the panels were sized in such a way that all parts fitted within the two panels. The core of the sandwich panels did not have the AIREX foam panels, but rather the Depron foam panels. The thickness of the foam was 6 millimetres, this in order to increase the bonding surface of the spars and ribs to the skin of the aircraft. The panels consisted out of three layers of fibreglass, 6 millimetres of Depron foam and another three layers of fibreglass.

For the control surfaces, the inner structure of the ribs were made out of balsa wood, stiffened by strips of carbon fibre at the spar. Balsa wood is very light and easy to use for small part shaping. Because balsa wood is very flexible, strips of carbon fibre were used to stiffen the balsa wood and make the control surfaces stiffer.

The mould used to manufacture the skins of the main wing and the winglets for the aircraft are made from SikaBlock M700⁴, which were CNC machined according to the CATIA design to obtain the correct shape. These blocks were glued together into a left and right part of the wing. The left and right part were bonded together using polystop to ensure a vacuum bond. This bond was brittle enough to separate the moulds from each other in case this was required.

2.1.3. Vacuum Assisted Resin Transfer Moulding

For the manufacturing of the parts, the method of VARTM (Vacuum Assisted Resin Transfer Moulding) was used. VARTM is a method where first a lay-up of a product is made, followed by resin infusion using vacuum. After the infusion is completed, the part is cured for 24 to 28 hours. For the resin infusion, a mixture of epoxy and hardener was used.

The lay-up of the parts was performed by using either the SikaBlock moulds described in section 2.1.2, or flat aluminium plates. The main wing skin and the winglet skin were infused using the moulds, the big and small panels for the ribs and spars were infused using the flat aluminium plates. Before the lay-up was performed, the surface of both the moulds and the aluminium was sanded to ensure a smooth surface roughness. Then, it was cleaned with acetone or ethanol to remove any of the dust from the grooves between the grains. After this, the surface was treated with a Marbocote release agent⁵, which was used to separate the laminate from the mould or plate.

When the surface of either the mould or the plate had been treated with the release agent, the laminate was made. The laminate was made from three layers of fibreglass, a layer of foam and

³AIREX C70 PVC foam, URL: <https://www.3accorematerials.com/en/products/airex-foam/airex-c70-pvc-foam>, visited on: January 21st, 2019

⁴SikaBlock M700, URL: https://advanced-resins.sika.com/gbr/en/solutions_products/product-groups/block-materials/model-and-tooling-boards/sikablock-m700.html, visited on: January 21st, 2019

⁵Mould Release Agents for Composite, URL: <https://www.marbocote.co.uk/products/mould-release-agents-for-composite-components/>, visited on: January 21st, 2019

another three layers of fibreglass. On top of this went peel ply, perforated foil and flow-mesh. The borders of the mould or plate were enclosed by tacky tape, which created a perfect airtight seal with the vacuum foil to create a vacuum. The inlet was connected to the flow-mesh and the outlet was connected to the breather, which as in contact with the laminate. Though the foam, holes were drilled to construct a resin connection between the upper and lower fibreglass layers.

Before the infusion of the resin, the vacuum bag was thoroughly tested for leakages. A test was always performed at about 5 millibars, at which the vacuum pump was closed and the leakage was tested. A tolerance of 1 millibar per 5 minutes was allowed to limit leakages and air bubbles inside the product. Before the leakages were tested, the pump ran for about 30 minutes to ensure almost all the air was removed from the product.

As the leakage testing was completed, epoxy and hardener were mixed to make the resin for the infusion. For the mixture, about 77% of the mixtures mass was epoxy and about 23% of the mixtures mass was hardener. After mixing, the mixture was put under vacuum for the degassing of the resin. This was done to eliminate all remaining air bubbles from the resin to enter the product. After 30 minutes of degassing, the resin was infused into the product by keeping the vacuum onto the product. The velocity of the resin was regulated by opening and closing valves to ensure the product was completely infused. After the resin was infused, all valves were closed and the product cured for about 24-28 hours. An impression of the infusion can be found in figure 2.3.

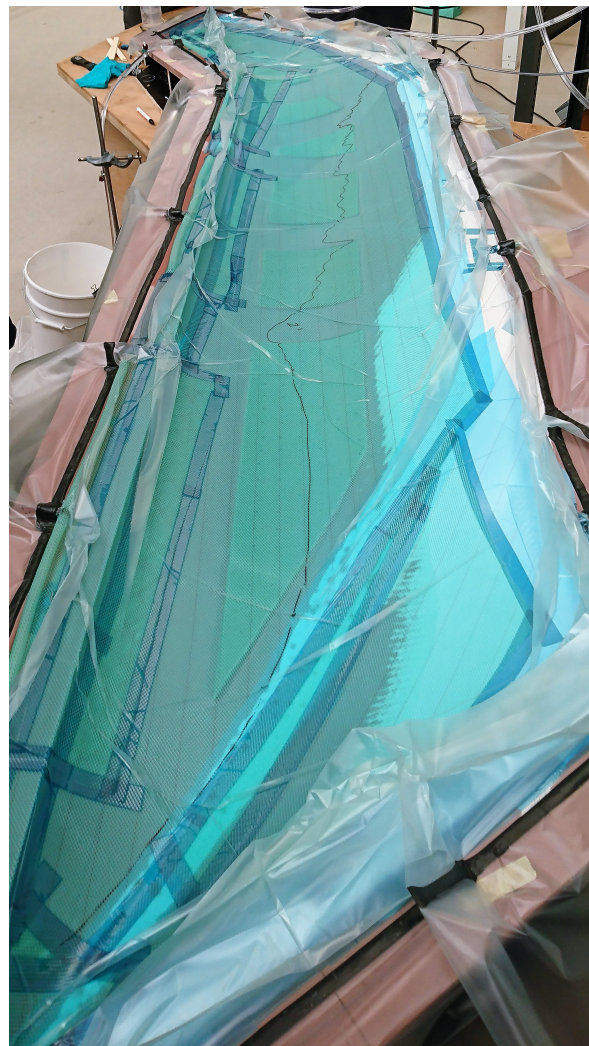


Figure 2.3: Infusion of the upper wing skin

2.1.4. Assembly

After all parts had been manufactured, the half-model of the aircraft was assembled. First, the lower wing skin was placed inside the mould to create a solid base which could not be deformed while working on the part. From this point onward, the edges of the laminate were trimmed and the spars and ribs were fitted and positioned in the correct location. The ribs and spars were sanded with the correct cant angle, so it perfectly fitted the curvature of the wing skin. An impression can be found in figure 2.4.



Figure 2.4: Spars and ribs fitted in the lower wing skin

From this point onward, the electronics were installed and the upper side of the wing skin was glued to the ribs and spars. This can be found in figure 2.5. The gluing of the two wing skin shells was performed while the lower shell was still inside the mould. The ribs and spars were sanded and canted into the correct angle with respect to the upper wing skin shell. Furthermore, a bonding strip of balsa wood was glued onto the leading and trailing edges that created an additional bonding area. The advantage of this extra bonding area was that during the wind tunnel experiment, the leading edge was less prone to rip the two wing skin shells off each other. The bonding procedure was performed using a vacuum bag, to ensure a distributed and equal pressing force all over the surface area. After the half-model had been glued together, the surface of the wing was sanded to ensure a smooth surface roughness. Furthermore, the leading edge and the trailing edge were sanded to provide a smooth transition from one wing skin to the other. In the figure, the structure for the control surfaces can be found as well.

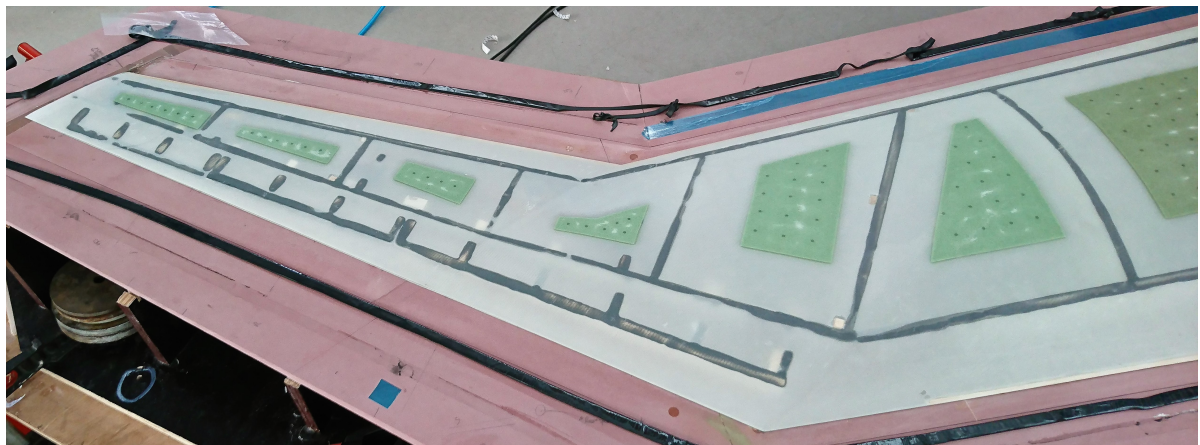


Figure 2.5: Closed wing skin

For the control surfaces, the structure was made out of balsa wood and already glued into the two shells to preserve the correct shape as they were cut. The cutting of the control surfaces led to the possibility to modify the control surfaces by adding a circular nose to the leading edge and hinges from the leading edge of the control surface to the rear spar of the main wing. The cut out of the control surfaces can be found in figure 2.6.



Figure 2.6: Cut out of the control surfaces

After the control surfaces had been cut from the main wing, inserts into the wing skin had to be made. This was to allow the control horns of the servos from inside the closed shell to stick out and make a connection with the control surfaces. The circular nose at the leading edge of the control surfaces were made out of balsa wood, which can be found in figure 2.7. This way, the nose was easy to modify into shape and ensured a perfect fit of the control surfaces to the main wing.



Figure 2.7: Control surface with a balsa wood leading edge

After the control surfaces had been fitted to the main wing, the servos were tested to measure the excitation of the control surfaces. During the test, it turned out that the servos allowed to have deflections from -125% up to +125%. The percentages were modified and tuned such that the controller delivered the same deflection for all the control surfaces. The same configuration is required for the flying model to ensure similarities between the deflection angle of the half-model and the full-model, as they will be built separately from each other.

During the first campaign, it turned out that the oil flow visualisation did not give the expected results, as explained in section 2.2. To solve this, between the first and second wind tunnel campaign, the surface of the half-model was painted with black paint. During the first campaign, the surface of the half-model was only sanded and unpainted. The painted version of the half-model provided a smoother surface roughness and a better contrast for the pictures taken during the oil flow experiments. The fluorescent dye lighted up brighter and therefore the quality of the results was improved.

2.2. Wind Tunnel Testing

A wind tunnel experiment is the main method after designing the Flying V to verify that the aircraft meets the aerodynamic expectations. This is because using CFD, the high angles of attack are not simulated well due to uncertainties in the turbulence models towards vortices and separation. In this chapter, the goals, set-up and expected results of wind tunnel experiment are described. To give a clear overview of how the chapter is divided, the section is started by explaining the goals of the wind tunnel experiment in section 2.2.1, followed by the set-up in section 2.2.2, the flow measurement techniques in section 2.2.3 and the expected outcome of the results in section 2.2.4.

2.2.1. Goals of Wind Tunnel Experiment

The goal of wind tunnel experiment was to acquire an accurate quantitative aerodynamic representation of the flight characteristics of the Flying V. It is important to know the flight characteristics to identify the capabilities of the aircraft during high angle of attack and approach speed conditions, to see its shortcomings and its strengths. The main goal of the wind tunnel experiment was to acquire data which led to an estimation of the maximum lift coefficient, provided a visualisation of where at different conditions the air separates from the surface of the aircraft, what the lift and moment behaviour of the aircraft is, to show the influence of the control surfaces onto the lift and moment of the wing at various flying conditions, to estimate the approach and stall speed and to estimate the optimal centre of gravity location for a trimmed and statically stable flight.

2.2.2. Wind Tunnel Set-Up

The wind tunnel experiments for the assessment of the flight characteristics of the Flying V were held at the Open Jet Facility wind tunnel (OJF) of the Delft University of Technology [21]. An impression of the wind tunnel can be found in figure 2.8. The Open Jet Facility is a closed loop wind tunnel with an octagonal test section of 285×285 cm (W×H). The room itself where the half-model was placed in, is a room of 13×8 meters (W×H). The flow was accelerated by a large fan which was, propelled by a 500 kW electric fan, generating a maximum velocity of 35 m/s. After the fan, the flow passed through a diffuser and turned twice in a 90 degrees angle by two columns of corner vanes. Then, the flow passed through another short diffuser and entered the settling chamber. Five fine-mesh screens provided the airflow to reduce its turbulence and velocity deviations. Then, via contraction, the air was blown into the test-section. At the end of the test section, the flow was cooled by a large radiator and was guided back to the fan by another set of two 90 degrees corner vanes.

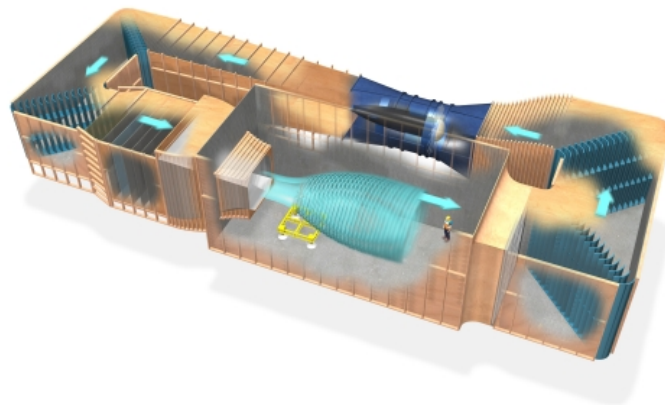


Figure 2.8: Impression of the Open Jet Facility ⁶

⁶TU Delft - Open Jet Facility, URL: <https://www.tudelft.nl/en/ae/organisation/departments/aerodynamics-wind-energy-flight-performance-and-propulsion/facilities/low-speed-wind-tunnels/open-jet-facility/>, visited on: January 21st, 2019

In the wind tunnel itself, a six-axis balance was used in order to measure the forces and moments in and around the x-, y- and z-axis. The balance digitally provided data to the computer, which saved all data such that it could be investigated at a later moment. The balance recorded the forces and moments for a time length of thirty seconds. This way, the fluctuations in the data were averaged out over the other data points.

The balance was put onto a turntable, which set the angle of attack during the experiment. The turntable was controlled from a computer in the control room. In here, the angles were set and maintained while the balance measured the forces and moments. The turntable was actively adjusting the angle of attack and was not locked, therefore small fluctuations during the measurement occurred, but were also cancelled out as the balance took the average over time as the recorded value.

The turntable and the balance were put onto a flat table, which could be moved around the floor and be raised in order to match the height of the jets floor. The flat table provided a solid base that did not move during the experiment. On top of this table, a set-up with a frame was built where the splitter plate was put. The splitter plate was put into the flow to remove the boundary layer of the jet from the measurement. The splitter plate had an aerodynamically shaped leading edge that decreased the tendency to separate the flow and increase the boundary layer over the plate.

Underneath the splitter plate, another plate was positioned which was in line with the floor of the jet. This way, the balance was not in direct contact with the flow from the jet to minimise noise and false data. From the balance, a strut support was built through holes of both plates to mount the half model. The half model was in contact with the balance through the support. In the first wind tunnel campaign, a triple strut support was used. After the test, it turned out that the support was not stiff enough in bending and torsion. For the second and third campaign this was solved by a new and stiffened support design. The supports were not in contact with the plates, to make sure no noise or false data was recorded. Around the support, a shield was built to eliminate any possible influences from the air to the data recorded by the balance. Furthermore, it was made sure that as the turntable turned the support, plates and half-model, no contact to the support and half-model was made and they could rotate freely. Because of this, external influences onto the balance measurements were minimised and only data from the half-model was taken. An impression of the set-up can be found in figure 2.9 through 2.13. In figures 2.14 through 2.17, schematic geometry and dimensions of the set-up can be found.

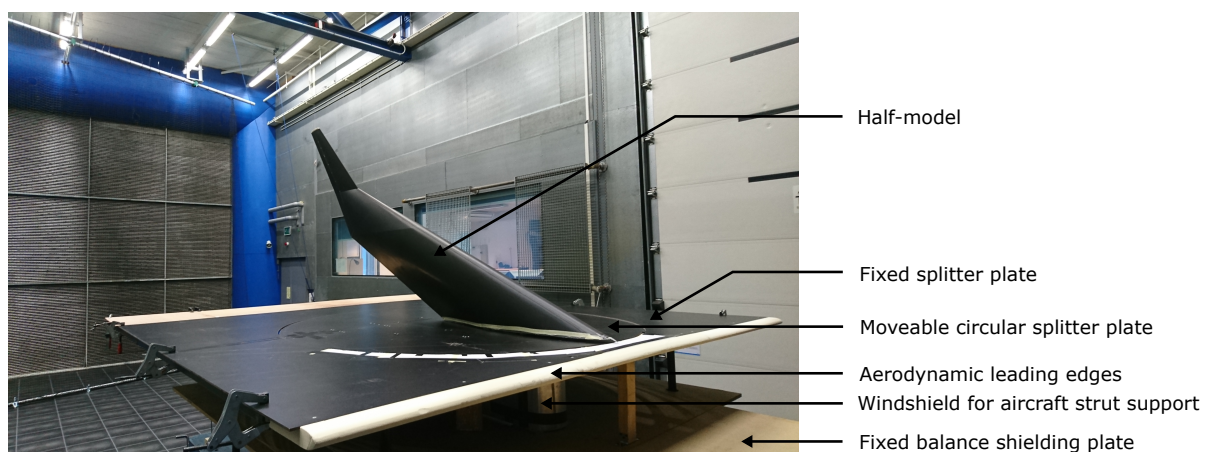


Figure 2.9: Set-up for the wind tunnel experiment with the half-model mounted

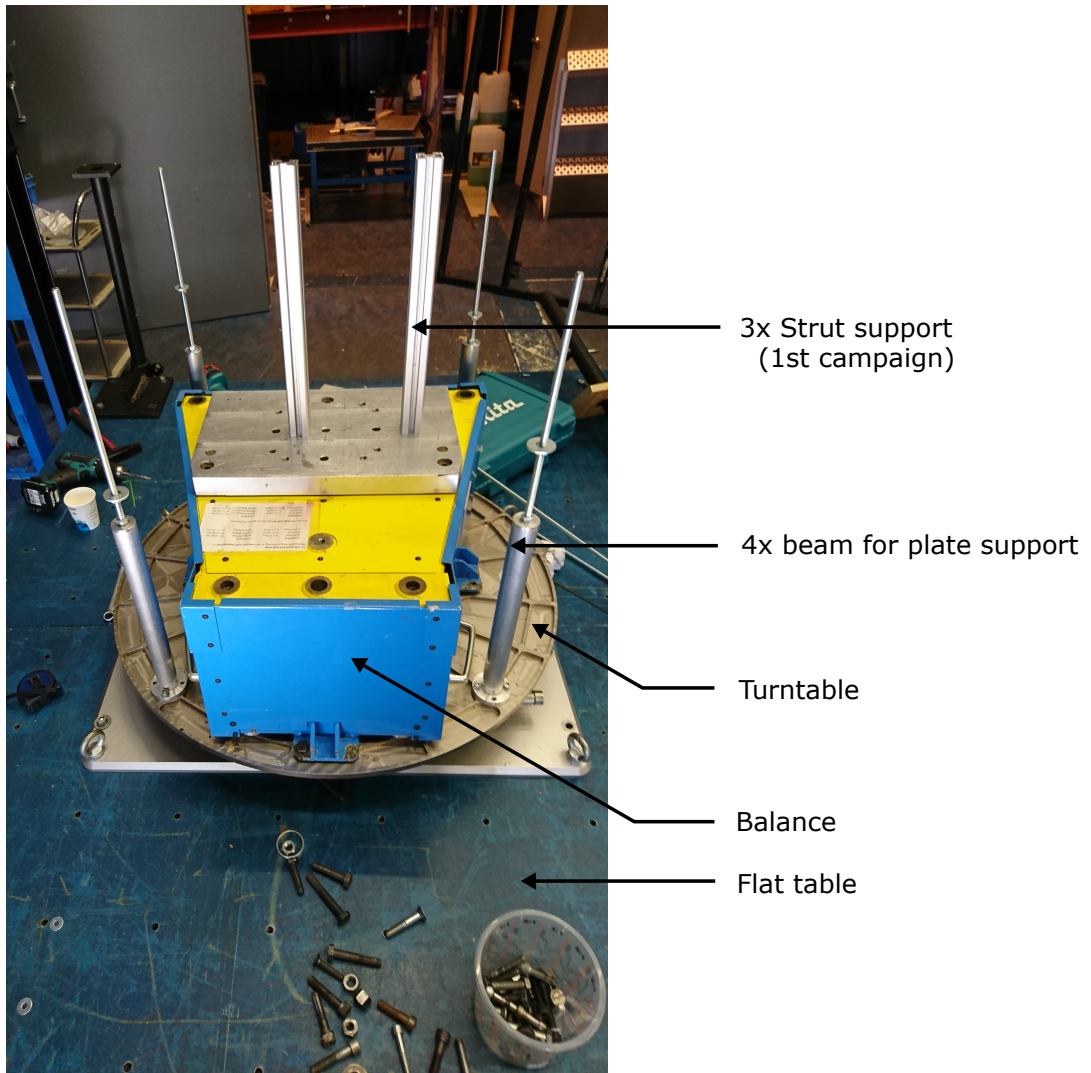


Figure 2.10: First campaign support set-up

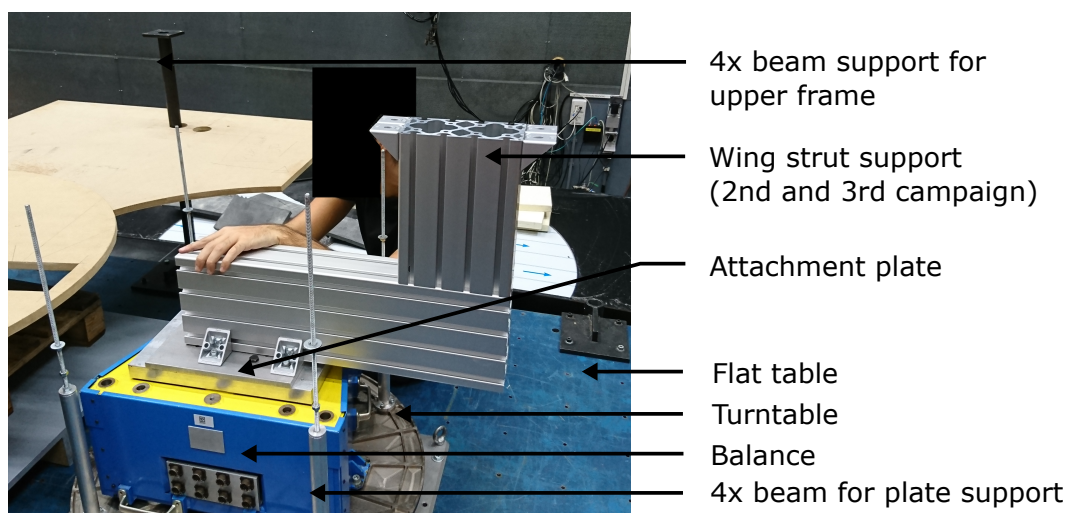


Figure 2.11: Second and third campaign support set-up

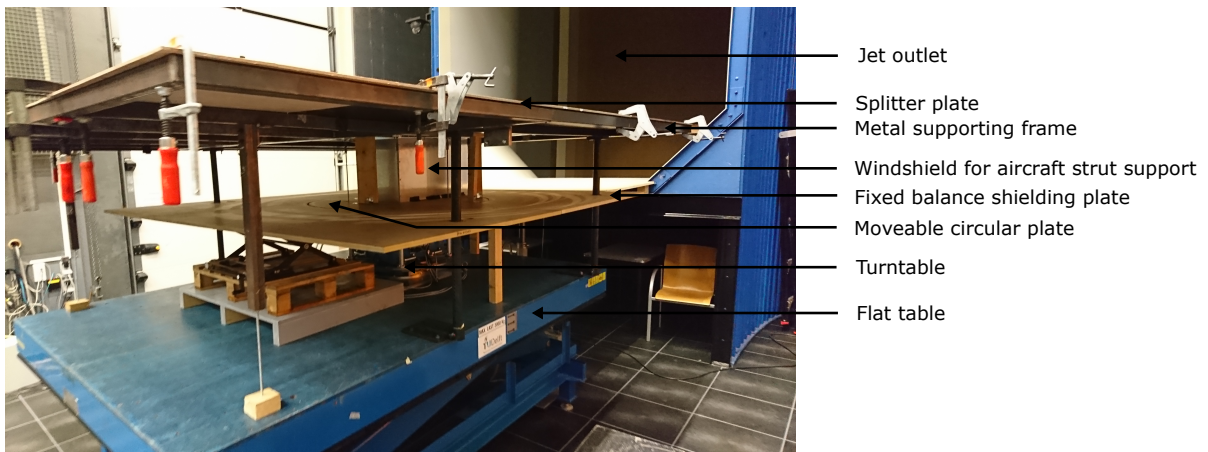


Figure 2.12: Lower view of the set-up for the wind tunnel experiment

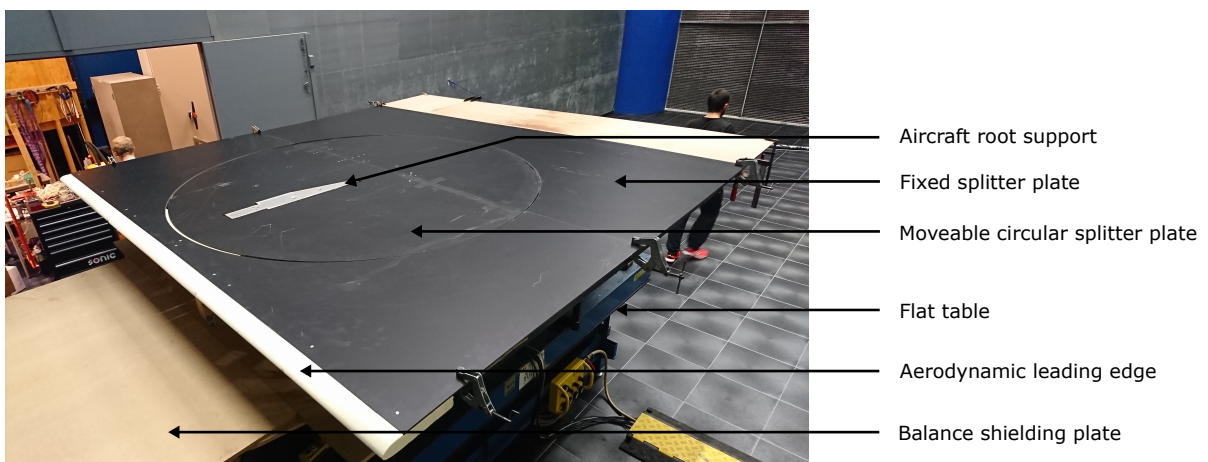


Figure 2.13: Upper view of the set-up for the wind tunnel experiment

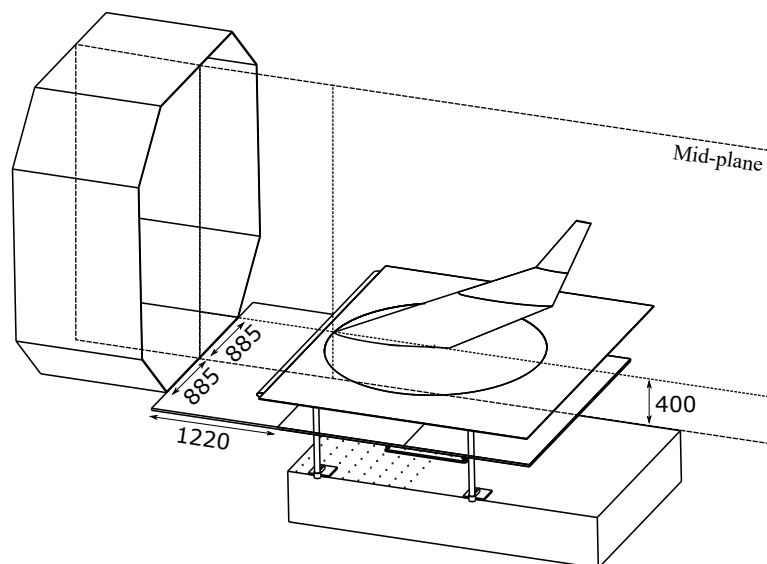


Figure 2.14: Schematic isometric view of the set-up used during the wind tunnel experiments [22] (Dimensions are in millimetres)

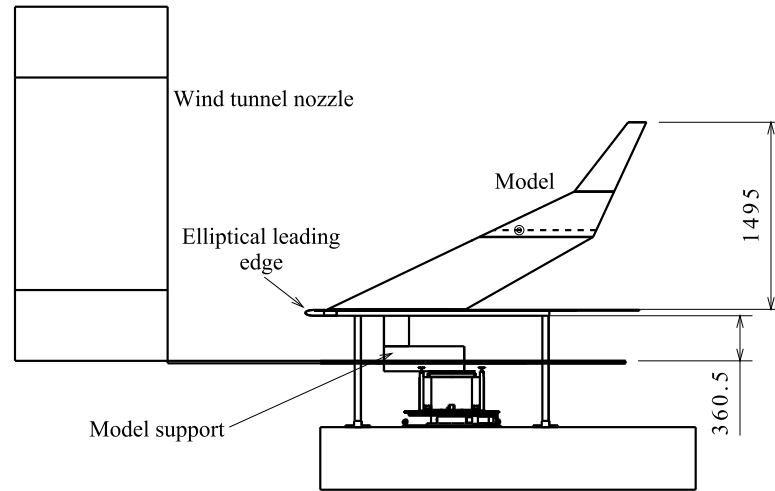


Figure 2.15: Schematic side view of the set-up used during the wind tunnel experiments [22] (Dimensions are in millimetres)

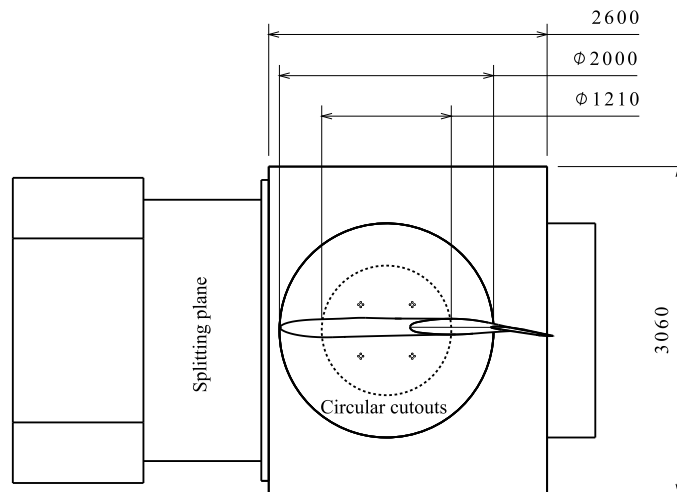


Figure 2.16: Schematic top view of the set-up used during the wind tunnel experiments [22] (Dimensions are in millimetres)

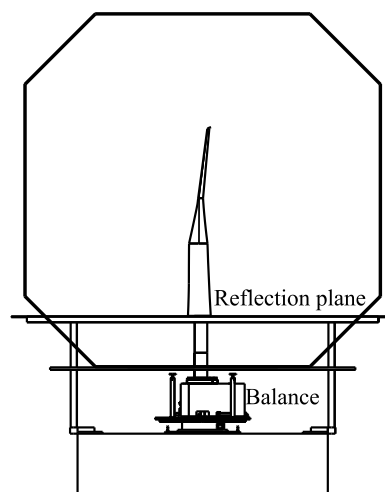
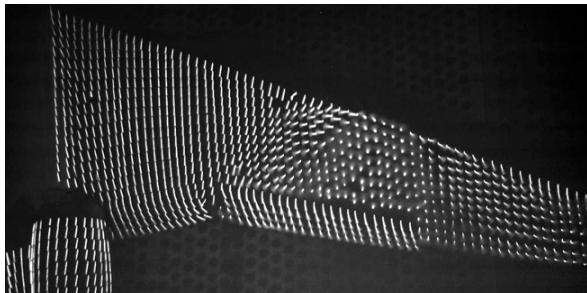


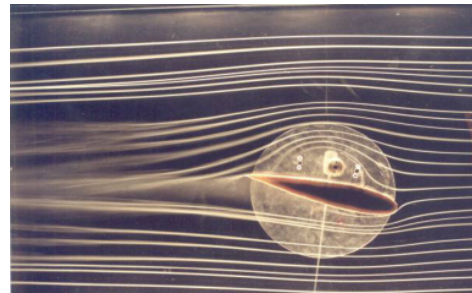
Figure 2.17: Schematic rear view of the set-up used during the wind tunnel experiments [22] (Dimensions are in millimetres)

2.2.3. Flow Measurement Techniques

To visualise the flow during the wind tunnel experiments, smoke, tufts and surface oil were used to provide information about the boundary layer of the flow ⁷. Impressions of these methods can be found in figure 2.18. Smoke is one of the oldest ways to visualise the flow behaviour. It can be used to show vortices and it can be used anywhere on and off the surface to visualise the flow. This can be seen as an easy and cheap way to diagnostically visualise the flow and can be inserted into the flow via a hollow wand. The disadvantages of using smoke are that this method does not work at velocities higher than about 480 km/h, it has to be introduced into the flow without disrupting the flow itself and that the smoke will leave a residue inside the wind tunnel and/or the aircraft model ⁸.



(a) Tuft visualisation on a wing ⁹



(b) Smoke visualisation on an airfoil ¹⁰



(c) Oil visualisation on a Blended-Wing-Body ¹¹

Figure 2.18: Measurement techniques of flow visualisation around a test object in a wind tunnel

Tufts are another method to visualise the flow. Tufts are made from nylon, polyester or cotton and are placed on the surface of the aircraft to show the air flow direction in the boundary layer just above the surface of the wing. The tufts always point into the direction the flow is moving and therefore it will be possible to visualise the streamlines of the flow. This method is an easy and cheap method as well and does not alter the flow if the tufts are from the correct material and length. To locally know the situation of the boundary layer, a tuft can be placed on a wand as well to manually set the desired location.

⁷Flow Visualization, URL: <https://www.grc.nasa.gov/www/k-12/airplane/tunvis.html>, visited on: January 22nd, 2019

⁸Smoke and Tuft Flow Visualization, URL: <https://www.grc.nasa.gov/www/k-12/airplane/tunvsmoke.html>, visited on: January 22nd, 2019

⁹Luminescent Mini-tufts, URL: <http://www.tsagi.ru/en/research/measurements/tufts/>, visited on: January 23rd, 2019

¹⁰SDSU Wind Tunnel Testing Facility, URL: <http://newscenter.sdsu.edu/aerospaceengineering/welcome.aspx>, visited on: January 23rd, 2019

¹¹Glow with the Flow, URL: https://www.nasa.gov/aero/flow_patterns_image.html, visited on: January 23rd, 2019

The method using surface oil is another method to visualise the flow ¹². Using this method, it is possible to show streamlines and boundary layer separation of the flow, as the oil is not able to penetrate the separation boundary. It has to be noted that the oil needs the correct lay-up thickness in order to create the best results. For the visibility of the oil, an ultraviolet dye was used which lighted up under a bright ultraviolet light source. Oil flow is used to show the direction of the wall shear stress vector on the surface of the model. While the experiment is ongoing, the oil will follow the wall shear stress vectors and develop long streaks. The dye inside the oil will either cluster together to indicate separation, or follow the long streaks to indicate the direction of the flow on the surface of the model.

The combination of these techniques will result in substantiation for the results found by the balance. The flow visualisation provides clear data on how the air behaves over the surface of the wing. Therefore this data can be taken as an argumentation into the discussion for the overall results and the findings from the balance results.

2.2.4. Expected Results

The balance results from the wind tunnel test will be raw digital data delivered in ".txt" files. This digital data will be recorded by the 6-axis balance and the Pixhawk controller ¹³, which records data from the control surfaces. The data will be provided in the order that is determined by the test matrices. The results need to be processed after the wind tunnel test in order to provide conclusions on what the lift and moment behaviour of the wing is. Furthermore, an analysis on the results from the flow visualisations will be made to understand the correlation between balance readings and the flow. Adding to this, the flow visualisations will provide insight into the boundary layer separation from the aircraft and if vortices are present over the wings. Photos and videos of this will be taken and lead to the support of conclusions to be drawn.

After the data has been processed, the expected results are figures for the lift curve, moment curve, centre of pressure location and neutral point location. It is expected that a clear lift gradient is shown for the nose-up motion and that a maximum lift coefficient can be seen. The moment curve will lead to an investigation into the optimal centre of gravity location and the effectiveness of the control surface for the stability of the aircraft.

From the balance results, the aim is to not only process the actual lift and moment data, but to get their derivatives as well. The lift slope and the moment slope (also known as the stability derivative) are needed in order to make predictions for the neutral point. Besides their need for the predictions of the neutral point, the lift and moment slope are important for the static stability of the aircraft as well. The investigation into the static stability will provide results which are directly related to the investigation into the centre of gravity location. The correlation between both the topics are used to draw conclusions for the flight characteristics of the Flying V.

¹²Surface Oil Flow Visualization, URL: <https://www.grc.nasa.gov/www/k-12/airplane/tunvoil.html>, visited on: January 22nd, 2019

¹³Pixhawk, URL: <https://pixhawk.org/>, visited on: January 23rd, 2019

3

Verification and Validation

Before the balance results were discussed in chapter 4, the balance data was verified and validated in order to show the accuracy and precision, as well as the repeatability and reproducibility of the data. Before the verification and validation was elaborated on, in section 3.1 the discussion on the wind tunnel corrections was made. Then, in section 3.2, the discussion towards the verification of the results was made. In section 3.3, the validation of the data was discussed.

3.1. Wind Tunnel Corrections

Before the data from the wind tunnel experiments could be used for the assessment on the aerodynamic characteristics of the wing, the raw data needed to be corrected in order to ensure precise and correct data. Data correction was applied for the bias during the experiment itself and for the three-dimensional flow of an open-jet wind tunnel. The bias corrections in section 3.1.1 were performed for the correction of the model and setup at a standstill, while the corrections for the open-jet wind tunnel in section 3.1.2 were based on the characteristics of the tunnel. Correction for the three-dimensional flow of an open-jet wind tunnel, the buoyancy, solid blockage, wake blockage, streamline curvature and the downwash corrections were taken into account, as discussed by Barlow *et al.* [23].

3.1.1. Bias Corrections

The bias corrections were divided into two separate methods. The first method was the method where the vibration induced bias error was taken into account, which was a correction for the dynamic bias error. As explained by Buehrle *et al.* [24], the dynamic bias error is determined by an algorithm which is dependent on the time and frequency domain. During the experiment, it was noticed that the vibrations on the wing could impact the results at a specific time. Therefore, it was made sure that the measuring time was set to thirty seconds. By doing this, a large single vibration or a multiple of it was cancelled out by the rest of the small vibrations during the measuring time, so that it did not impact the results.

The second bias correction taken into account was the deviation at the beginning and end of each run. To account for this bias correction, it was made sure that during all the experiments for each run a balance reading was made at the beginning and end of the run, making sure the wing was set at zero degrees angle of attack (AoA) with the flow velocity set to a standstill [25]. By looking at the data measured at the beginning and end of the run, it was seen that some small forces and moments were measured, even when the undisturbed flow was set to zero velocity. Therefore, for the data processing it was taken that the bias error increased linearly over time from the begin of the run till the end of the run. The equation from this linearly approach was then taken into account for each single measurement done during the run and was subtracted from the measured data. This way, the measured data during the run was not only corrected for the dynamic bias error correction, but as well for the static deviation approximated linearly over time from the static begin and end situation.

Furthermore, during the three wind tunnel campaigns the setup had been changed between the first and second wind tunnel campaign. During the first wind tunnel campaign, a triple strut support

was used to mount the wing to the balance. During the experiments it turned out that the triple strut structure was bending due to the forces acting on the wing. Not only did the support bend, it also twisted due to the bending moments caused by the forces on the wing. This resulted in a shift in local angle of attack, where the input angle set to the turntable did not result in the same angle of attack of the wing. During the entire first campaign, a needle was fitted to the nose of the wing to indicate the actual angle of attack the wing was facing during the experiments. This was done by a scale drawn to the splitter plate which did not move at any point during the entire campaign. As the velocity of the air was set to zero, a full angle of attack sweep was performed to mark the reference angle of attack of the turntable. During the experiments itself, it was therefore easily readable from a top view camera what the angle set to the turntable was (and thus the measured angle of the balance) and the actual angle of attack of the wing in the airflow. As the wind tunnel was running, an increase in angle of attack resulted in larger deviations between the actual angle of attack and the angle set to the turntable. This makes sense in the way that if the angle of attack is increased, the forces and moments acting on the wing are larger and thus that the support will bend and twist more. For the remaining two wind tunnel campaigns, the triple strut support was changed to a very stiff beam support, which did not allow the bending and twisting of the support anymore.

3.1.2. Open Wind Tunnel Corrections

As the bias correction was taken into account, the results also needed to be corrected for the wind tunnel used during the experiment. This correction procedure was performed according to the discussion of Barlow *et al.* [23]. The recordings from the wind tunnel needed to be corrected for in order to correct for any blockage and wall influences of the flow on the model. This influence leads to different results, as the flow behaves differently if it is blocked by the shield, or faces a different inflow incidence on the model by the model's wake interacting onto the side walls of the wind tunnel. For the correction of the Open Jet Facility¹, the dimensions of the jet were taken together with the rest of the wind tunnel dimensions.

For the derivation of the wind tunnel corrections, assumptions in the dimensions were made. The derivation made by Barlow *et al.* [23] assumed the model used is a full wingspan model with finite tips on both ends. Since the wing used in the wind tunnel is a half model, it is assumed and also suggested by Barlow *et al.* [23] to mirror the geometry around the symmetry plane at the root. This way, both the model and the tunnel are mirrored and thus twice as long. In figure 3.1 an impression of the mirror plane can be found.

First the solid blockage of the wing and the shield was calculated. The solid blockage of the wing can be seen as the blockage that the frontal area of the wing generates. This blockage then interacts with the surrounding flow by accelerating it according to the Bernoulli equation. The solid blockage of the wing and the shield was calculated according to equation 3.1.

$$\epsilon_{sb} = \frac{K_1 \cdot \tau_1 \cdot V_{w,s}}{C^{(3/2)}} \quad (3.1)$$

Based on this equation, the solid blockage of the wing was estimated to be 0.0064 and the solid blockage of the shield was estimated to be 0.0036. It has to be noted that the calculated blockages are for a closed wind tunnel. It is mentioned by Barlow *et al.* [23] that the open jet blockage factors can be taken as a fourth of the values calculated for closed wind tunnels. This means that the total blockage factor was equal to 0.0025. This blockage factor was taken to correct for the dynamic pressure from the jet exit. This definition can be found in equation 3.2.

$$q_c = q_a \cdot (1 + \epsilon_t) \quad (3.2)$$

¹Delft Open Jet Facility, URL: <https://www.tudelft.nl/en/ae/organisation/departments/aerodynamics-wind-energy-flight-performance-and-propulsion/facilities/low-speed-wind-tunnels/open-jet-facility/>, visited on: December 18th 2018

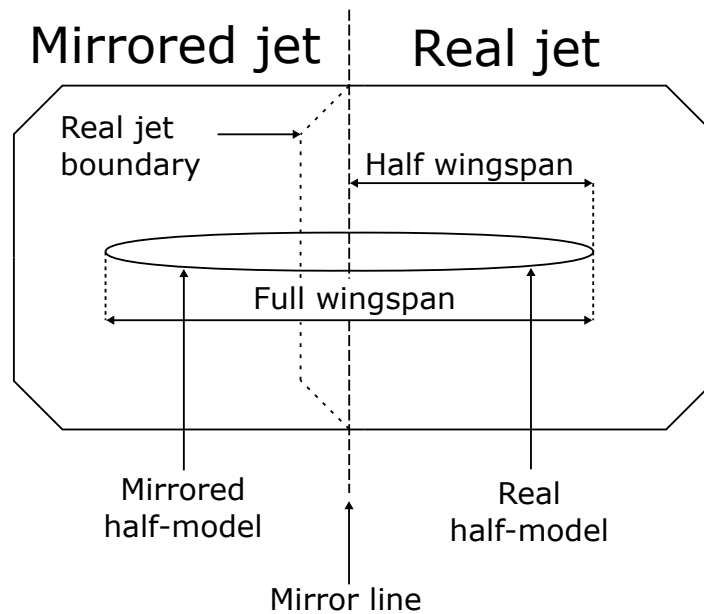


Figure 3.1: Impression of the symmetry plane of the tunnel and wing (not to scale)

The corrected dynamic pressure calculated in the equation was about 0.5% higher compared to the dynamic pressure recorded during the experiment. Given this fact, the lift coefficient for example decreased as a consequence of having a higher dynamic pressure with the same forces recorded.

Continuing on the blockages, the wake blockage is a blockage which is corrected for due to separated flows which influence the momentum effects outside the wake. The wake blockage was calculated by the definition given in equating 3.3 and 3.4. The wake blockage factor depends on the drag coefficients of the wing and the surface area of the wing to jet area of the wind tunnel. In equation 3.3, the last term represents the drag coefficient due to stall. This means that before separation occurs, this term vanishes and only the first term is applied in the calculations.

$$\epsilon_{wb} = \frac{S}{4C} C_{D_0} + \frac{5S}{4C} (C_D - C_{D_i} - C_{D_0}) \quad (3.3)$$

$$\frac{q_c}{q_a} = 1 + \frac{S}{2C} C_{D_0} + \frac{5S}{2C} (C_D - C_{D_i} - C_{D_0}) \quad (3.4)$$

For the wake blockage investigation, only the linear part is investigated where no separated flow is coming off the wing. Therefore the equations were reduced and led to a wake blockage factor of 0.0005. The correction for the dynamic pressure is a decrease of 0.10%. As the authors mention, in an open wind tunnel the sign of the wake blockage factor is reversed. Furthermore, it has to be noted that the given equations apply for a closed wind tunnel section. The authors do not have specific wake blockage equations for open wind tunnels, therefore it is mentioned that the wake blockage of open wind tunnels is smaller compared to closed wind tunnel sections. Given the fact that the wake blockage difference in dynamic pressure for closed wind tunnel without separated flow was about 0.10%, for the open wind tunnel this would even further reduce. Therefore, it was decided that the wake blockage correction was negligible and the dynamic pressure correction only applied on the solid blockage correction.

All the blockage factors were taken into account for the correction of the dynamic pressure. With this corrected dynamic pressure, the lift coefficient and the other aerodynamic coefficients used must be recalculated, as they all depend on the dynamic pressure. Given that the dynamic pressure was increased with about 0.5% and for example the lift coefficient is linear with respect to the dynamic pressure, the lift coefficient is decreased by about 0.5%.

Continuing on this, the correction for the blockage decreased the lift coefficient of the wing by the increased dynamic pressure. From this on, the downwash corrections could be taken into account.

The downwash correction was made in order to correct for the angle of attack due to the adjusted streamline curvature, as the angle of attack was increased. The method to correct for the downwash corrections was mostly correcting trailing surfaces, but since the Flying V does not have a trailing surface, the correction was only made for the wing itself. The correction was based on the geometry of the wind tunnel and the effective vortex span of the wing. Again, the dimensions were taken in such a way that the mirror plane at the root provided a complete finite aircraft.

From the book of Barlow *et al.* [23], the vortex span over the geometric span was estimated to have a ratio of 0.70, which led to an effective vortex span of 2.55 meters. Note that the wingspan of the wing itself is 3 meters, so the effective vortex span is smaller by almost half a meter compared to the wingspan of the model. The effective vortex span over the jet width led to a constant with a value of 0.52 and a jet height over width ratio of 0.58, which was used to derive the boundary correction factor from the figures from book. A summary of the values can be found in table 3.1

Table 3.1: Summary of dimensions used for boundary correction factor estimation

$\frac{b_v}{b}$ [-]	b_v [m]	b [m]	$\frac{b_v}{b_a}$ [-]	$\frac{h_a}{b_a}$ [-]
0.70	2.55	3.00	0.52	0.58

From the figures from Barlow *et al.* [23], three different values for the boundary correction factor were derived. The first boundary correction factor was -0.188, which was for an open rectangular jet with a model with uniform loading. The second boundary correction factor derived from the figures was equal to -0.165, which was for an open elliptical jet with a model with uniform loading. The last boundary correction factor was -0.165 as well, which was for an open elliptical jet with a model having an elliptical loading. The summation of the boundary correction factors derived from the figures can be found in table 3.2.

Table 3.2: Summary of boundary correction factors

	Boundary correction factor, δ [-]
Open rectangular jet, uniform loading	-0.188
Open elliptical jet, uniform loading	-0.165
Open elliptical jet, elliptical loading	-0.165

The wind tunnel used during the experiment featured an octagonal jet. As mentioned by Barlow *et al.* [23], the open octagonal jet can be approximated as an elliptical jet, given that the mirrored jet has a wider width than height. Therefore, it was chosen not to approximate the open octagonal jet as an open rectangular jet, but as an open elliptical jet. For the Flying V, it was given that the aircraft was designed with an elliptical loading [20].

The downwash correction for the model used during the wind tunnel experiment could be calculated by the definition given in equation 3.5. From this equation, it was seen that the downwash correction for the angle of attack was based on the boundary correction factor, the surface area of the wing with respect to the surface area of the jet and the lift coefficient of the wing.

$$\Delta\alpha_w = \delta \cdot \left(\frac{S}{C}\right) \cdot \left(\frac{180}{\pi}\right) \cdot C_{L_w} \quad (3.5)$$

Since the correction was based on the lift coefficient, the correction for the angle of attack of the wing gets larger as the lift coefficient increases. The change in corrected angle of attack of the wing over the lift coefficient of the wing was equal to a ratio of -1.26. This means that the correction in angle of attack for the wing only was equal to -1.26 times the lift coefficient of the wing. For the complete correction of the angle of attack, the angle of attack which was recorded during the experiment was

added with the correction for the angle of attack of the wing only and the correction in the angle of attack for the upflow. The correction in angle of attack for the upflow is assumed to be zero, as this value was not recorded during the experiment and was usually close to zero. Therefore, the total angle of attack correction for the wing only depended on the recorded angle of attack and the correction for the downwash of the flow. Furthermore, as the model did not have a tail or a trailing surface, the complete correction for the angle of attack was based on the angle of attack correction due to the downwash. Results showed that at maximum lift coefficient, the angle of attack is corrected by -1.4 degree, which is a maximum correction of about -3%.

For the corrections made, several assumptions had been applied. The most important assumptions were that the setup was mirrored over the root of the half wing in order to create a finite full wing span model which was usable for this method. Furthermore, the solid blockage factor was assumed to be about a fourth of the value calculated, as the equations used were for closed wind tunnels while for this experiment an open wind tunnel was used. Besides this, the octagonal jet of the wind tunnel was in the mirrored setup approximated as an elliptical jet. Next, the upflow of the wind tunnel was assumed to be negligible. As a last note, the model was used as a wing only model and that there is no correction on the wing due to any tail or other trailing surfaces.

Besides all the assumptions stated above, the authors from Barlow *et al.* [23] mention that the big differences between the methods shown in the book for closed wind tunnels and for the use of open wind tunnels are that the sign of the boundary correction factor changes and the blockage correction is a fourth of the one derived from the closed wind tunnel equations. The rest of the method for closed wind tunnels corrections is similar to open wind tunnels. A word of caution from the authors is that when using a splitter plate to shield the balance from the airflow is, the open wind tunnel is not completely open and should be approximated as one solid boundary tunnel. This method was discussed by Heyson [26, 27] and Ewald [28] and described how a splitter plate was used in a '3/4 method'. Because of the fact that the splitter plate was exactly in the mirror plane of the wing, it was assumed that the corrections made by Barlow *et al.* [23] were correct. As the splitter plate lied horizontal with the model standing vertical onto it at the root, the location and orientation of the splitter plate was therefore not influencing the downwash or the solid blockage factors.

The total corrections for the dynamic pressure and for the angle of attack, shown in table 3.3, were not very significant. Together with all the assumptions made to get to these values, it is arguable whether it is scientifically correct to continue with these corrections. Based on this, it was decided to not take any dynamic pressure and angle of attack corrections into account for the post-processing of the results from the experiments. The corrections made with respect to the bias were taken into account, which means the results shown in the upcoming sections are the raw data from the wind tunnel experiments.

Table 3.3: Summary of open wind tunnel corrections

Dynamic pressure, $\frac{q_c}{q_a}$ [%]	Angle of attack, $\frac{\Delta\alpha_w}{\alpha_u}$ [%]
+0.5	-3

Between the first wind tunnel campaign and the second and third wind tunnel campaign, the strut support between the root of the half model and the balance was changed, as was explained in chapter 2.2.2. The reason for the change in setup was due to the twist of the support when it was under load. The twist of the support made the support and wing touch the frame of the setup. This led to incorrect recorded data due to the interaction between the support and the frame. For the second and third wind tunnel campaign this problem was solved by a new and stiffer support design. Therefore, the external influences were limited and the recorded data was the actual data from the half model only. Due to the incorrect measured data from the first wind tunnel campaign, in the next sections the results from this campaign will not be discussed and are regarded as untrustworthy. Therefore, only the data from the second and third wind tunnel campaign will be used for this research. For future studies, it is recommended that the wind tunnel corrections are predicted with a more accurate model, such that the balance results from the experiments are more accurate.

3.2. Verification

As all results have been presented and discussed, the results also need to be verified and validated in order to ensure accuracy and precision. Where precision is a description on random errors, accuracy is a description on systematic errors like the bias error. The systematic errors can be reduced by ensuring the use of a calibrated balance and turntable, a stiff support and a high quality model.

The bias is taken into account during the experiment. Each time a new run was started during the wind tunnel test, a bias measurement was taken at zero air velocity and zero position of the turntable. At the end of the run a bias measurement was taken as well in order to see the drift of the sensors. The drift was taken into account by linear interpolation through time to compensate for the systematic bias.

In table 3.4 the maximum and standard deviation of the balance can be found [29]. As the balance is capable of measuring forces up to 250 Newton in the lift direction and 500 Newton in axial direction, the uncertainty is limited to 0.06% [30]. For the sake of the Flying V, this means that a 0.06% deviation in lift or moment recorded during the measurement results in a very small impact with respect to the real flight. As disturbances in the air during the flight may cause bigger influences to the model than the uncertainty errors of the balance, it is said the uncertainty error is acceptable for accuracy of the results.

Table 3.4: Standard and maximum deviation of the balance

	ΔF_x [N]	ΔF_y [N]	ΔF_z [N]	ΔM_x [Nm]	ΔM_y [Nm]	ΔM_z [Nm]
Max. deviation	0.06	0.23	0.16	0.05	0.05	0.25
Standard deviation	0.02	0.05	0.05	0.01	0.01	0.07

During the wind tunnel test, the random errors were hard to measure. To limit random errors, it is important to have a closed environment that minimises the influences from outside. Therefore during the test it was made sure that all doors were closed and no access from outside was granted during the runs without permission from the control room. Furthermore, the testing facility was thoroughly cleaned before the experiments were performed to prevent dirty flow and no obstructions were present to disturb the flow coming from the jet.

3.2.1. Tufts and Oil Flow Comparison

In order to verify that the results are as expected, a comparison for the tufts and oil flow with respect to the lift curve of the aircraft was made. This in order to show any differences and whether the differences are logical with respect to the expected outcome.

Looking into the behaviour of the tufts, results for a comparison are given in figure 3.2. As for some runs performed during the experiment, pictures of the tufts are taken. Therefore, it is important to know how the tufts influence the boundary layer in such a way that it is known how this changes the results with respect to the lift force. As seen in figure 3.2a, the difference in lift coefficient between the tufts-on and tufts-off wing are not major, meaning the influence of the tufts on the boundary is not impacting the results on a large scale. Looking into detail, it is shown in figure 3.2b that the lift coefficient with the tufts equipped over the full suction surface is slightly lower compared to the wing without any tufts. The average difference in lift coefficient is estimated to be around 0.01, which is negligible compared to the lift coefficient itself.

It is also observed that the difference in lift coefficient before the vortex lift becomes dominant is larger compared to the angles of attack where the vortex lift is dominant. In the region where the vortex lift is dominant, the lift decrease at the lift coefficient of 0.8 is estimated to be 2.5%. Around the maximum lift coefficient, the differences in lift coefficient because of the tufts get larger before the two curves overlap each other.

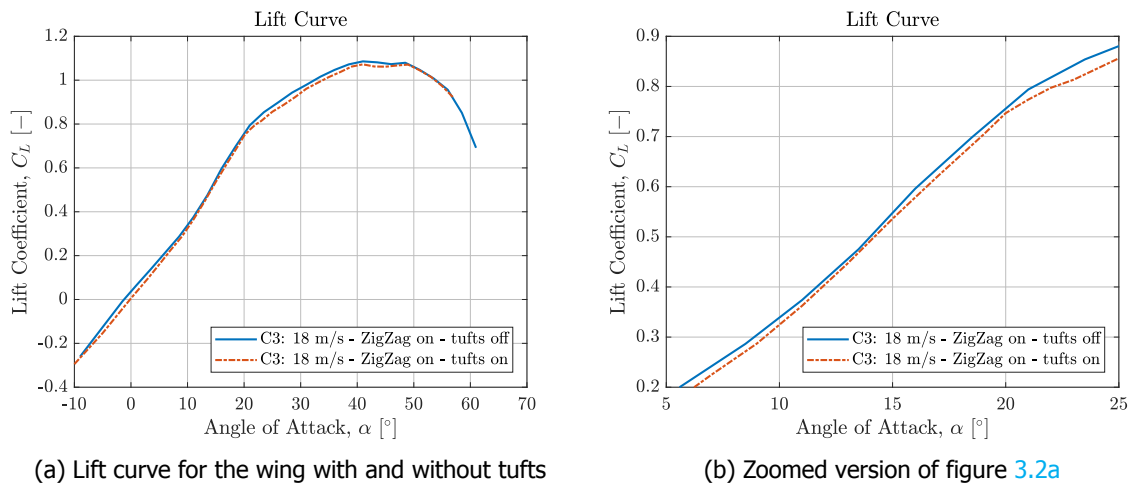


Figure 3.2: Comparison of the wings lift curve with and without tufts equipped

Based on the observations from the tuft experiments and their influence on the lift performances of the wing, a same comparison is made for the experiment where the wing is covered in fluorescent visualisation oil for the pictures taken in section 4.2.2. The comparison between the run with clean surface and the run where the oil is applied can be found in figure 3.3.

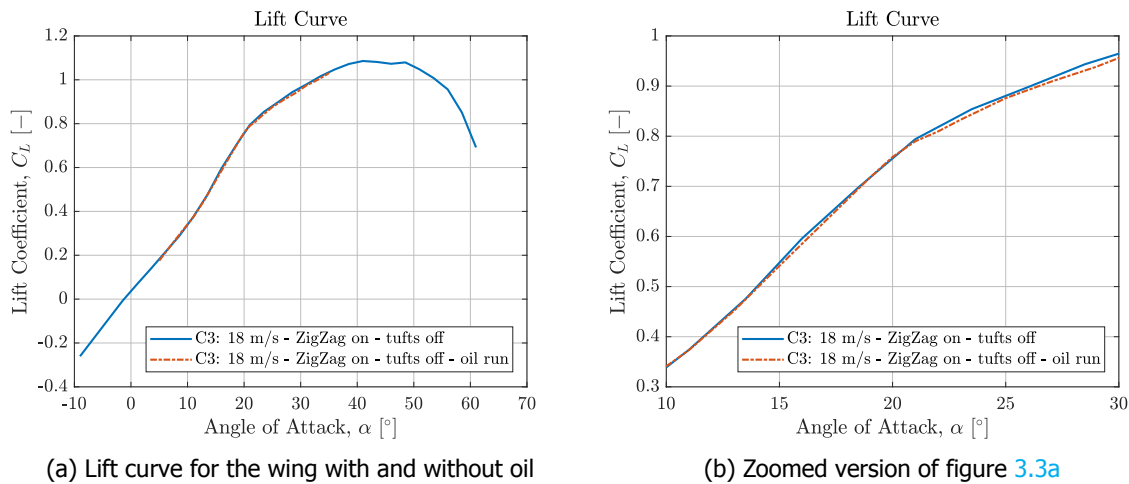


Figure 3.3: Comparison of the wings lift curve with and without visualisation oil applied on the surface

In this figure it is seen how the oil run affects the generation of the lift. The very thin layer of oil increases the dimension of the wing very minimalist. Together with this and the fact that the surface finish of the oil is very smooth, it does not have any influence on the lift characteristics of the wing. Also when zoomed in onto the curve, the differences are less than 1%. The only noticeable difference is that any disturbance during the run can be made to the wing or the support at the moment when the oil was reapplied. The data was recorded when the wing was untouched and stabilised, but even with this taken in mind there is no major difference spotted between the run with and without the oil applied.

3.2.2. Reynolds Number Effects

Looking into the effects of the Reynolds number, a comparison between four different velocities from the second wind tunnel campaign had been made. The comparison for the Reynolds number effect on the lift curve for the second wind tunnel campaign can be found in figure 3.4. In this figure the lift

curves for four different velocities at the second wind tunnel campaign is found, namely 15, 18, 25 and 30 meter per second. The corresponding Reynolds numbers at the MAC of 0.820 meter can be found in table 3.5.

Table 3.5: Reynolds numbers at the MAC of 0.820 meter

	$V = 15 [m/s]$	$V = 18 [m/s]$	$V = 25 [m/s]$	$V = 35 [m/s]$
Reynolds number, $Re [-]$	828.000	994.000	1.380.000	1.656.000

It was discussed by Jacobs and Sherman [31] that an increase in Reynolds number increased the lift coefficient. This was also explained by von Doenhoff and Tetervin [32] and Abbott *et al.* [33], where it was shown that the lift coefficient increased with increasing the Reynolds number due to a thinner boundary layer. Looking into the data provided, it is seen that with increasing the Reynolds number the lift coefficient was decreased. This is contrary, as it was expected that the lift coefficient would increase, instead of decreasing with increasing Reynolds number.

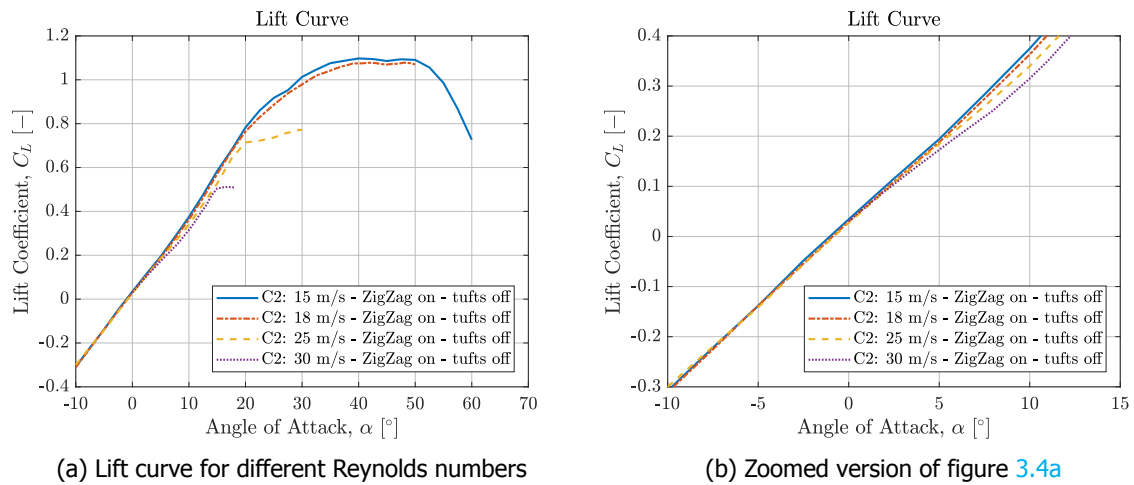


Figure 3.4: Comparison for different Reynolds numbers on the lift coefficient

Looking into the angle of attack, it is seen that for the 25 meter per second case, the lift curve abruptly changed slope at 20 degrees. The same occurred for the 30 meter per second case, but than at an angle of attack of 15 degrees. Also the maximum lift coefficient of the 15 and 18 meter per second cases were clearly not matched by the 25 and 30 meter per second cases. Looking into the lift slope in figure 3.4b, it is seen that at very low and negative angles of attack the lift slopes exactly matched each other. From the angle of 2 degrees onward, it is observed that the lift slope of the 25 and 30 meter per second case deviated from the runs performed at 15 and 18 meter per second. This again was not explained by the Reynolds number effect and the solution had to be found in the skin of the wing or the attachment plate touching the splitter plate. This makes sense by looking into the abrupt lift slope changes. The lift coefficient barely increased and this may be a sign of the model and the splitter plate touching each other. For the 15 and 18 meter per second case of the second wind tunnel campaign it can be concluded that the wing and the attachment plate did not touch the splitter plate, by the small deviation found between the results.

An explanation for the decreased lift coefficient might be found in the dihedral of the wing. The dihedral angle of the wing might have been increased by the bending of the support, or by the bending of the wing itself. For wings with dihedral, it is known that the stability will increase, at the cost of lift and drag [34]. Therefore, this might be an explanation for the additional generated lift by the increased dihedral angle.

3.3. Validation

For the validation of the balance data from the wind tunnel experiments, a standard deviation analysis was made to verify consistency of the data. This analysis gives an indication on the accuracy and precision of the data, as well as the repeatability and reproducibility of the data. The results of the standard deviation analysis can be found in figure 3.5.

By looking into the figure it is seen how the deviation varies with each angle of attack. The figure consists out of a weighted arithmetic mean for two data sets from the second and two data sets from the third wind tunnel test. For the processing of the results, it was made sure that each data point was recorded at the same angle of attack, at the same air speed of 18 meters per second and clean configuration. The vertical error bars visualise the deviation of three times the standard deviation. Using three times the standard deviation for a normally distributed data set, it is expected that 99.73% of all future recorded data fits within the upper and lower limit, provided that the exact same setup and aircraft configuration will be used. The averaged triple standard deviation over all angles of attack is estimated to be 0.016.

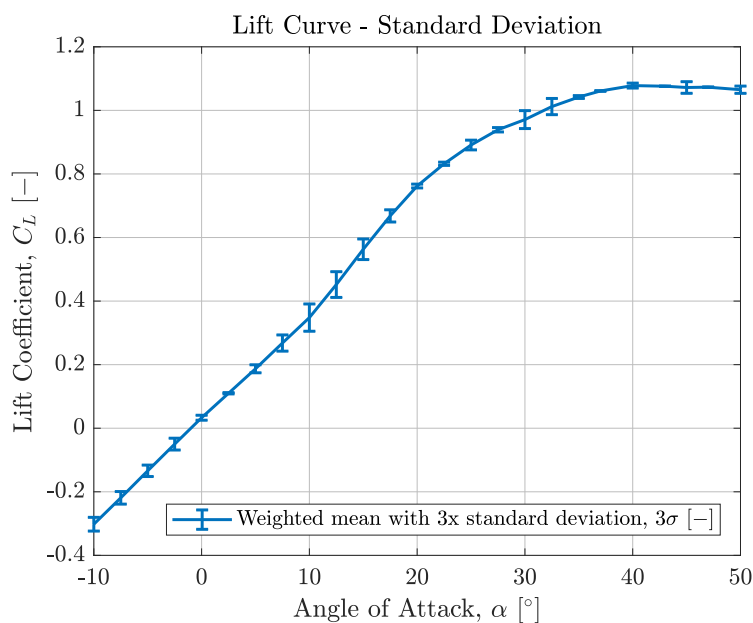


Figure 3.5: Standard deviation for the lift curve

The maximum lift coefficient is estimated within a 0.72% error margin using three times the standard deviation of 0.008, meaning the maximum lift coefficient is predicted with high accuracy. Around ten and thirty degrees angle of attack, the deviation gets larger. At ten degrees angle of attack the largest standard deviation is recorded, namely 0.043 for the triple standard deviation. This is an error margin of about 12.3%. At thirty degrees angle of attack, the deviation recorded is 0.028, which is about 2.90% using the triple standard deviation. At low angles of attack in the regime of the linear lift slope, the averaged triple standard deviation is estimated to be 0.014, which is slightly lower compared to the overall averaged deviation.

4

Wind Tunnel Results

During the wind tunnel campaigns, data was obtained from the 6-axis balance, the Pixhawk controller and from the oil, tufts and smoke visualisations. First, in section 4.1, the balance results will be discussed. This discussion provides the results from the data recorded by the balance on the lift and pitching moment. In section 4.2, the results of the oil, tufts and smoke visualisations will be presented and discussed.

4.1. Balance Results

During the wind tunnel experiments, three different wind tunnel campaigns were performed. The numerical data from the experiments was obtained in data sheets where the forces (F_x, F_y, F_z) in- and the moments (M_x, M_y, M_z) around the x-, y- and z-axis are listed. Besides this, data with respect to time (t), total temperature (T_0), total pressure (P_0), delta pressure ($\Delta P = P_0 - P$), undisturbed air velocity (V) and dynamic pressure (q) have been recorded. This data was taken to calculate and provide results with respect to the lift and pitching moment of the wing. First, as discussed in section 3.1, the raw data was corrected for the wind tunnel and setup used. Furthermore, the data from the first wind tunnel test was left out of the discussion, for the fact that external factors influenced the data recordings of the balance. After the correction had been applied, the results for the lift of the wing were provided in section 4.1.1, followed by an analysis on the pitching moment in section 4.1.2.

4.1.1. Lift Results

As the data had now been corrected for the bias, the first discussion made was to the lift of the wing. To calculate the lift from the balance results, first the data had to be converted from the balance axis system to the wings axis system. As the axis system of the balance rotated with the angle set to the turntable, it was assumed no correction had to be made for this. The balance rotated around its centre point and this was also where the support attachment was positioned. Looking into the wing, it was assumed that if the angle of attack was increased, the lift and drag parameters remained at a fixed angle, which had a reference angle set at an angle of attack of zero degrees. Therefore, the results of the balance needed to be converted to the axis system of the wing, as the reference angles of the balance to the lift and drag changed with each variation in angle of attack. The axis system is defined in figure 4.1.

In this figure it is seen that the 'x-axis' represents the x-axis of the balance and the 'y-axis' represents the y-axis of the balance. The angle of the balance is defined by the Greek symbol θ . For the second and third wind tunnel campaign, the angle of the balance was assumed to be identical to the angle of attack α of the wing. The equations for the calculations of the lift force and lift coefficient can be found in equation 4.1 and 4.2.

$$L = -(F_x \cdot \sin(\theta) + F_y \cdot \cos(\theta)) \quad (4.1)$$

$$C_L = \frac{L}{\frac{1}{2}\rho V^2 S} = \frac{L}{q \cdot S} \quad (4.2)$$

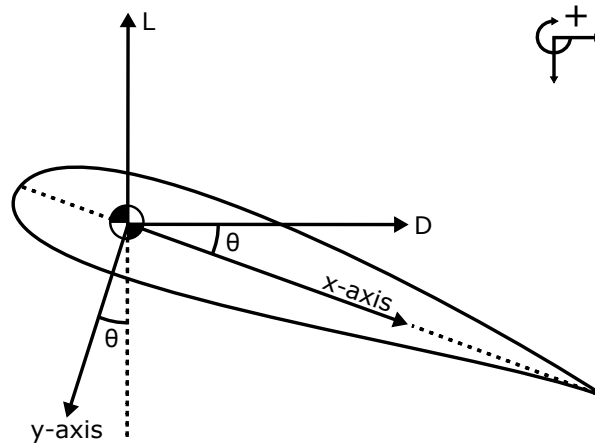


Figure 4.1: Lift axis system

Following equation 4.1, the forces F_x and F_y are set to negative, as the lift force is pointing in the positive upward direction and the reference system of the balance is in the negative downward direction. The equation for the lift coefficient shown in equation 4.2 is the simplified equation that results from the fact that the undisturbed air velocity during the experiment was much lower than the velocity where the compressibility effects had to be taken into account, $M < 0.3$ [35].

A comparison for the lift coefficient between the two wind tunnel campaigns can be found in figure 4.2. During the second (C2) and third (C3) wind tunnel campaign, the maximum velocity of 35 meters per second was achieved and experimental data for the lift was taken at 15, 18 and 20 meters per second. For the comparison of the data, the situation had been taken where on all cases a Zig-Zag strip was applied to the model and the tufts were not equipped.

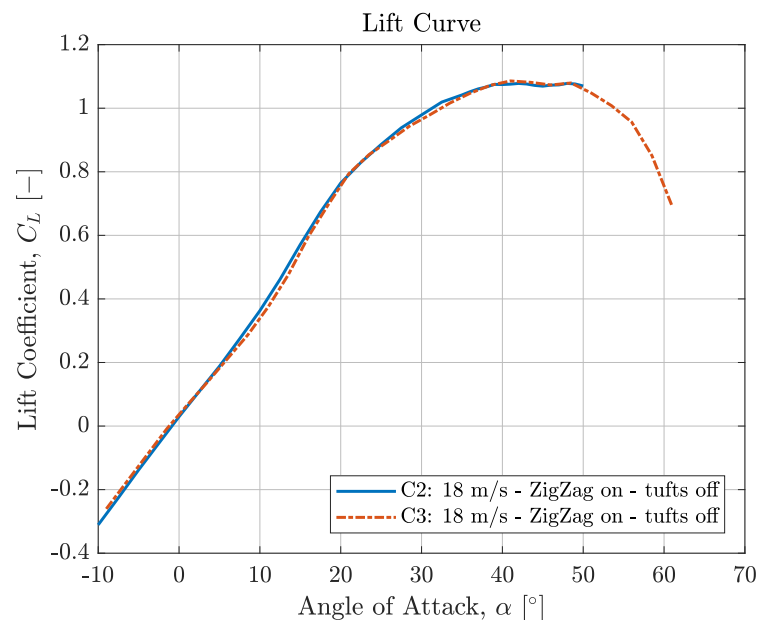


Figure 4.2: Lift coefficient comparison for each wind tunnel campaign

In figure 4.2, the maximum lift coefficient reached during the second and third wind tunnel campaign are about the same. The maximum lift coefficient is defined as the point where the aerodynamic forces acting on the wing generate the most lifting force possible for a specific angle of the entire range angles of attack. The exact numbers for the maximum lift coefficient and the angle of attack can be found in table 4.1.

Table 4.1: Maximum lift coefficient

	Maximum lift coefficient, $C_{L_{max}}$ [-]	Angle of attack, α [°]
Second campaign	1.08	42
Third campaign	1.09	41

After the maximum lift coefficient had been reached, both the lift curves decreased slightly in lift coefficient. However, at an angle of attack of 48 degrees, a lift recovery was noted where both the lift curves reached a lift coefficient of 1.08. This is explained by the complex flow showed in the oil flow visualisations in section 4.2.2, where it is seen that large leading edge vortices influence the separation of the boundary layer and the generation of lift. From this angle of 48 degrees onward, as was shown by the data from the third campaign, the lift coefficient reduced and the wing went into stall.

To provide more insight into the lift curve, an investigation into the lift slope of the lift curve was made. The lift slope was investigated by the increase in the lift coefficient over each degree in angle of attack. This is shown by equation 4.3. For the derivation of the data, the data of the lift coefficient was taken as a polynomial, which showed a norm of residuals of less than 4%. From this polynomial, the derivative of the data was taken and used for the lift slope. The unit of the lift slope is taken in $\frac{1}{rad}$, rather than $\frac{1}{deg}$.

$$C_{L\alpha} = \frac{\partial C_L}{\partial \alpha} \quad (4.3)$$

Based on the results of the lift coefficient from figure 4.2, the lift slope could be taken to show the findings for the lift gradient before the vortex lift becomes dominant and during the regime where the vortex lift is dominant. The results can be found in figure 4.3. At low angles of attack, it is seen from the figure that the lift gradient for the second and third campaign is constant. As can be seen in both figures, the lift slope increased at an angle of attack of 6 degrees and found its maximum vortex lift at an angle of attack of 12.5 degrees for the second campaign and 13.5 degrees for the third campaign.

Going beyond than this angle of attack, it was seen that at an angle of attack of 20 degrees for both the second and third campaign, the lift gradient was lower than the initial lift gradient before the vortex lift came into play. From this angle onward, the lift gradient decreased and therefore resulted in that the lift coefficient was increased at a lower rate. The decrease was linear until the angle of attack of 25 degrees, where the decrease reduced in magnitude in both the campaigns. The maximum lift coefficient was reached around the angle of 40.5 and 43.5 degrees for the second and third campaign respectively, by the indication that the curves crossed the zero gradient line.

It was also shown that the lift recovery noted in the lift curve was due to a change from a negative lift gradient into a positive lift gradient. After the recovery, the lift gradient became negative again and remained negative as the wing went into stall. In the figure it is shown that only the second campaign features this behaviour, while for the third campaign this was not the case. The reason for this is found in the approach of estimating the lift slope by a polynomial through the lift curve. This resulted in a shift of the maximum lift coefficient to 43.5 degrees and the neglect of lift recovery. The same applies for the second wind tunnel test, where the angle of attack of the maximum lift coefficient shifted from 42 to 40.5 degrees.

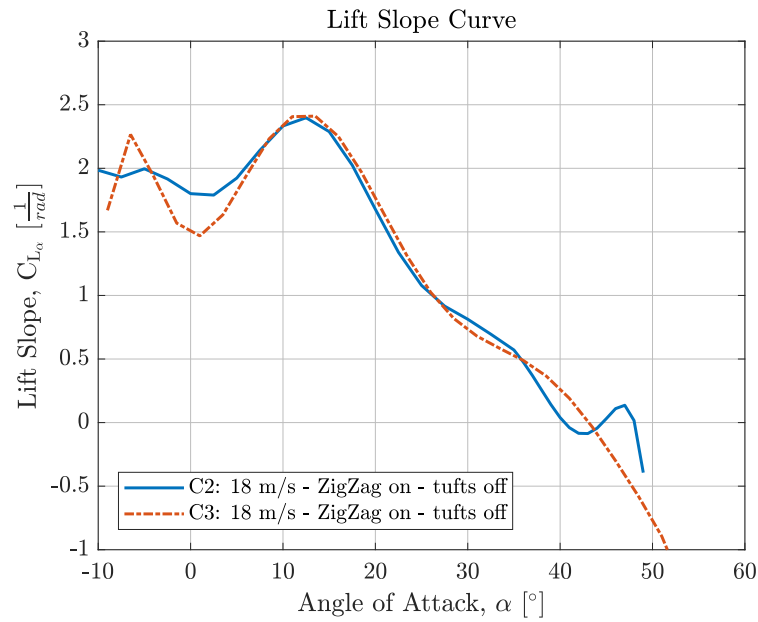


Figure 4.3: Lift slope comparison for each wind tunnel campaign

In table 4.2 the numbers for the lift slopes can be found. The first number is the constant lift slope at low angles of attack before the vortex lift came into play. The second value is the added vortex lift slope peak. The last value is the change in lift slope due to the vortex lift compared to the constant lift slope at low angles of attack.

Table 4.2: Lift slope coefficients

	Lift slope, $C_{L_{\alpha}}$ $\left[\frac{1}{rad}\right]$
Constant linear lift slope below 5° AoA	1.9
Vortex lift slope peak at $\approx 13^\circ$ AoA	2.4
Added lift slope due to vortex at $\approx 13^\circ$ AoA	0.5

As can be seen in figure 4.2, at an angle of attack of 10 degrees onward, the lift slope during both the campaigns started to increase. As will be explained later in chapter 4.2, this is due to the leading edge vortices which become dominant from this angle of attack onward and is called vortex lift. The increase in lift slope due to the leading edge vortices made that the lift coefficient at 21 degrees angle of attack was increased by about 19%. The added lift due to the vortices is defined by the formula given in equation 4.4.

$$C_L = C_{L_{\alpha}} \cdot \alpha + \Delta C_{L_{vortex}} \quad (4.4)$$

Another interesting discussion about the models results is the angle of attack range. Where a typical conventional aircraft like the Boeing 777-200 had its maximum lift angle between the 15 and 20 degrees angle of attack with high lift devices deployed, the Flying V did not show similar results [36]. Where the maximum lift angle of the Flying V lied around 40 degrees angle of attack, the results compared to conventional commercial aircrafts were that the angle of attack for maximum lift is about twice as large. A survey performed by Luckring [10] showed that a 50 degrees constant swept chord wing with a blunt ONERA D airfoil had its maximum lift attained at an angle of attack of about 30 degrees. The setup used showed that at a Reynolds number of $2.3 \cdot 10^6$ the maximum lift angle already shifted by more than 10 degrees compared to the study performed on the Boeing 777-200. As was researched by Luckring [10], the larger the sweep angle of the blunt airfoil wing, the larger the angle of attack at the maximum lift was.

4.1.2. Pitching Moment Results

The data regarding the pitching moment was recorded during the experiment in order to draw conclusions for the longitudinal flight capabilities of the aircraft. The lift results have already shown that the aircraft is able to create lift, but the pitching moment results should lead to whether this wing is able to be trimmed during flight. The investigation of the trimmed flight is discussed in chapter 5.2. This section is about the results with respect to a fixed pre-determined centre of gravity location at 1.234 meters behind the nose, which is exactly where the geometric mean aerodynamic chord is located. An impression of the location of the pre-determined centre of gravity can be found in figure 4.4.

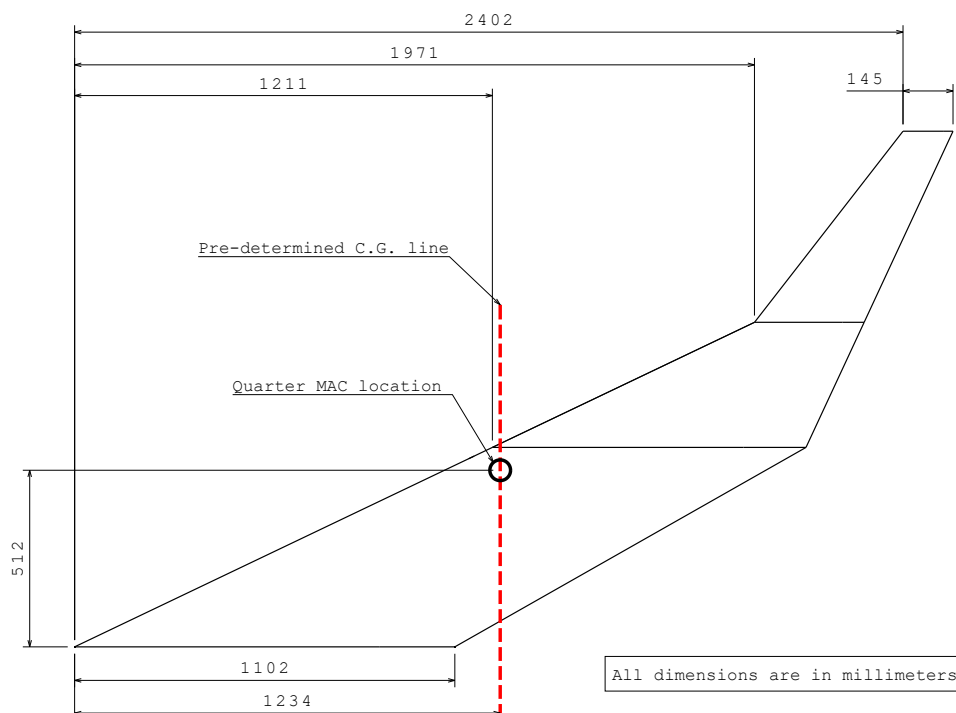


Figure 4.4: Pre-determined centre of gravity location

Following the same procedure as was done in section 4.1.1, first the axis definition was made followed by a set of equations to calculate the pitching moment from the recorded data around the centre of gravity. The definition of the axis system used for the equations can be found in figure 4.5. As can be seen in the figure, the axis definition was composed by a force and a moment. The force was taken by the forces in the x - and y -direction of the balance axis system, as defined in figure 4.1. The abbreviation ' x_{CoM} ' stands for the distance between the nose and the centre of measurement, with the centre of measurement being the location where the balance is positioned and recorded the data. The distance ' x_{cg} ' stands for the distance between the nose and the centre of gravity. Again, for this section the centre of gravity is positioned at a fixed location from the nose. The distance ' x_{cp} ' stands for the distance between the nose and the centre of pressure of the wing. This distance varies with the angle of attack, as the location of the sum of the forces moves with the angle of attack. It was assumed that the force in x -direction goes through the centre of gravity and the centre of measurement, eliminating any spacing and thus a moment. The moment located at the CoM is the moment recorded by the balance around the z -direction of the balance.

Looking into the definition of the equations for the pitching moment, the goal was to get the moment around the centre of gravity. Since the resultant force, the angle of the resultant force, the moment measured due to the resultant force around the centre of measurement and the distance between the nose and the centre of measurement were known, the distance between the centre of pressure and the nose could be calculated for each angle of attack. This definition can be found through equations 4.5 to 4.7. Then, as the location of the centre of pressure was known, it was possible to calculate the

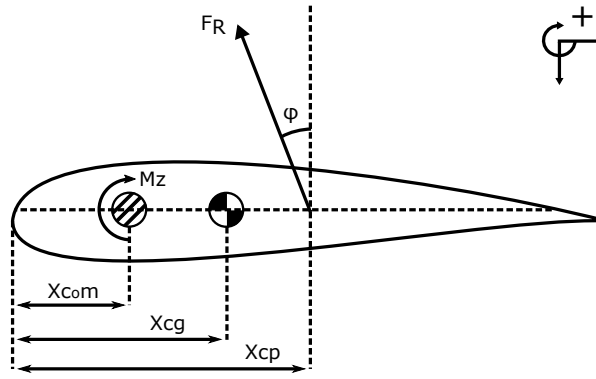


Figure 4.5: Moment axis system

moment around the centre of gravity, as the location of the centre of gravity was set at a fixed location. This definition can be found in equation 4.8. Then, the moment around the centre of gravity can also be written in a dimensionless form, given by equation 4.9.

$$F_R = \sqrt{L^2 + D^2} \quad (4.5)$$

$$\varphi = \theta - \tan^{-1}\left(\frac{D}{L}\right) \quad (4.6)$$

$$x_{cp} = \frac{-M_z}{F_R \cdot \cos(\varphi)} + x_{com} \quad (4.7)$$

$$M_{cg} = -F_R \cdot (x_{cp} - x_{cg}) \cdot \cos(\varphi) \quad (4.8)$$

$$C_{M_{cg}} = \frac{M_{cg}}{\frac{1}{2}\rho V^2 \cdot S \cdot \bar{c}} = \frac{M_{cg}}{q \cdot S \cdot \bar{c}} \quad (4.9)$$

For this discussion the control surfaces were set to zero deflection angle, which meant the pitching moment around the centre of gravity purely exists due to the lifting forces acting on the body. A comparison between the pitching moments can be found in figure 4.6. The location of the balance x_{com} was positioned at 1.065 meters measured from the nose. The x_{cg} distance used in the figure was taken at the quarter MAC location, now also referred to as $x_{\bar{c}/4}$. For both cases presented in the figure, the CG location was fixed at the quarter MAC location, at 1.234 meters measured from the nose.

As can be seen in the figure, the results between the second and third wind tunnel campaign were similar each other. The slope of both the curves had the same sign and about the same magnitude as well. The small differences between the second and third wind tunnel campaign could be explained by the position where the centre of pressure was located. Results of the centre of pressure can be found in figure 4.7.

As presented in the figure, the comparison for the location of the centre of pressure was compared for both the second and third wind tunnel campaign. The runs presented are from the same data set as presented in section 4.1.1, which makes comparison easier. It can be seen that around the angle of attack of zero degrees, the data plotted went into an asymptotic trend. This is explained by the fact that the force in y-direction of equation 4.7 went from negative into positive and therefore imposes the asymptotic limit.

It can be seen that the location of the centre of pressure of the second and third wind tunnel campaign were aft of the MAC location for angles of attack higher than five degrees. Although it is

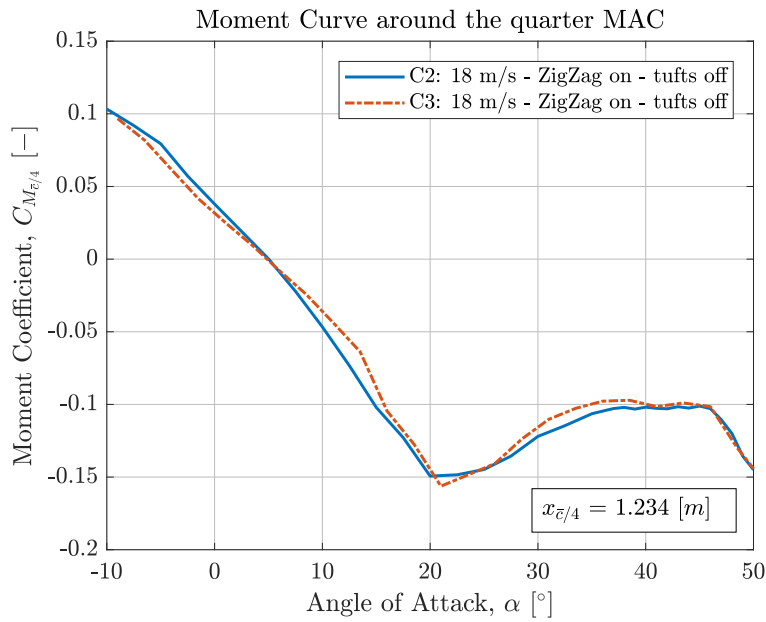


Figure 4.6: Moment coefficient comparison for each wind tunnel campaign

arguable whether the location of the centre of pressure was below the 1 meter for very low angles of attack based on the discussion of the asymptotic limits, the higher angles of attack showed a more accurate results. The location of the centre of pressure for the second and third wind tunnel campaign are between the 1.2992 and 1.3919 meters measured at angles of attack higher than ten degrees.

As can be seen in the figure, from the very small positive angles of attack onward, the distance of the centre of pressure went more towards the trailing edge. From 20 degrees angle of attack onward, the location of the centre of pressure went more towards the leading edge. This can also be directly seen in the moment curve in figure 4.6, where the tendency of a negative slope changed to a positive slope.

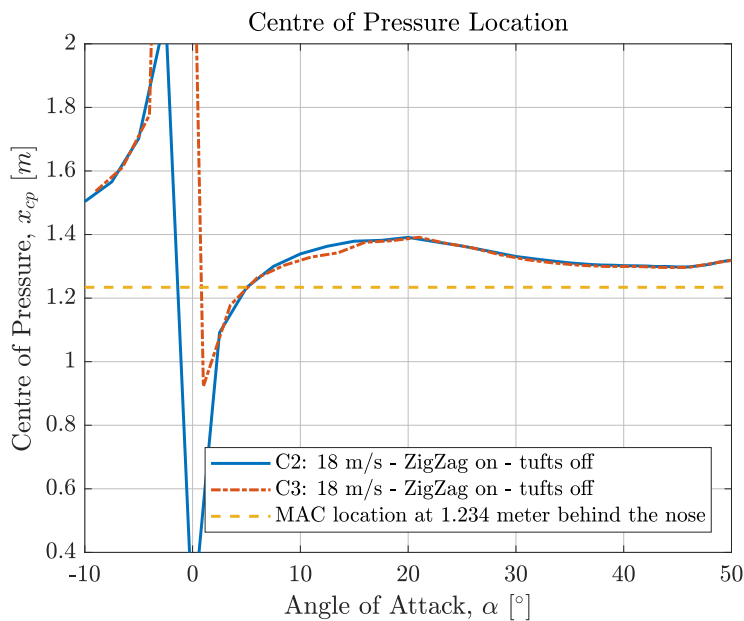


Figure 4.7: Centre of pressure location comparison for each wind tunnel campaign

Based on the moment coefficient, it was possible to look into the longitudinal static stability of the wing. This was done by comparing the moment coefficient and its slope. The slope of the moment coefficient is the derivative of the curve of the moment coefficient itself. This can be further defined as the change in moment coefficient with the angle of attack and is generally known as the stability derivative. The formulation can be found in equation 4.10.

$$C_{M_\alpha} = \frac{\partial C_M}{\partial \alpha} \quad (4.10)$$

Applying this equation to the moment coefficient shown in figure 4.6 leads to the stability derivative around the MAC location. The results with respect to the slope of the moment coefficient can be found in figure 4.8. For the curves presented in the figure, the same approach has been used as was elaborated on in section 4.1.1. First, a polynomial through the moment coefficient was taken. This showed a norm of residuals less than 4%. From this polynomial, the derivative of the data was taken and used for the lift slope. The unit of the lift slope is taken in $\frac{1}{rad}$, rather than $\frac{1}{deg}$. In this figure it can indeed be seen that the stability derivative for angles of attack below about 20 degrees angle of attack is negative. Angles of attack larger than about 20 degrees show positive trend up until the angle of about 40 degrees. This is also around the region where the maximum lift coefficient is reached, which is estimated at around 40 to 42 degrees angle of attack.

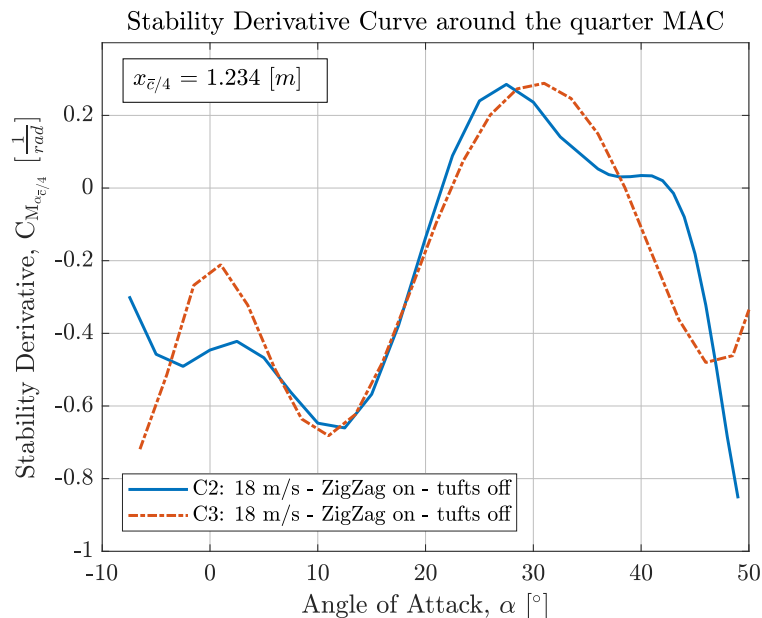


Figure 4.8: Comparison of the stability derivative for each wind tunnel campaign

Based on the sign of the stability derivative, it is possible to indicate whether the placement of the centre of gravity leads to a statically stable, neutral or unstable aircraft. The aircraft is said to be statically stable when the stability derivative is negative. This means that with increasing the angle of attack, the moment coefficient has a downward trend. If the stability derivative is equal to zero, the aircraft is said to be statically neutral. This means that an influence to the state of the aircraft will make an adjustment to the orientation of the aircraft, but that the aircraft will remain in the adjusted orientation if the state is not further influenced. The aircraft is statically unstable as the stability derivative shows a positive sign. This is seen in the moment coefficient curve as an increasing moment coefficient with increasing angle of attack [37].

Based on the theory of static stability of aircraft, the aircraft with the centre of gravity placed at a distance of 1.234 meters from the nose, which is the location of the geometric MAC of the aircraft, shows a statically stable behaviour for angles until the 20 degrees angle of attack. This means the aircraft is stable for any disturbances which increase the angle of attack of the aircraft. From this angle onward, the aircraft is unstable. From pilot point of view, an unstable model aircraft flown at low velocities is still flyable, while a real aircraft at very high velocities usually features an autopilot capable of flying unstable aircraft. As for this discussion the control surfaces are not taken into consideration and are put to zero deflection angle, the trim of the aircraft can only be discussed based on the placement of the centre of gravity. The trim of the aircraft with respect to the deflection of the control surfaces will be discussed in section 5.2. The dynamic stability of this aircraft is not taken into consideration for this discussion, as not enough data is provided.

Based on the findings from the stability derivative of the aircraft, it is possible to give a first indication of what to expect from the centre of gravity location. The position of the centre of gravity will make influences on whether the location of the centre of pressure provides a positive or negative moment around the centre of gravity. If the centre of gravity is placed behind the centre of pressure, the wing lift will create a positive moment around the centre of gravity. By turning this around, if the centre of gravity is placed in front of the centre of pressure, the wing lift will create a negative moment around the centre of gravity. For the Flying V with its highly swept flying wing layout, the centre of pressure will be more aft compared to non swept flying wings. As a result, the shape of the Flying V puts the centre of gravity more forward, while the centre of pressure is more aft and lies behind the centre of gravity. Therefore, it is investigated how the centre of gravity influences the moment coefficient and the stability derivative. This is done based on the neutral point. The neutral point is the point where if the centre of gravity is put at that point, the moment coefficient is equal to zero. This means, the aircraft is flying in its statically neutral position. This is possible by setting the summation of moments of the centre of pressure times the arm to the centre of gravity and the moment around the aerodynamic centre at zero lift to zero. By putting the centre of gravity in front of the neutral point, the wing has a pitch down moment. If the position is reversed and the centre of gravity lies aft of the neutral point, the wing has a pitch up moment. This way, the horizontal placement of the centre of gravity works as a stability measure. The definition for the location of the neutral point can be found in equation 4.11.

$$x_{np} = - \left(\frac{C_{M\alpha}}{C_{L\alpha}} \right) \cdot \bar{c} + x_{cg} \quad (4.11)$$

The equation depends on the slope of both the lift and the moment curve. This way, the neutral point, also referred to as the pitch stiffness, goes to zero if the centre of gravity is located at the neutral point [38]. It can also be seen that the pitch stiffness is proportional to the distance between the neutral point and the centre of gravity, also known as the static margin (SM). The static margin is usually expressed as the percentage of the distance between the centre of gravity and the neutral point, both divided by the MAC. This is also shown in equation 4.12.

$$SM = - \left(\frac{\partial C_M}{\partial C_L} \right) = \frac{x_{np}}{\bar{c}} - \frac{x_{cg}}{\bar{c}} \quad (4.12)$$

As a rule of thumb, the static margin of a conventional aircraft with the right amount of stability and manoeuvrability, the centre of gravity lies within 5%-15% ahead of the neutral point. If the centre of gravity is put further ahead of the neutral point, the aircraft will have more pitch stability, but less elevator authority. A centre of gravity location too close to the neutral point gives less pitch stability and more elevator authority. The data showing the neutral point can be found in figure 4.9.

From this figure it can be seen that the neutral point is very sensitive to separation on the wing, given the data fluctuates from about thirty degrees angle of attack onward. Given that the centre of gravity is placed at 1.234 meters from the nose, it shows that the centre of gravity is ahead of the neutral point for low angles of attack up to twenty degrees when the stability derivative is negative. By averaging the neutral point from zero to twenty degrees angle of attack, the neutral point for the second wind tunnel campaign lies at 1.422 meters behind the nose, while for the third campaign this

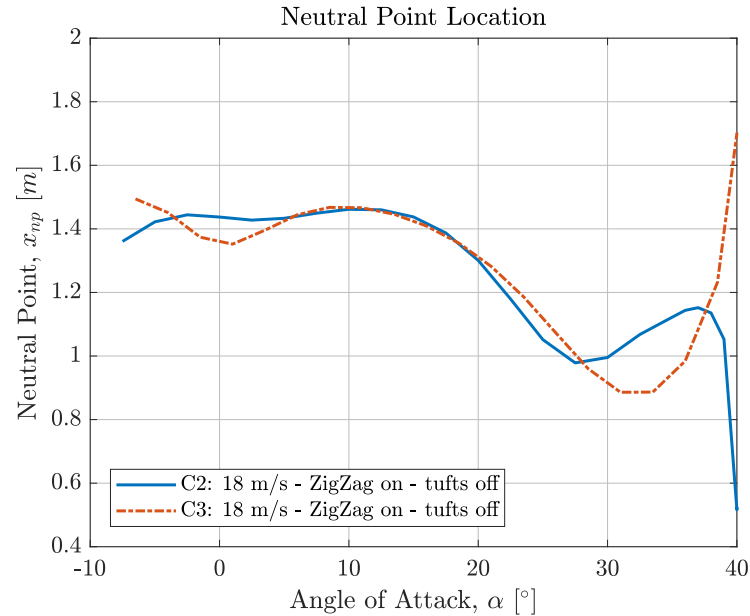


Figure 4.9: Comparison of the neutral point for each wind tunnel campaign

is averaged at 1.402 meters behind the nose. This provides a static margin of 22.87% and 20.48% for the second and third wind tunnel campaign respectively. This shows that the pre-determined centre of gravity location at the quarter MAC position is too far forward to provide an ideal combination of pitch stability and elevator authority. An overview of the values can be found in table 4.3. In figure 4.10, the visualisation of the MAC location and the neutral point on the Flying V are shown.

Table 4.3: Neutral point and static margin overview

	Neutral point, x_{np} [m]	Static Margin, SM [%]
Second wind tunnel campaign	1.422	22.87
Third wind tunnel campaign	1.402	20.48

For trim, the position of the centre of gravity plays an important role in the sense if it is placed in front or behind the neutral point. For this section the pitching moment is discussed without the influence of the deflection of the control surfaces. This means they rest in zero degrees deflection and the Flying V acts as a wing only aircraft without any other active control surfaces. To trim the aircraft without the interaction of the control surfaces, the centre of gravity can be used as a trimming device. If the centre of gravity is placed in front of the neutral point, the wing will be stable for external aerodynamic disturbances like gusts. If the centre of gravity lies aft of the neutral point, the wing is unstable to any external aerodynamic disturbances in the sense that an increase in angle of attack will result in an even larger growing angle of attack. By placing the centre of gravity on the location of the neutral point, the wing will be neutrally stable and 'trimmed', meaning that an external aerodynamic disturbances will not affect the state of the wing.

By having a mechanism which is able to move the centre of gravity in front and aft of the neutral point, theoretically the wing should be able to fly in a stable manner. By having a fast weight moving mechanism, the wings centre of gravity can be moved towards the front of the neutral point in case of any disturbances. In case of the need to change the angle of attack, the weight can simply be moved in front or aft of the neutral point. In case no external aerodynamic disturbances are acting on the wing, the wing can be trimmed by placing the centre of gravity on the location of the neutral point. For the range between zero and twenty degrees angle of attack, the neutral point location is known and it may therefore be theoretically possible to trim the aircraft without the influence of any control surfaces.

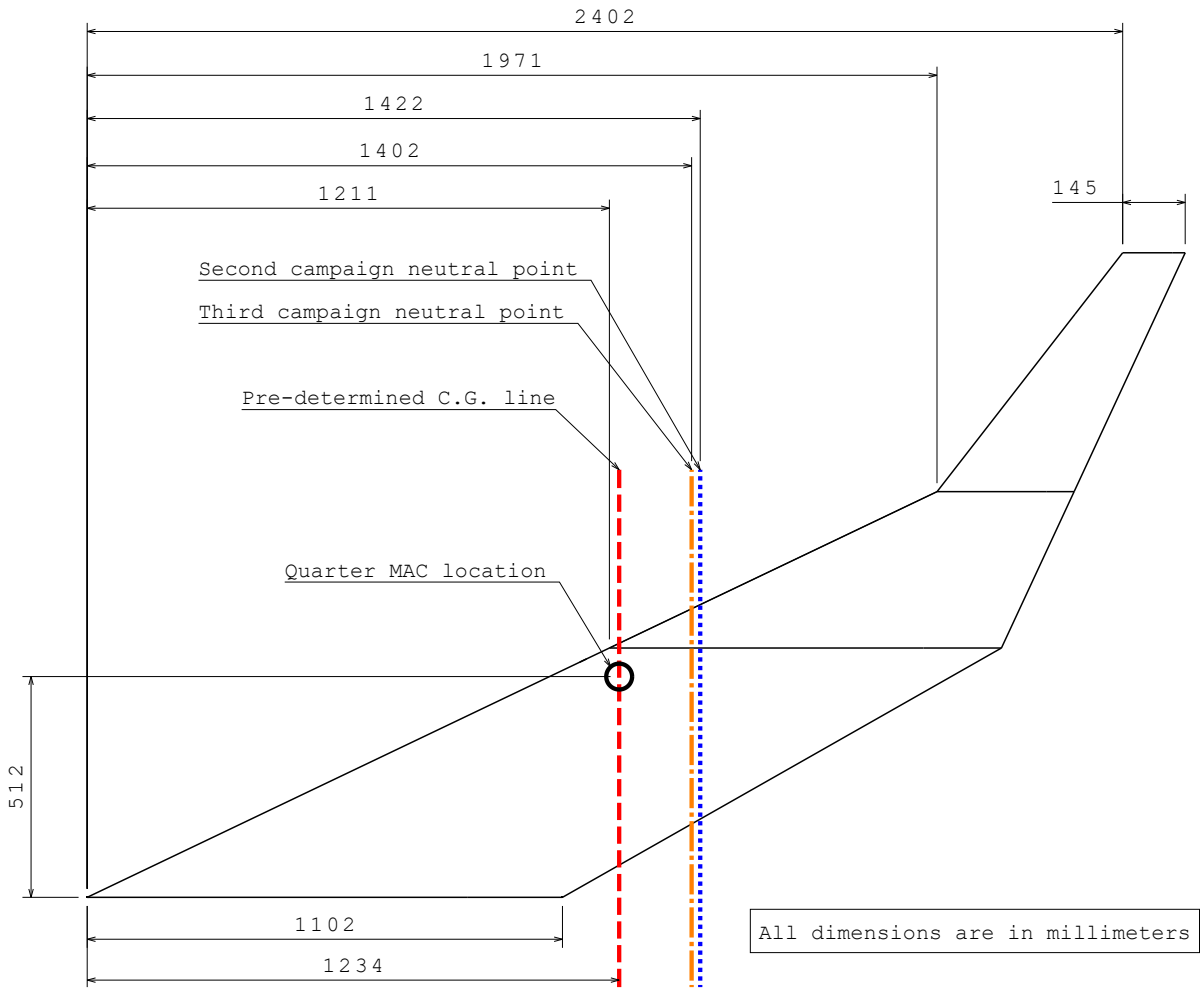


Figure 4.10: MAC and neutral point location visualisation

4.2. Flow Visualisation Interpretation

Flow visualisation is an important measure of determining the state of the flow around the model. In section 4.2.1, the definitions used in the remaining of the chapter are discussed and explained. During the wind tunnel campaigns, three different methods were used. The first method was the oil visualisation, which can be found in section 4.2.2. The second method used was by means of tufts, where both pictures and videos were taken from the model. This can be found in section 4.2.3. The last method used for the visualisation of the air was smoke and can be found in section 4.2.4. The smoke was used to look outside the boundary layer, as the oil flow and tufts only indicate what happens within the boundary layer at the surface of the wing.

4.2.1. List of Definitions

In this section the definitions with respect to the oil flow techniques are discussed and explained. The definitions are terms used for the remaining of the chapter, where the flow will be analysed and discussed. The definitions used for the discussion are as follows:

- **Vortex:** a flow which features a pattern in the shape of spiral. This spiral has a centreline where the vortex rotates about. In the topology layout the vortex can be recognised by a flow moving from an attachment line towards a separation line. The vortex flow usually features a S-shaped pattern on the surface of the wing.
- **Attachment line:** a point or line indicated where the vortex hits and attaches to the surface of the wing. In the topology layouts, the attachment line is indicated by the dotted lines.
- **Separation line:** a point or line indicated where the vortex separates from the surface of the wing. As local flow from the vortex is separated from the surface, it moves into the spiral away from the wing. In the topology layouts, the separation line is indicated by the dash-dotted lines.
- **Primary vortex:** the vortex which is the largest and most dominant indicated.
- **Leading edge separated vortex:** the vortex which originates at the crank of the wing and is formed just in front of the leading edge where the corner of the crank is located.
- **Counter-rotating vortices:** a set of at least two vortices near to each other which counter-rotate around their centreline. As a result, the side where the two vortices meet have the same direction and the same attachment line. Over the surface, the direction of the flow is in an opposite direction. Both vortices feature their own separation line.
- **Cross-flow:** a flow which features a different direction due to pressures and isobars compared to the direction of the undisturbed flow. Angles might be Cross-flow is sometimes also referred to as transverse flow.
- **Isobars:** representation of the pressure distribution of the local airfoils over the complete wing surface.
- **Streakline:** the line which is created by the movement of all fluid particles that have passed continuously through a particular spatial point in the past. The long streaks found by the oil visualisation are for example a measure of streaklines.
- **Pathline:** a trajectory featured by an individual fluid particle.
- **Streamline:** a line which is tangent to the velocity vector of the flow by a mass-less fluid element. In a steady flow, the streaklines, pathlines and streamlines coincide due to a constant velocity-field over time.
- **Pressure gradient:** slope or pressure difference between different pressure regions over the surface of the wing.
- **Boundary layer:** a layer of the fluid which creates a bounding surface between the wing surface and the undisturbed flow. Within the boundary layer viscosity effects are significant.

- **Flow separation:** if the influence of the adverse pressure gradient to the velocity inside of the boundary layer. If the relative boundary layer velocity to that of the surface of the wing is zero, than the flow detaches from the object.
- **Suction peak:** the area on the surface of the wing where the lowest pressure is recorded. Usually this is just aft of the leading edge.
- **Lift recovery:** as the maximum lift is reached, a region beyond this certain angle of attack may cause some stabilising behaviour for the lift. As the wing was originally stalled after the maximum lift angle, the stabilising behaviour is caused by local flow generating very low pressure regions. Usually drag recordings are high due to large areas of flow separations and/or vortices.

4.2.2. Oil Flow

In this section, the results of the oil flow experiments are discussed. The oil flow data is taken from the second and third wind tunnel campaign. For both the campaigns, the model was painted black to provide the sharpest pictures with the lowest surrounding reflections in order to maximise the data quality. The surface roughness between the campaigns was preserved to ensure similar test conditions. The experiments performed during both the campaigns was conducted at a velocity of 18 meters per second at various angles of attack ranging from 5 to 50 degrees. An impression of the pictures taken during the experiment can be found in figure 4.11. This picture was taken at an angle of attack of 22 degrees. To simplify the analysis and clarification of the pictures taken of the oil during the test, topology layouts of the pictures have been made. The results can be found from figure 4.12 through 4.32. Please note that for a more universal approach the orientation of the topology figures are mirrored, so that the air flows from left to right. For the pictures taken during the experiment, the air flows from right to left. The pictures taken during the experiment can be found in Appendix A.

This section is split into different subsections. In section 4.2.2.1, the topology layout for low angles of attack between 5 and 9 degrees are discussed. Section 4.2.2.2 discusses the medium angle of attacks between the 11 and 17 degrees angle of attack. From section 4.2.2.3 onward, the topology layouts for high angle of attacks are presented per one degree instead of per two degrees. This is done for the angles between 19 and 23 degrees angle of attack. In section 4.2.2.4 the very high angles of attack between 25 and 50 degrees angle of attack are presented and discussed.



Figure 4.11: Oil visualisation for 22 degrees angle of attack

4.2.2.1. Topology Layouts for Low Angles of Attack (5 - 9 degrees)

In figure 4.12, the topology overlay of the picture taking during the experiment for 5 degrees angle of attack is shown. The velocity of the air during the experiment was 18 meters per second, which is equal to a Reynolds number at the Mean Aerodynamic Chord (MAC) of 994.000, which is about 1 million. In this figure an overlay for the contours of the wing is made. It is shown by the thick borders what are the edges of the wing as shown in figure 4.11. Furthermore, two horizontal lines defined by a stripe and a dot indicate where the local airfoil is positioned at the kink of the leading edge and the kink of the trailing edge. At the leading edge of the wing, a parallel line defined as a stripe and two dots indicate the location of the zig-zag strip on the suction side of the wing. The thin lines with the arrow show the wall shear stress factor of the flow acting on the surface of the wing. The thick dotted lines indicate regions where a change in direction or a pattern change takes place.

From figure 4.12, it is seen what the flow direction at the surface of the wing is. The flow is completely aligned and shows no sign of separation. It is also seen that the direction of the flow below the leading edge kink is different compared to the region above the kink. The direction of the flow above the kink is almost parallel with the air flow in front of the wing. This is not the case for the flow below the kink. Here, the flow tends to move down due to the alignment of the isobars. The alignment of the isobars represents the pressure distribution of the local airfoils over the complete wing surface. The air flow is subject to the local pressure gradient, meaning it will bend towards the highest suction pressure. This is because of the pressure gradient being the highest in the perpendicular direction of the isobars. After the suction peak, the movement is reversed due to an adverse pressure gradient into the outboard direction [39]. An illustration can be found in figures 4.13a and 4.13b. Therefore, the direction of the flow below the kink can be explained due to the alignment of the isobars having a higher sweep angle compared to the the isobars above the kink. The higher the sweep angle of the isobars, the more dominant the movement of the particles, and thus the flow, is to follow the S-shape. As the sweep angle above the kink is smaller compared to below the kink, the isobars have a lower sweep angle and thus have a lesser S-shape and a more parallel movement to the flow.

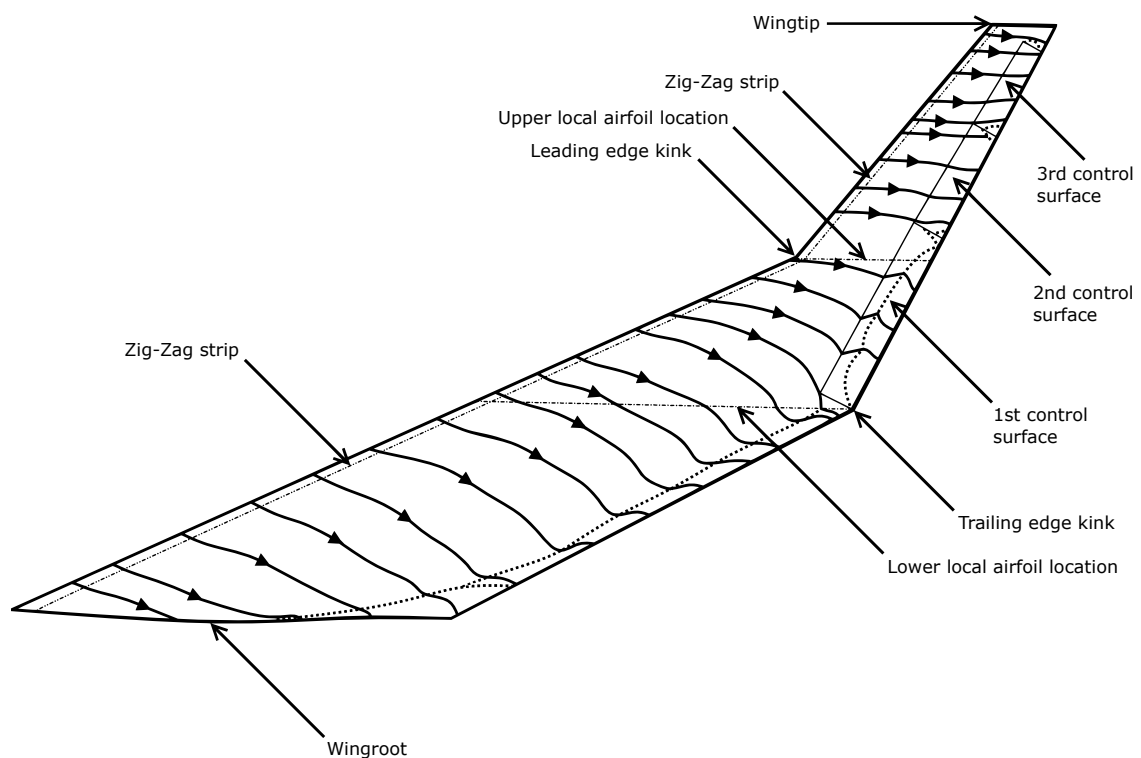


Figure 4.12: Oil visualisation for 5 degrees angle of attack

Looking at the trailing edge of the wing, it is seen that below the kink there is a very thin region of trailing edge separation. Along the chord length the flow follows the S-shape and recovers due to the adverse pressure gradient after the suction peak. The surface flow gets parallel to the undisturbed flow and at the trailing edge itself, the flow drops down with the gravity, indicating minor trailing edge separation occurred.

In the region near the root, there is the phenomena where the boundary layer of the plate grows and impacts the flow on the wing [40, 41]. The boundary layer growth over the length of the plate influences the growth of the boundary layer of the surface of the wing. The splitter plate and the peniche used during the experiment minimised the effect of the boundary layer of the plate on the wing. However, here it can be seen that the effect is not cancelled out and that it leads to a small area of low flow velocities where the oil has a tendency to move down with gravity instead of following the direction of the undisturbed flow.

Looking into the section above the trailing edge kink, it can be seen that the lower control surface has a renewed boundary layer from the slot where the control surface it attached to the wing. An explanation for this is that the gap between the control surface and the wing have an effect on starting a new boundary layer from the slot. Another explanation is that some air is pushed through the slot from the pressure side of the wing to the suction side of the wing, creating a new boundary layer [42]. A last explanation is that there is a slight misalignment between the control surface and the wing, where the control surface is positioned slightly higher compared to the wings surface. This may lead to a renewed boundary layer as well. After the renewal of the boundary layer, the flow at the trailing edge of the control surface stalls off in a way that the local flow velocity in the boundary layer is not high enough to withstand the gravitational forces.

At the upper two control surfaces, the boundary layer at the gap between the control surface and the wing is renewed as well, but no trailing edge separation takes place. The flow direction at the surface of the control surface is completely parallel to the direction of the undisturbed flow. The two gaps between the control surfaces imposes a slot where the air flows through from the pressure side towards the suction side and separates the edges of the control surfaces.

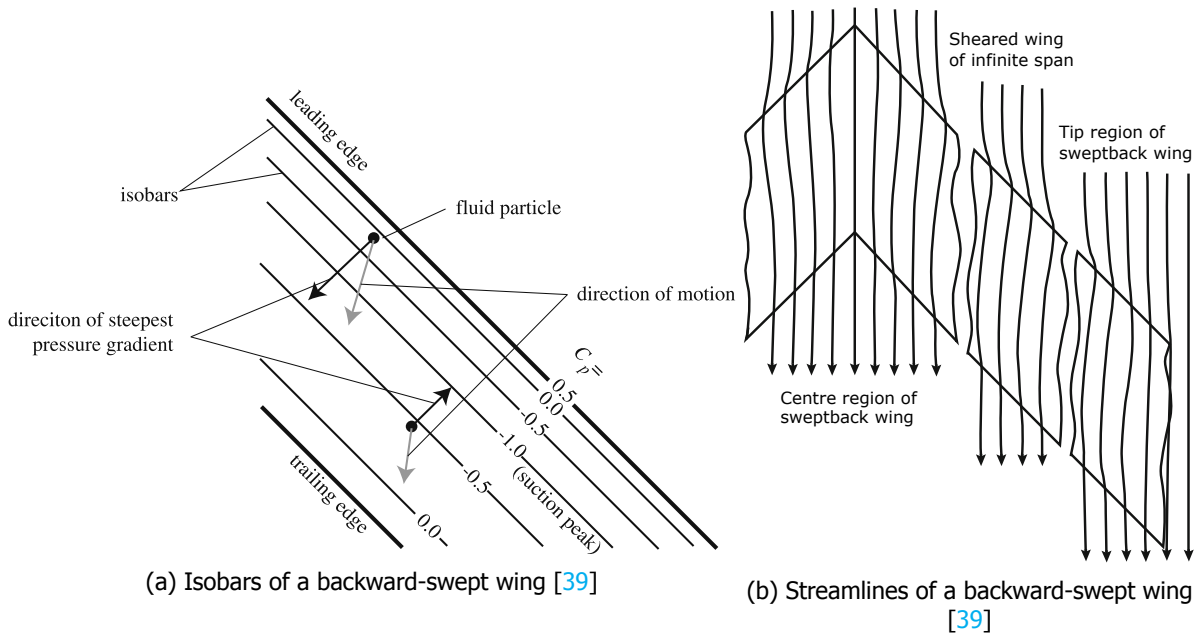


Figure 4.13: Illustration of isobars and streamlines of a backward-swept wing

Continuing to the next angle of attack, the topology layout for the angle of attack of 7 degrees can be found in figure 4.14. In the figure it is shown how the flow transformed from 5 to 7 degrees angles of attack. Differences are seen in the region of the trailing edge below the kink and on the first control surface. The S-curves seen on the wings surface at the angle of attack of 5 degrees are still present at this angle of attack of 7 degrees. Furthermore it is seen that the S-shaped curves in the region between the trailing edge kink and the leading edge kink changed into a flow being more parallel to the undisturbed air flow.

Looking into the region from the root till the trailing edge kink, it is seen that at the trailing edge a new front has formed that changed the direction from the s-shaped flow, at around two thirds of the local wing chord length, into a more parallel flow. Around the kink also the first signs of cross flow is noted. With a cross flow it is meant that the flow is not following the parallel directions of the undisturbed flow, or the the s-shaped curves due to the isobars on the wing. The cross flow for the Flying V is defined as the flow being sucked towards the tip of the wing. This phenomena is caused by local low pressure areas, local tip separation and/or vortex creation. The trailing edge itself of the region between the root and the trailing edge kink still shows a thin region of separation by the fact that the oil runs down with gravity.

The flow on the first control surface is still facing a renewed boundary, but a small region of trailing edge separation as well. The flow on the second control surface had no trailing edge separation at an angle of attack of 5 degrees, but starts to show separation at this angle of attack of 7 degrees. Also the gap between the first and second control surface shows a more dominant region of separation, giving that the airflow is not affected by the region and moves around the small region.

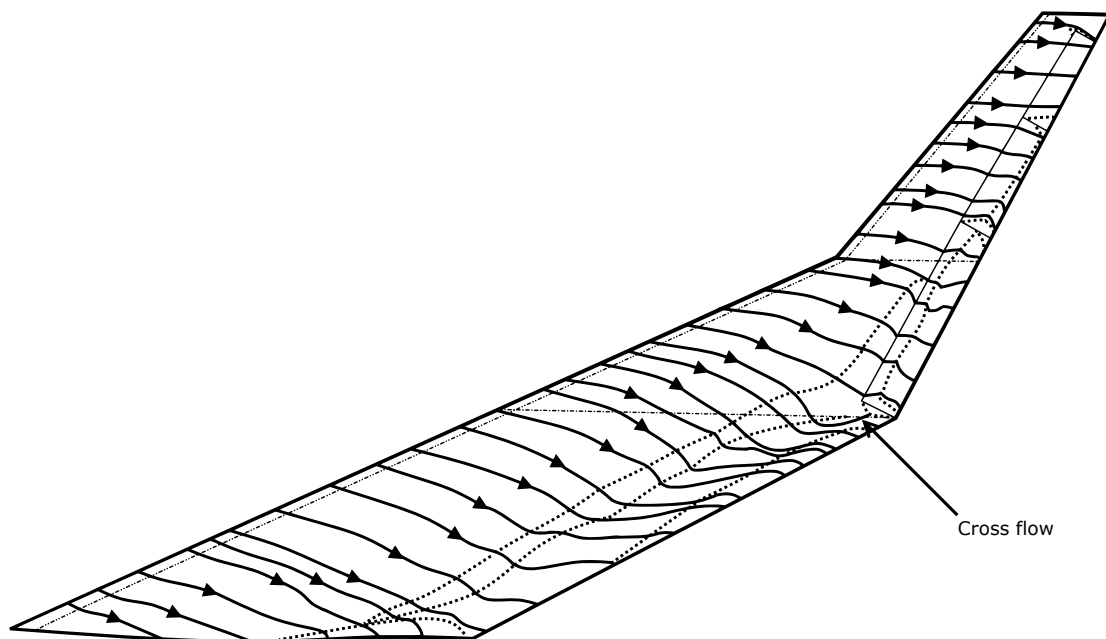


Figure 4.14: Oil visualisation for 7 degrees angle of attack

Moving on to the next angle of attack of 9 degrees, the topology layout can be found in figure 4.15. From the last angle of attack to this angle of attack, the flow has undergone a transformation round the kink of the trailing edge where the airfoil change occurs. It is clearly seen how the flow from the leading edge is turned in a cross flow towards the tip, but halts exactly on the section where the airfoil change occurs. A line of separation is noticed, where the dye of the oil is clustered together on the section where the airfoil is positioned. This is showed by a single black line.

The reason for the separation to occur is the fact that the cross flow is facing a sudden 'downhill' gradient of the surface on the location where the airfoil profile is located. This sudden change in surface direction leads to an adverse pressure gradient, which imposes separation of the air. Above the separation line drawn in solid black, it is seen that the streamline which was above the airfoil location is not affected by the separation occurring. The cross flow streamline tends to move on in the same direction as the separated cross flow streamline did below the line of separation.

What furthermore can be seen is that the flow is from the root to the kink in at the leading edge moves in a direction more along with the undisturbed flow direction. Just after half of the local chord length this pattern changes and after the first dotted line it moves down drastically before it recovers and goes parallel to the undisturbed flow or even slightly transverse towards the tip. At the trailing edge, the flow between the root and the trailing edge kink is still facing minor separation due to the oil moving down with gravity.

At the first control surface, it is seen that the flow is disturbed by the rapid changes in direction of the streamlines. At the lower side of the first control surface, it is seen that the streamline cluster together, while at the top of the control surface there is a small region of separation due to the gap between the first and the second control surface. For the rest of the tip the flow is undisturbed and completely attached to the surface.

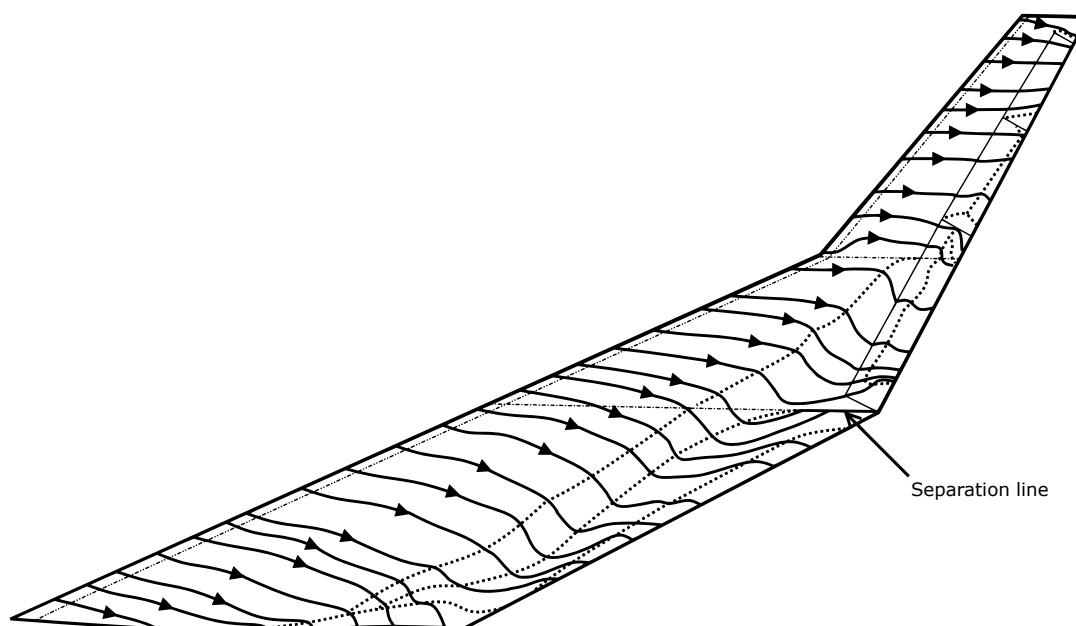


Figure 4.15: Oil visualisation for 9 degrees angle of attack

4.2.2.2. Topology Layouts for Medium Angles of Attack (11 - 17 degrees)

The next angle of attack investigated is the angle of attack of 11 degrees. In figure 4.16 the topology layout of the flow can be found. At the location of the crank, there is a formation of a vortex coming from the kink at the leading edge which spreads in the direction of towards the tip towards the trailing edge of second and third control surface. From this angle of attack onward, the vortex from the leading edge kink will be present at higher angles of attack as well and will change in strength, dimension and direction.

The vortex by means of an ultra violet dye ingested oil can be identified by a separation and an attachment line. The separation line is identified by the roll-up motion of the vortex, which leaves the surface. As a result of this, the direction of the vortex streamline goes into a S-shape and goes moves into a thick line of ultra violet dye. At the other side of the thick line of the ultra violet dye, there is another pattern of streamlines going into the line of separation as well. The attachment line of the vortex is identified as the pattern where a line can be formed that expands the streamlines into two 'departing' directions. One of the vortex rolling onto the surface of the wing in the S-shaped direction and the other of regular aligned flow [43].

The generation of the vortex from the leading edge kink is initiated by the two angles of the leading edges coming together, to create a leading edge separated vortex [44–46]. The leading edge separated vortex increases the local suction pressure and adds to the postponement of separated flow at higher angles of attack. Because of this leading edge separated vortex, the control surfaces are less prone to normal separation and remain effective for higher angles of attack.

Furthermore it is observed that the cross flow below the trailing edge kink gets stronger and a larger region is affected by the cross flow. This can be seen by the fact that the separation line located on the airfoil section got larger towards the leading edge and that the trailing edge separation region reduced towards the root.

From this angle of 11 degrees angle of attack onward, it is observed in figure 4.2 that the lift curve is increasing in lift slope. The vortex acting on the wing does impose an additional lift and is therefore referred to as vortex lift. This effect gets stronger by increasing the angle of attack.

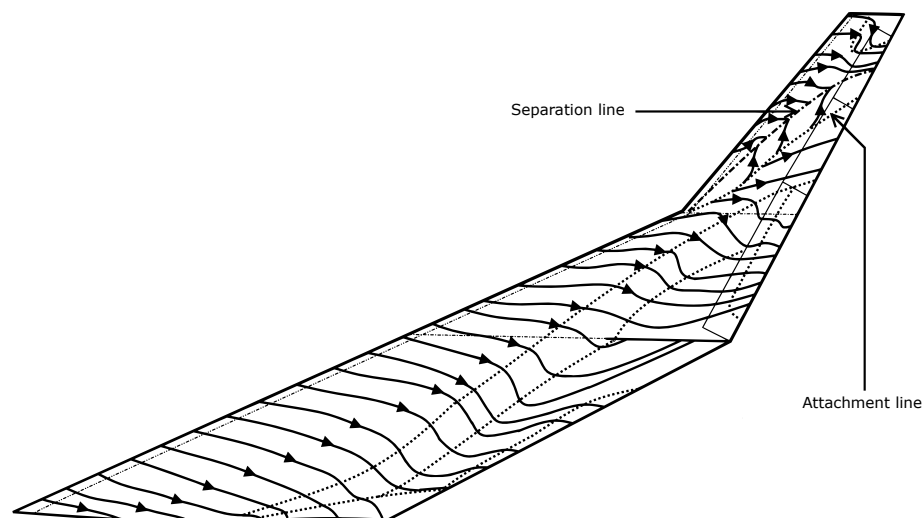


Figure 4.16: Oil visualisation for 11 degrees angle of attack

In figure 4.17, the topology layout of the oil flow picture taken at 13 degrees angle of attack can be found. At this angle, it is observed how another vortex is rolling close and parallel to the trailing edge between the root and the trailing edge kink. This can be seen by the attachment and separation line visible close to the trailing edge. Furthermore, a new vortex is seen between the lower local airfoil location at the trailing edge kink and the new formed separation line.

Two new separation lines are formed at the leading edge near the leading edge kink. The leading edge separated vortex which was first observed at 11 degrees now changed its attachment line location to the new separation line located on the upper local airfoil location. The new lower separation line located near the leading edge kink does not indicate a vortex pattern, but just visualises a single line of separation.

Furthermore, at the third control surface it is seen how a suction region pulls the streamlines onto the surface. No signs of separation are present at this control surface and therefore the control surface is said to be effective. This means that at higher angles of attack the outer control surface, which is used for rolling motions, will be effective and make the airfoil roll. It has to be noted that this is derived from the picture taken where all control surfaces are fixed at their zero deflection angle. It is not investigated by the oil flow till what angle of attack combined with the deflection angle the outer control surface will be effective.

At this angle of 13 degrees angle of attack, it is seen in figure 4.3 that the vortex lift slope gets stronger and adds lift to the linear lift slope. This means that the vortices acting on the suction side of the surface add an additional lift compared to when the vortices were not present.

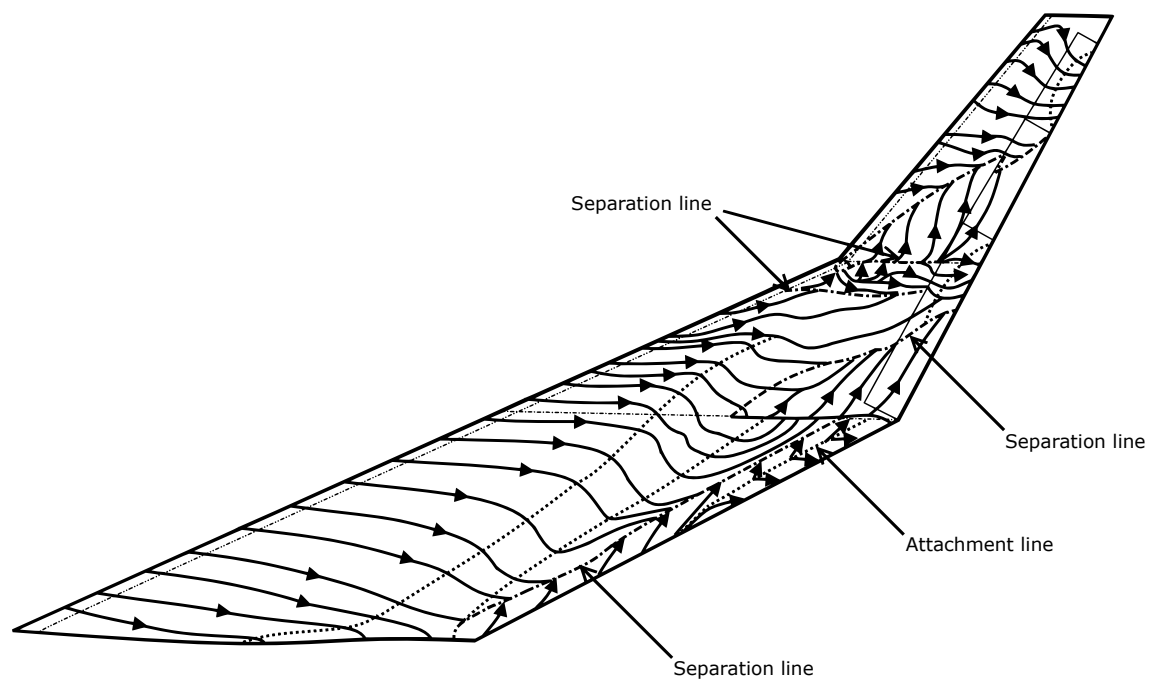


Figure 4.17: Oil visualisation for 13 degrees angle of attack

The next topology layout is based on the oil flow picture taken at the angle of attack of 15 degrees. The topology layout can be found in figure 4.18. In this figure it can be seen that another separation line is formed near the leading edge below the leading edge kink. From this line no streamlines are 'departing' meaning there is cross-flow, but no actual vortex. Below the new formed separation line there are streamlines forming from the separation line, meaning there is a small region where a new vortex is formed.

At the wing tip, it is observed how the attachment line of the leading edge separated vortex has released itself from the corner where the airfoil is located. It now follows the direction of the vortex more and it clearly visualised how streamlines are departing in both directions from the attachment line. Due to this, there is no separation located on the second control surface.

Between the root and the lower airfoil location there is a new formed attachment line which goes towards the lower airfoil location, overshoots it location and returns towards the separation line of the vortex located at the trailing edge. This new formed attachment line indicates a new and larger vortex moving at the region from mid chord of the lower airfoil location towards the entire first control surface. Therefore, at the first control surface, no separation is noticed as well.

Furthermore it is observed at the leading edge between the root and the leading edge kink that the streamlines do not face a downward S-shape any more. The pattern has due to the angle of attack, the blunt nose, the vortices and the cross-flow over the surface changed into a direction which is parallel to the undisturbed flow.

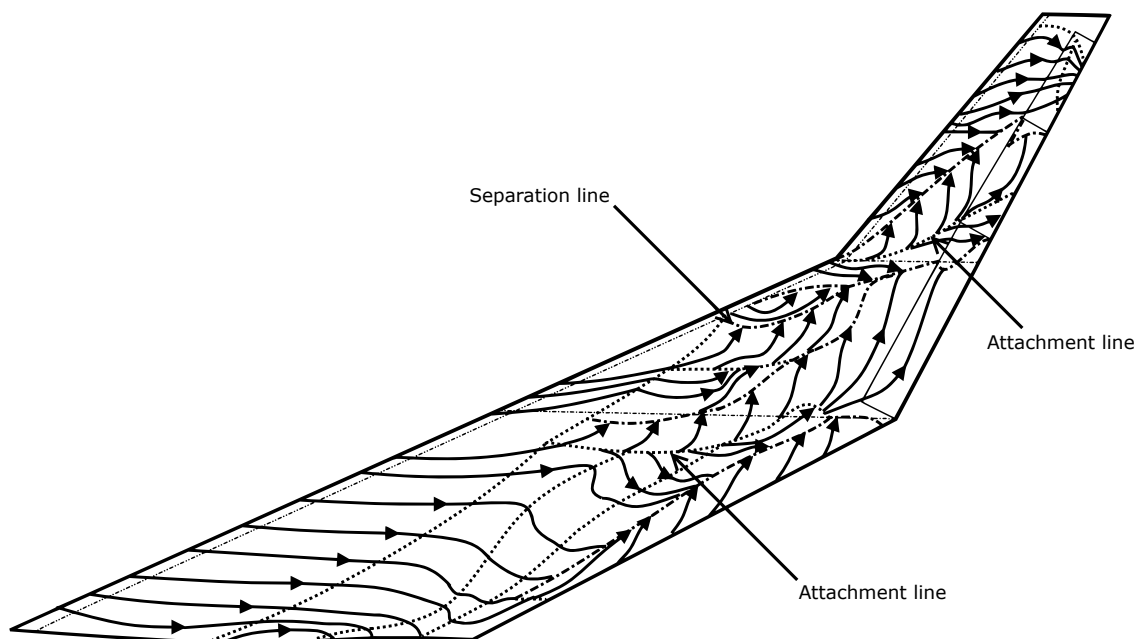


Figure 4.18: Oil visualisation for 15 degrees angle of attack

The next angle of attack investigated is the angle of attack of 17 degrees. The topology layout can be found in figure 4.19. The flow at the suction side of the surface is facing more and more vortex flows as the angle of attack is increased. At this angle of attack, there is a number of 5 different vortices flowing over the surface of the suction side of the wing. Two additional vortex like structures are observed just underneath the leading edge kink, but since their streamlines do not depart from an attachment line, this is not considered as a vortex even though they have a separation line.

Not a lot of change is observed by going from 15 degrees to 17 degrees angle of attack. The main differences are found in the vortices getting stronger. Especially the vortices labelled as the first and the third gained strength by the fact that their surface area got bigger. The separation line of the first vortex moved towards the leading edge, while the same applied for the third vortex.

Two regions of separation get larger as the angle of attack is being increased. The first noticeable region is the wingtip, where separation is noticed due to the ultraviolet dye in the oil moving down due to gravity. The second region of separation is observed at the root, where the region of oil dripping down gets larger towards the trailing edge as well. Beside these two regions, no major separation is noticed over the suction side of the surface.

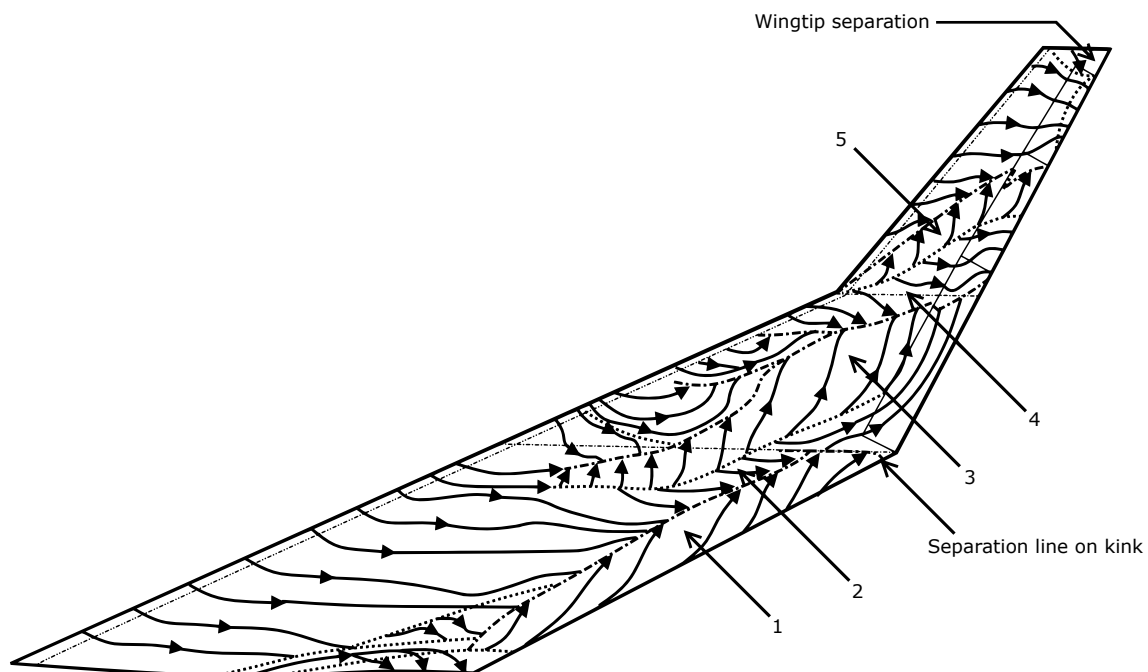


Figure 4.19: Oil visualisation for 17 degrees angle of attack

4.2.2.3. Topology Layouts for High Angles of Attack (19 - 23 degrees)

Increasing the angle of attack leads to the topology layout at 19 degrees found in figure 4.20. At this angle of attack, a total of 7 clear noticeable vortices are found through observing both their attachment and separation lines. The 7 different vortices all have cross flow over the surface rolling towards the tip and increasing additional vortex lift to the linear lift of the wing.

The main difference compared to the last angle of attack which was at 17 degrees, is that the separation line of the first vortex defined in figure 4.19 let go of the local airfoil location and moved in the transverse direction with the vortex itself. Due to the movement of the separation line, this vortex has now become the strongest vortex and impacts the lift coefficient the most.

Furthermore, three new attachment lines have formed to create their own vortex. The two regions near the leading edge where at the last angle of attack only cross flow was observed now turned into small vortices as well. The lower new attachment line turned into a closed attachment line at the bottom, closing the path toward the separation line of the first vortex. This attachment line was already visible at the last angle of attack as well and created its own vortex, but it moved a lot and closed the inlet path compared to this angle of attack.

From this angle onward, the angle of attack is increased by one degree instead of two degrees in order to clearly show the development of the flow over the surface around the region where the vortex lift turns into a decrease in lift slope. The development of the flow will tell how the vortices develop and influence the lift characteristics of the wing.

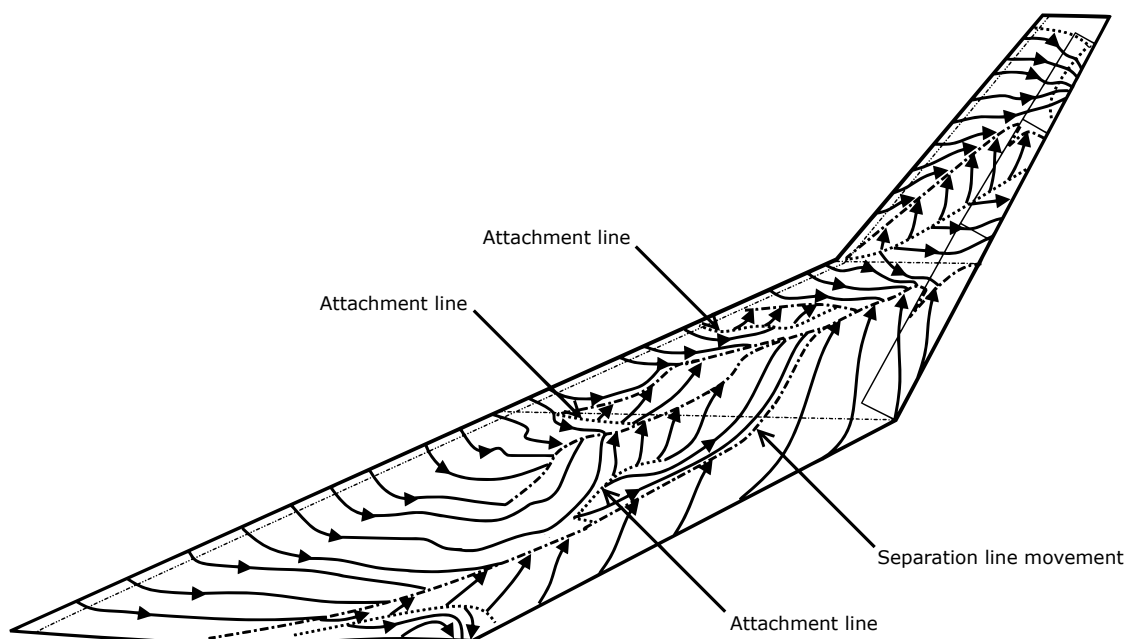


Figure 4.20: Oil visualisation for 19 degrees angle of attack

The next angle of attack investigated is at 20 degrees. The topology layout can be found in figure 4.21, where it is seen that the primary vortex is now added with an attachment line. This attachment line comes from the boundary where the initial root separation originated from. The closed region of root separation turned into a region of root separation and trailing edge separation. Because of this small loss in vortex surface area, it is also observed in figure 4.3 that the lift slope is now at its original value of around 0.03. Looking into the figure, it is observed that this increase of lift slope is turned into a lower lift increase than at the original linear slope below the 10 degrees angle of attack.

Furthermore, the two vortices at the leading edge of the wing below the leading edge kink turned into cross flow, as the streamlines do not originate from an attachment or separation line any more. The attachment line discussed at the last angle of attack which closed the patch by growing towards the separation line of the main vortex now is released from the separation line again. This as a result shows a very long streamline travelling from the leading edge parallel to the undisturbed flow into a cross flow until it reaches a separation line.

At this angle of attack, it is seen in figure 4.6 and 4.8 that the sign of the stability derivative switches from positive to negative and that the trend of the moment coefficient is therefore changed from a negative slope into a positive slope. It is also seen in figure 4.11 that the neutral point of the wing changes location and lies in front of the centre of gravity, which explains what is happening with the moment coefficient and the stability derivative. The centre of pressure seen in figure 4.7 confirms the behaviour of the neutral point and indicates that the centre of pressure location is at its furthest aft position and will move towards the nose. Looking into the topology layout of this angle of attack, it is seen that separation occurs at the trailing edge near the root and at the wingtip, but no further separation is observed indicating that the centre of pressure indeed will move forward. Another explanation for this is that the strength of the vortices flowing over the surface of the wing are changing in strength and they will therefore give another pressure distribution over the wing.

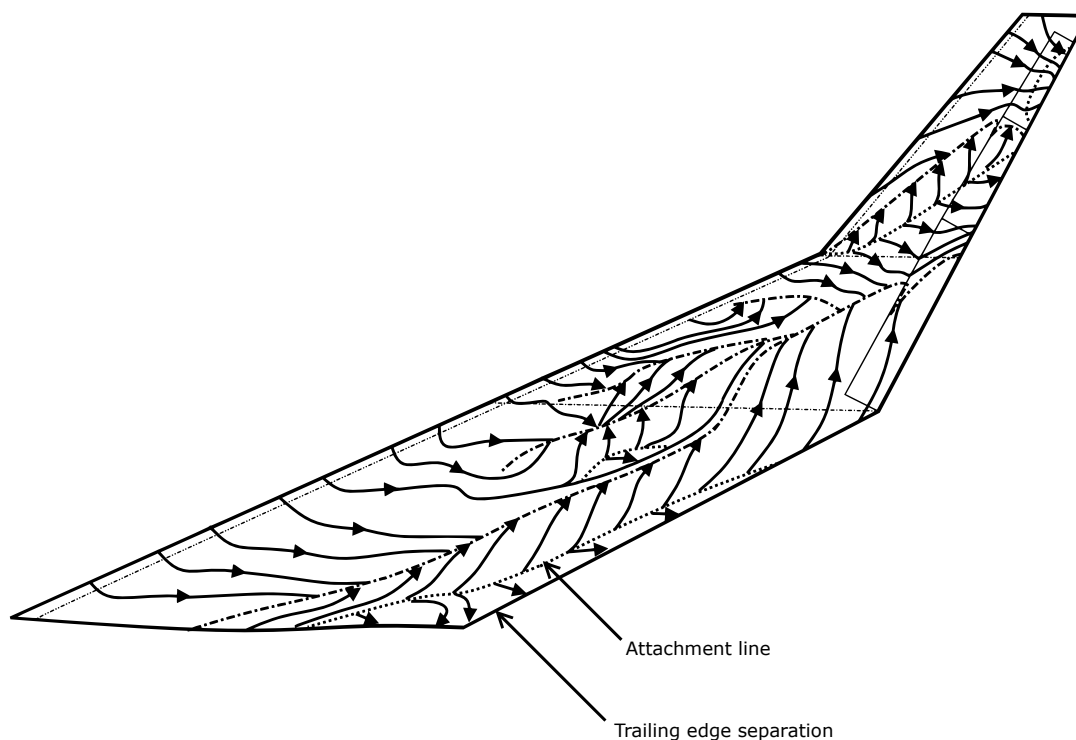


Figure 4.21: Oil visualisation for 20 degrees angle of attack

Increasing the angle of attack by one degree leads to the topology layout at 21 degrees angle of attack, as found in figure 4.22. At this angle of attack it is observed how the separation line of the primary vortex switches from position. At the last angle of attack, the separation line was connected to a lower separation line than at this angle of attack. By increasing the angle with one degree, the separation line of the primary vortex switched towards the separation line closer to the leading edge. This results in an even larger area of the primary vortex.

The separation line where the primary separation line was first attached to still is still visible on the surface by the oil. The separation line sits in the middle of the primary vortex and splits the primary vortex into two segments. The bigger segment flow around the separation line along the trailing edge toward the direction of the wingtip, while the segment closer to the leading edge is interrupted by the old separation line. The old separation line creates a small attachment line, which creates one small vortex flowing the leading edge until it reaches the new separation line of the primary vortex. The other side of the attachment line creates streamline which do not specifically generate a new vortex, but more like a cross flow, which is interrupted as they cross the new separation line of the primary vortex as well.

The region near the root and the trailing edge where a small segment of trailing edge stall was observed at the last angle of attack has grown a bit and therefore adds to the loss of lift and the increase of lift. Besides this area and the wingtip which shows small signs of separation, there is no major area where separation of the air occurs. Because the wingtip shows more signs of separation, this may add to the argument of separation mentioned at the last angle of attack for the movement of the centre of gravity towards the nose. Loss of suction force at the tip will namely lead to another pressure distribution and will make the centre of pressure move towards the nose.

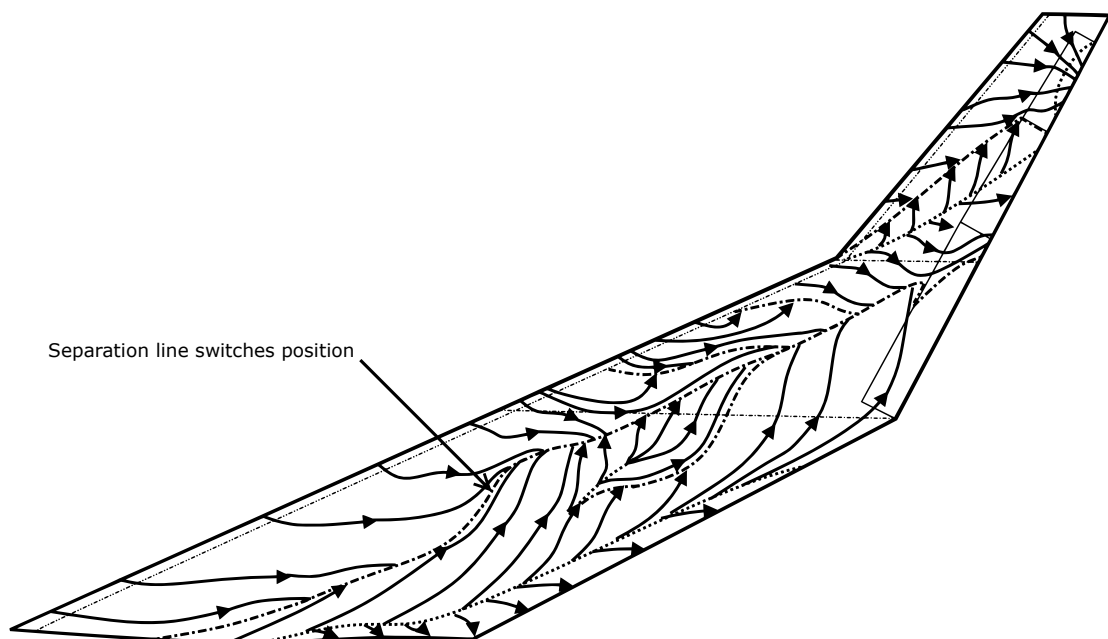


Figure 4.22: Oil visualisation for 21 degrees angle of attack

At this angle of attack of 22 degrees it is seen in figure 4.23 that the separation line which split the primary vortex at the last angle of attack has vanished. The primary vortex now sustains the entire area without being affected by any attachment or separation line inside the vortex at the surface of the wing. The primary vortex has now completely grown to its final shape and continues to develop over the coming angles as the angles of attack are being increased.

Looking into what the primary vortex effects, it is seen that the vortex originates from the root, gets wider towards the wing tip as it progresses parallel to the leading edge and flows off the surface of the wing as it completely went over the first control surface area. The area the primary vortex covers is large in the sense that the surface of the wing faces almost a complete cross flow instead of a S-shaped or straight flow. This is different compared to what a swept wing of a conventional aircraft usually faces [47, 48]. Here the regions of cross-flow are mainly in the regions near the tip, at the location where separation occurs as well. By looking into highly swept blunt leading edges, it is observed that leading edge vortices will dominate through a large range of angles of attack [10].

The leading edge separated vortex has developed over the range of angles of attack starting from 11 degrees toward this angle by the movement of the attachment and separation line. The separation line has developed by moving higher towards the wing tip. First, the separation line of the leading edge separated vortex was in the direction where the attachment line is right now, ending half over the second surface. Over the angles of attack between 11 and 22 degrees, the separation line has moved towards the wingtip, where the separation line exactly lies onto the gap between the second and third control surface. The attachment line has developed by first being unstable and switching from the upper airfoil location towards the wing tip where it reaches the half wing span of the second control surface. Because of this, the vortices created at both sides of the attachment line result in that separation of the airflow is delayed to higher angles of attack and that therefore the second control surface remains effective for a larger range of angles. Again, this is not visualised by the oil by deflecting the control surfaces, but this is confirmed by the trim data in section 5.2.

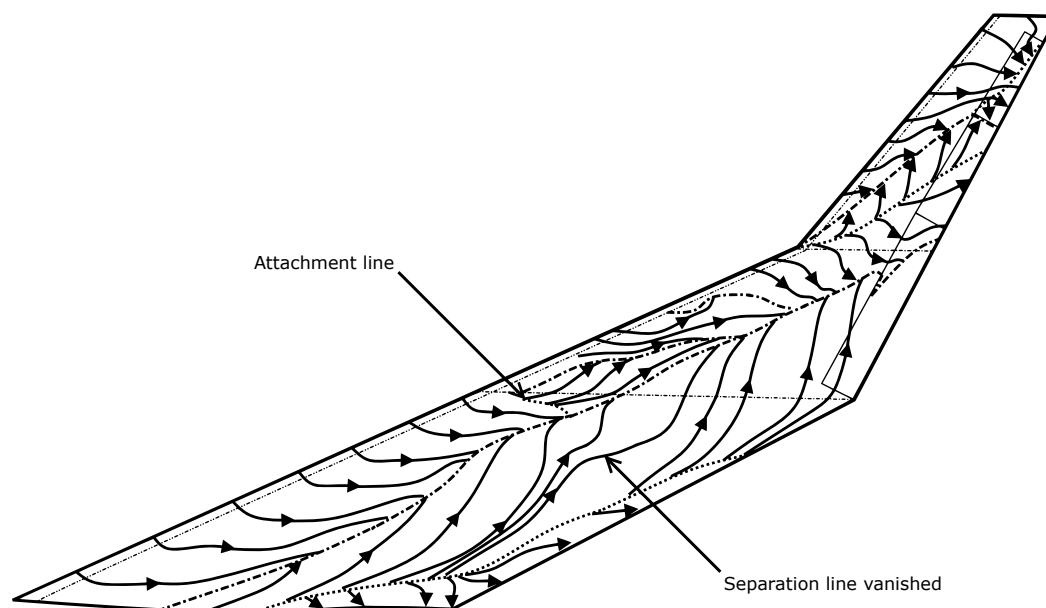


Figure 4.23: Oil visualisation for 22 degrees angle of attack

The topology layout for the angle of attack of 23 degrees can be found in figure 4.24. Differences with respect to the last angle of attack are that the separation line which was present at the leading edge between the root and the leading edge kink has vanished. The turns the region into a cross flow, with characteristics of a vortex. This is due to the fact that the flow originates from an attachment line and ends in a separation line, seen by the streamlines.

Furthermore, the primary vortex has moved a little towards the leading edge and decreased in size. This is probably due to the high angle of attack and the fact that at the trailing edge of the root the region of separation is growing with each increment in angle of attack. The height of the primary vortex now till three quarters of the first control surface. The separation line of the leading edge separated vortex is not located at the gap between the second and third control surface any more. The separation line moved towards the wingtip, which results in the leading edge separated vortex to have an effect on the third control surface as well. Besides the separation at the root and the separation at the wingtip, there is no sign of a separation region observed.

As seen in figure 4.2 and 4.3, the lift slope is not as high any more as it was at its peak at was between the 10 and 20 degrees angle of attack. Also, the lift coefficient is increasing with a slower rate due to the lower lift slope, which is an indication that lift loss is occurring on the surface. Looking into the topology layout, the vortices are still acting onto the surface of the wing, but the loss in lift is explained by the growing separation at the root, the trailing edge and the wingtip.

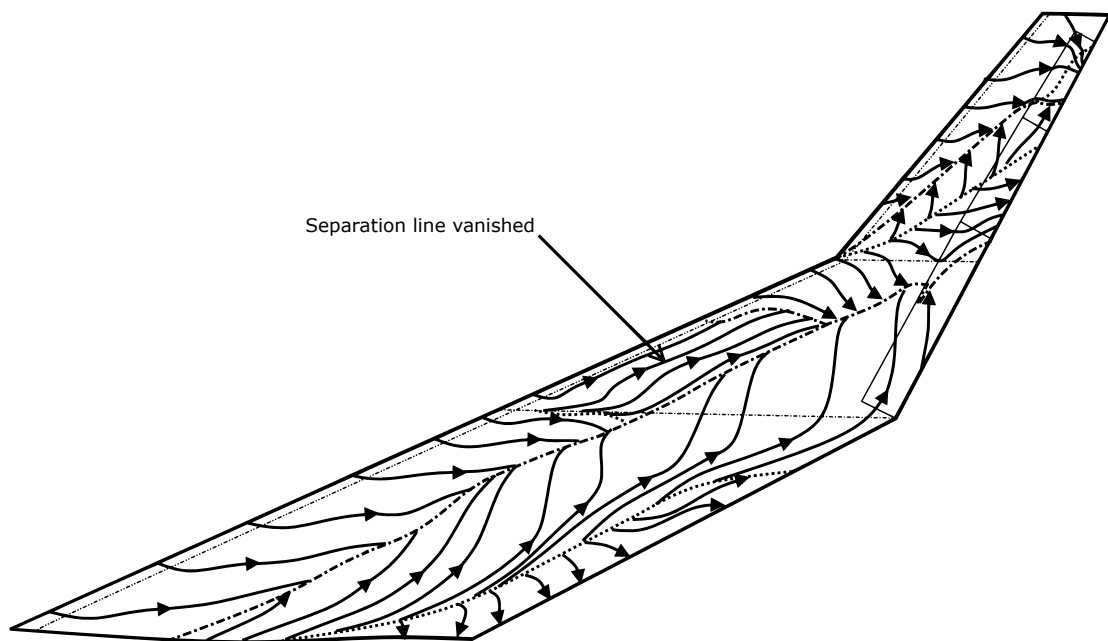


Figure 4.24: Oil visualisation for 23 degrees angle of attack

4.2.2.4. Topology Layouts for Very High Angles of Attack (25 - 50 degrees)

The next angle of attack investigated is at 25 degrees, as can be found in figure 4.25. From now on, the angle of attack will be increased with an increment of two degrees per time, until the angle of attack of 35 degrees is reached. It is seen that the attachment line at the leading edge between the root and the leading edge kink has moved and lies onto the lower airfoil location. This means that the sudden change in surface angle causes the flow not to separate, but to initiate a new starting point of the flow. The flow from the attachment line lying on the lower airfoil location moves towards separation line of the primary vortex, as well as the separation line which is towards the wingtip. The flow coming over the leading edge flows towards the separation line in the direction of the wingtip. This means that the flow is surrounded by two different separation lines.

At the first control surface, it is seen that a new separation line has formed, originating at the gap between the control surface and the main wings surface, flowing towards the second control surface where it merges with the separation line of the primary vortex. The air flowing through the pressure side of the gap towards the suction side of the surface leads to interactions with the primary vortex, which creates this separation line. The flow itself does not show a region of separation, but instead the separation line of a part of the primary vortex which rolls over the first control surface.

At the root, it is also observed that a new attachment line has formed, which was not present at the last angle of attack. The new formed attachment line shows a small region of separation at the left, while at the right there still is a region of attached flow. This region is the beginning of the real separation of the root section, which start at the trailing edge of the root. The separation is as earlier explained due to the boundary layer interaction with the splitter plate and the wing.

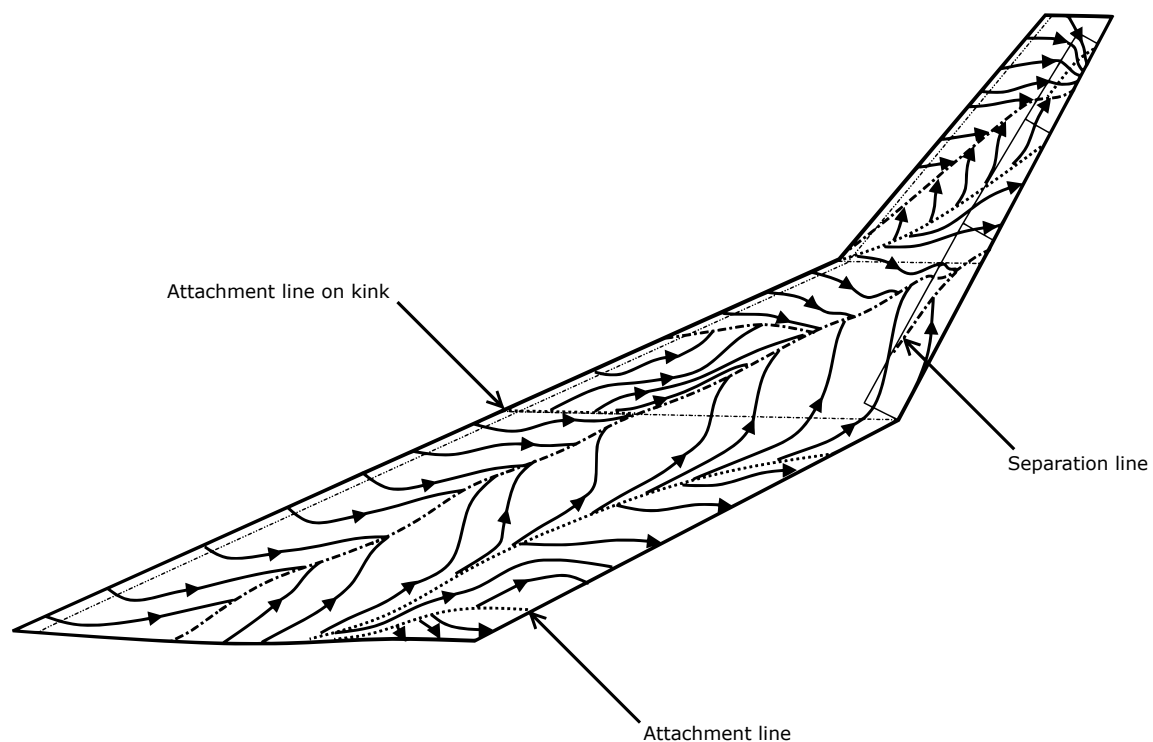


Figure 4.25: Oil visualisation for 25 degrees angle of attack

In figure 4.26, the topology layout for the angle of attack of 27 degrees can be found. In this layout, it is seen how the flow developed from 25 to 27 degrees angle of attack. The main differences are found in the reduction of the area covered by the primary vortex, the growth of root separation and the movement the attachment line near the leading edge which was on the lower airfoil location towards the root.

The movement of the attachment line to the position below the lower airfoil location is a first sign of the flow over the leading edge of the wing being distributed by the increasing angle of attack. The flow starts the attachment line at a lower location as the radius over the leading edge is larger compared towards the wingtip. Above the attachment line, it is therefore seen that the streamline only comes from the attachment itself and are not entering from the leading edge any more. A cross flow prevents the air from coming over the leading edge and flow over the suction side of the surface.

The attachment line of the leading edge separated vortex moved down towards the first control surface. Furthermore the separation line of the leading edge separated vortex moves up toward the wing tip. By this, the origin of the vortex is not from the point in the leading edge corner any more. Instead, the front side of the vortex now covers a wider region. The area the vortex covers also has grown bigger, indicating the vortex has grown stronger as the angle of attack was increased to 27 degrees.

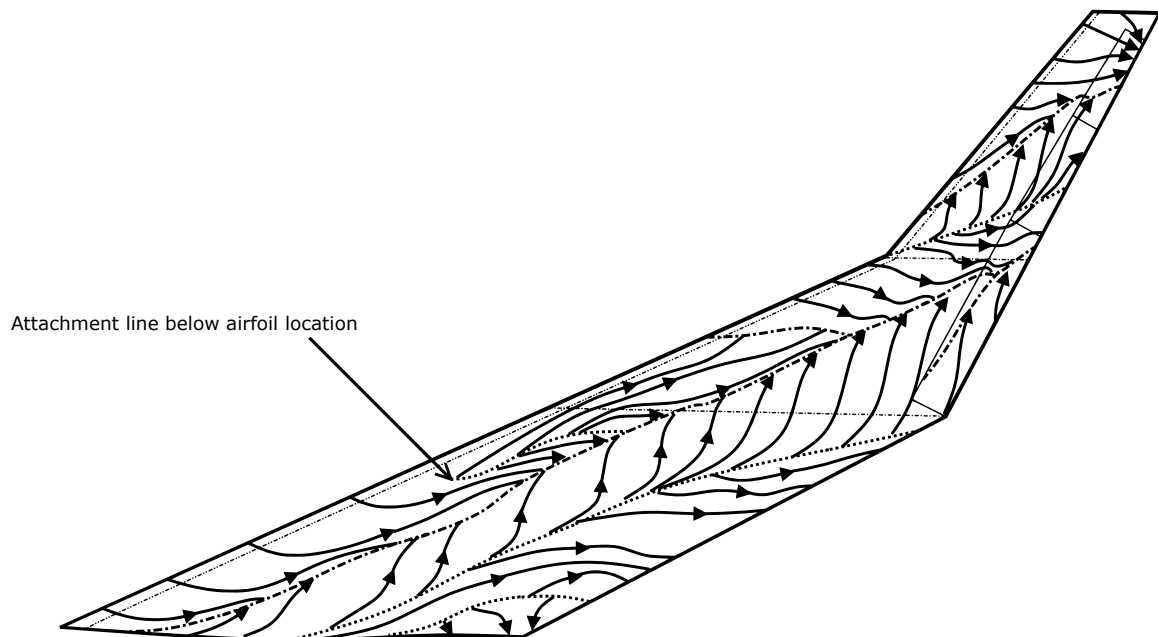


Figure 4.26: Oil visualisation for 27 degrees angle of attack

At the angle of attack of 29 degrees multiple changes have occurred, as can be seen in the topology layout found in figure 4.27. Starting at the first control surface, it can be seen that the separation line has vanished. Because this occurred, the primary vortex which was split due to the separation line at 25 and 27 degrees angle of attack now recovered into a single vortex. Furthermore, the attachment line at the root has vanished. This leads to the fact that the region of separation is not directly coming from the attachment line any more, but originates from the root section as can be seen from the streamlines. Also, in this region trailing edge separation occurs, leading to loss of lift and increase in drag. The movement of the attachment line of the primary vortex towards the leading edge of the wing decreased the size of the primary vortex. In figure 4.3 it can also be seen that around the angle of attack 30 degrees lots of small changes in the lift slope are seen. This behaviour is explained by the movement of the attachment and separation lines, as well as the changes in strength of the vortices and the growth of separation over the wing.

Looking into the leading edge of the wing, one new separation line and two attachment lines are observed. The separation line exactly overlaps the attachment line which was observed at 27 degrees angle of attack, meaning the attachment line has become an elongated separation line. Close to the separation line of the primary vortex, a new attachment line has appeared, giving the presence of another small vortex in front of the primary vortex. This vortex is placed towards the leading edge and is surrounded by the new separation line and the separation line of the primary vortex.

Above the separation line of the new vortex, another new attachment line is formed, giving presence to another vortex rolling into the opposite direction as the one below closer to the root. Also seen from this attachment line is that the streamlines are moving over the leading edge of the wing towards the pressure side of the wing. This can be explained by the fact that the location of the air to hit the static point has shifted towards the pressure side by increasing the angle of attack. As a result, the airflow from the attachment line moves in a S-shape towards the leading edge and rolls into a counteracting vortex off the surface.

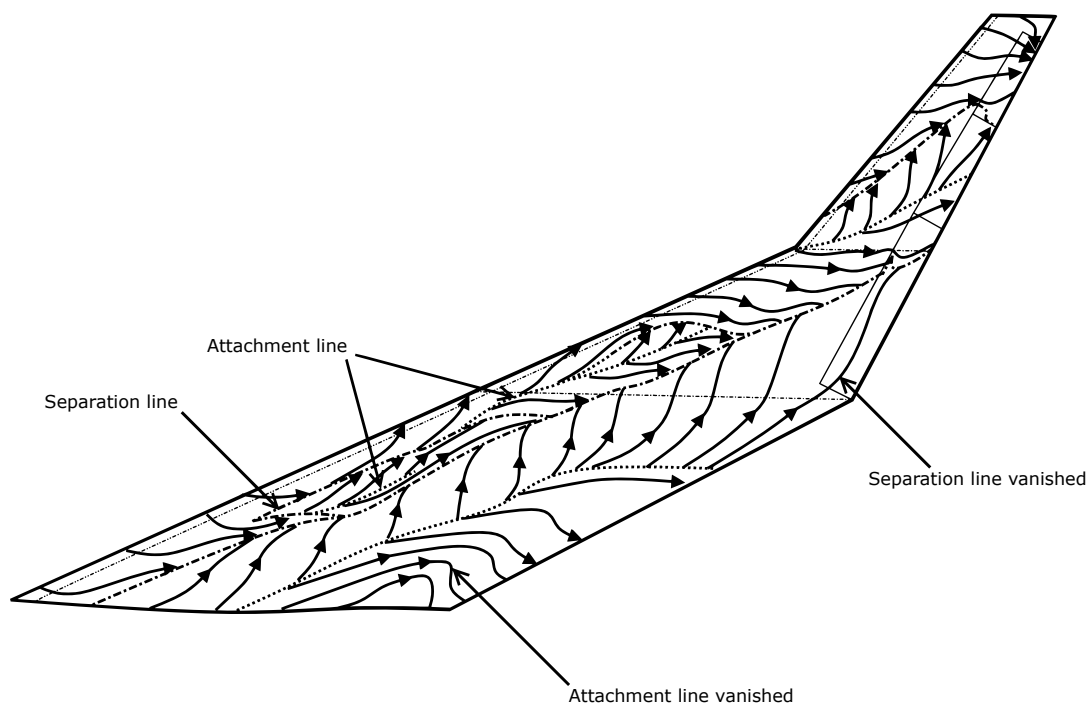


Figure 4.27: Oil visualisation for 29 degrees angle of attack

The topology layout for the angle of attack of 31 degrees can be found in figure 4.28. As was discussed at the previous angle of attack at 29 degrees, the separation line near the leading edge became an attachment line. At this angle of attack, the newly formed separation line switched back to an attachment line. The separation line gave rise to a small vortex regime at the previous angle of attack, but the new attachment line at the current angle of attack creates a small vortex regime into the other direction towards the separation line of the primary vortex. Furthermore, the bottom side of the attachment line was closed by a separation at the previous angle of attack. At the current angle of attack this gap is open, but it does not necessarily lead to inflow, as the flow in the channel originates from the attachment line. Due to the high angle of attack and the attachment line near the leading edge of the wing, the pattern of the flow going over the nose in the rolling vortex motion is maintained and grown into a slightly larger area.

Furthermore at the leading edge kink, it is seen that the attachment line moved towards the root and lies onto the upper airfoil location. The difference in surface inclination leads to the movement of the attachment line to the point where both surfaces meet at the kink. Due to this, the lead edge separated vortex increased in area and now covers half the wing tip. This includes part of the first and third control surface, including the full second control surface. The separation line of the leading edge separated vortex halts at the gap between the third control surface and the wing, where the renewal of the boundary layer causes the separation line to disappear.

Near the trailing edge kink, two differences have been observed compared to the last angle of attack. The first difference is that the separation line on the first control surface reappeared and is causing a line of where the vortex comes lose from the surface. Again, this separation line causes the primary vortex to break into two different vortices. The second difference observed is that the attachment line below the trailing edge kink is not connected to the trailing edge anymore. Because of this, the flow below the attachment line is now able to flow away over the surface into the primary vortex. Also, the attachment line has moved up, meaning that the area of the primary vortex is reduced, which causes a loss of lift. The region of separation near the root and the trailing edge is increased as well. It is also seen that at the root, a big region of separation is causing the oil to move down with gravity, meaning no actual flow is occurring at this section on the surface on the wing.

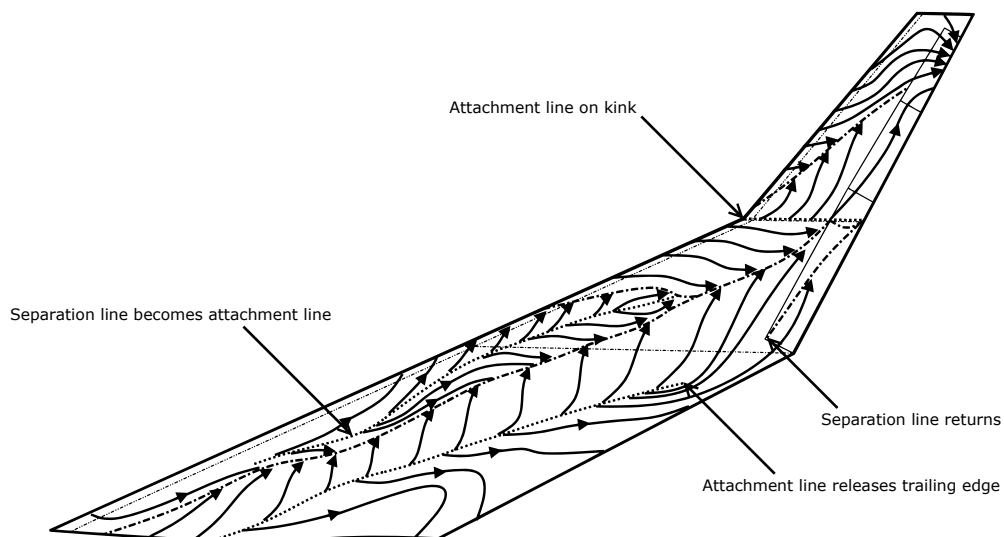


Figure 4.28: Oil visualisation for 31 degrees angle of attack

Looking into the next angle of attack of 33 degrees, it is seen the flow developed in several places. The topology layout for this angle of attack can be found in figure 4.29. At the leading edge of the wing, it is seen that the attachment line which was created at the previous angle of attack has broken down and turned into a separation line. The old attachment line is still visible and can be found at the leading edge further towards the wing tip. The attachment line still creates a vortex towards the separation line of the primary vortex, but the vortex into the direction of the leading edge is not further occurring.

At the leading edge kink, it is seen how a new separation line has developed. This separation line causes the leading edge separated vortex to break down into two smaller counter-rotating vortices. One of them is still defined as leading edge separated, while the other one is a normal and smaller vortex. The attachment line which moved down towards the upper airfoil location is remains at its place. The separation line of the leading edge separated vortex moved down a little and now halts at the gap between the second and third control surface.

At the first control surface it is seen how a new attachment line formed at the leading edge of the control surface. This is caused by flow moving from the pressure side towards the suction side through the gap between the wing and the control surface. This flow causes the boundary layer to be renewed, which in turn forms a new attachment line. The flow from the attachment line is in a S-shape, which indicates that the flow behaves a cross-flow. Because no separation line is observed, it is uncertain whether this is a vortex or not. Because no separation itself is seen, the first control surface does not show trailing edge separation.

At the root and the trailing edge, a new attachment line has been created. This new attachment line in combination with the old attachment line which shrunk creates a gap where the air flows through into the region of the primary vortex. Most of the surface airflow bound by the two attachment lines show separation, meaning loss of lift and increase in drag will be more severe.

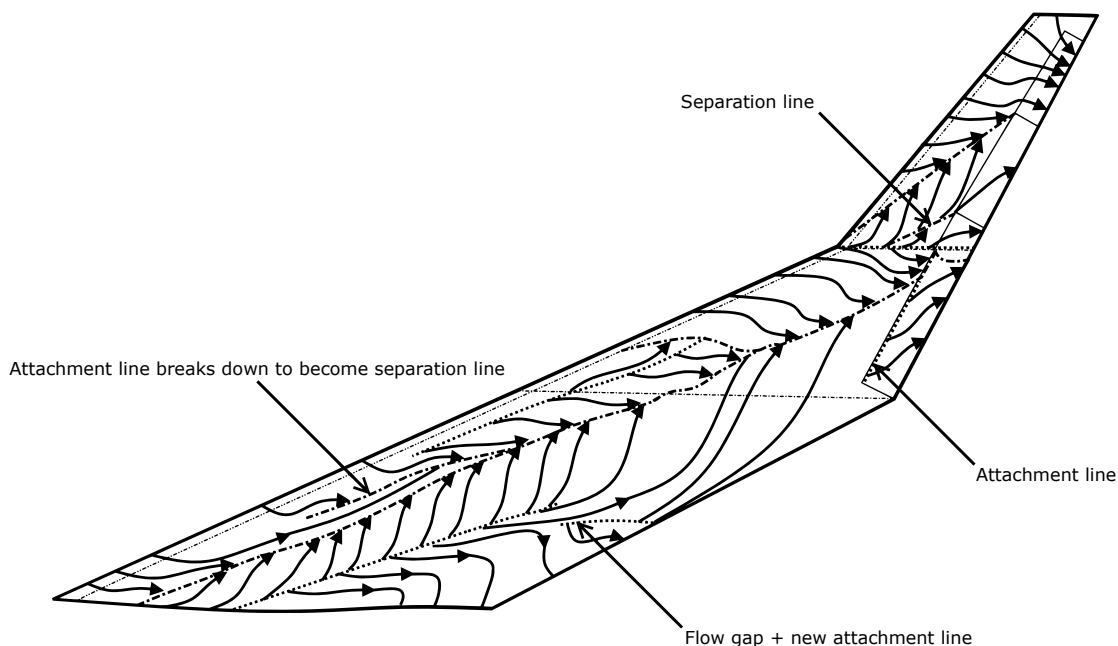


Figure 4.29: Oil visualisation for 33 degrees angle of attack

The picture taken at an angle of attack of 35 degrees is the last picture taken in the detailed range of angles of attack which is investigated. As the aircraft during flight will not fly at these high angles of attack due to stability reasons as explained in section 4.1.2, only the moment of maximum lift and lift recovery are recorded during the experiment. These results can be found in the next two figures. The results for the angle of attack of 35 degrees can be found in figure 4.30.

Looking at the leading edge of the wing, two differences are observed. The first observation is that the attachment and separation line merged together. This means that the attachment line transformed into a separation line as the flow went from the root towards the tip. Furthermore, the separation line seen at the previous angle of attack vanished and leaves the attachment line at the leading edge for the creation of the vortices towards the separation line of the primary vortex and the vortex towards the leading edge of the wing. It is also seen how the vortex which rolls over the leading edge of the wing does not return, as the flow more towards the kink has a counter-rotating S-shape, indicating the vortex does not have an influence on that particular region on the surface.

At the second control surface, it is seen how the air from the pressure side is pushed towards the suction side of the wing through the gap between the control surface and the wing. This renews the boundary layer of the flow, which in turn creates a new attachment line on the leading edge of the second control surface. The flow from the attachment line is in a S-shape and does not show any signs of trailing edge separation. The leading edge separated vortex is stopped by the new attachment line and does not have an influence on the surfaces of the control surfaces any more.

The region at the root and the trailing shows more signs of severe separation, as the oil moves down with gravity. At the trailing edge, it is seen how trailing edge separation is acting taking place at the separated region. The wingtip shows a separated region as well, which in turn influences the effectiveness of the third control surface.

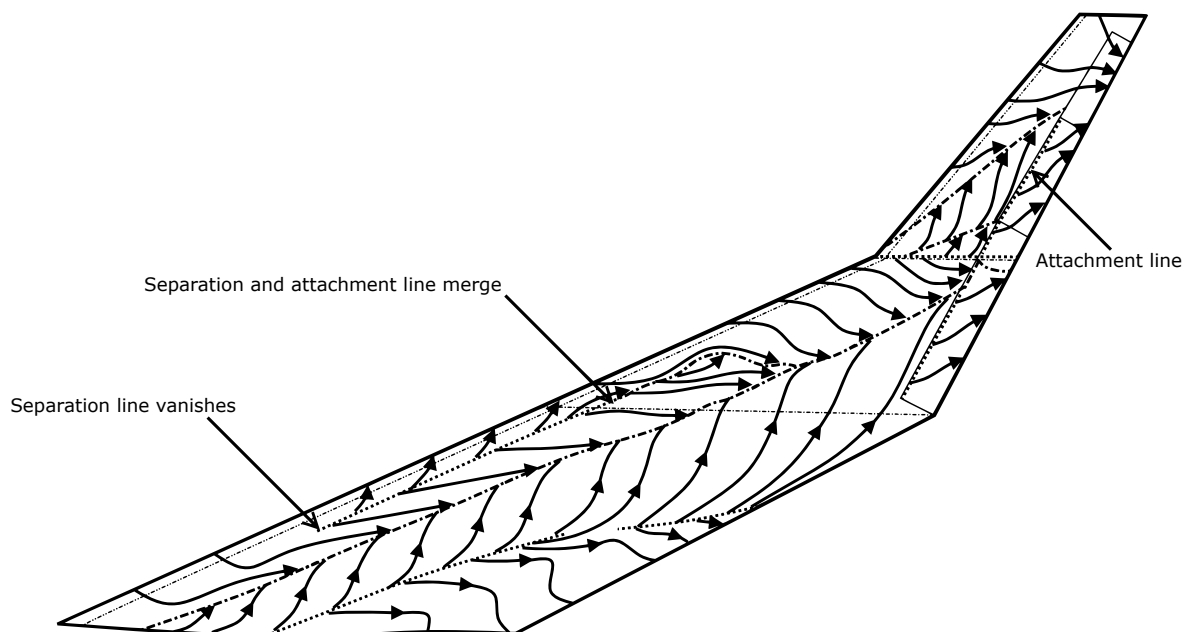


Figure 4.30: Oil visualisation for 35 degrees angle of attack

At the angle of attack of around 41 degrees, it is shown by the lift results in figure 4.2 that the maximum lift coefficient is reached. Therefore this angle of attack is also investigated by the oil, where the results can be found in figure 4.31. At this angle of attack the lift slope is zero, which means that the change of the flow around this point does not lead to a lift increase, but instead to a lift decrease. As seen in the figure, regions of both separation, vortices and cross-flow combine to a situation where the maximum lift of the wing is achieved.

At the leading edge of the wing, the attachment and separation line have vanished, meaning the vortices which were present at previous angles of attack are not longer influencing the flow at the surface of the wing. Instead, normal aligned flow combined with regions of small separation are now observed from the leading edge. The primary vortex which was over most of the surface area of the wing at previous angles of attack has shrunk by size. This is due to the separation line of the primary vortex being moved down and the region of trailing edge separation on the control surfaces which impact the primary vortex. At the root of the wing, the region of separation has shrunk a little as well and now adds to the flow into the primary vortex, creating additional lift instead of lift loss and drag increase.

At the leading edge separated vortex, a new attachment line has formed which halved the vortex in size. Below the leading edge separated vortex, separation occurs which is being spread out towards the trailing edge over the first and second control surface. The control surfaces themselves show signs of severe separation as well. Only the region where the leading edge separated vortex still flows over the second and third control surface no direct separation is observed, but the rest of the area of the control surfaces do not show any aligned flow anymore. This also means that the effectiveness of the control surfaces are zero to minimal, as it is not investigated how the flow behaves around the control surfaces at these high angles of attack. Also, at these high angles of attack, the flow makes the aircraft unstable such that any control effectiveness would not create a large enough compensation for the wing to be statically stable again, as seen in figure 4.6.

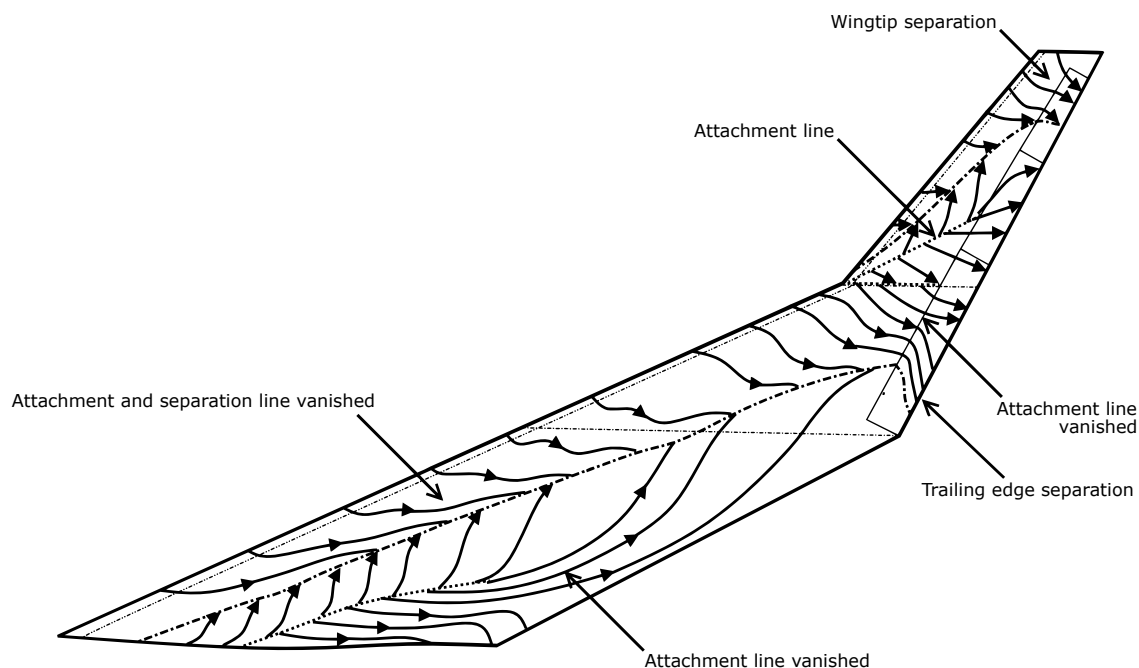


Figure 4.31: Oil visualisation for 41 degrees angle of attack

After the maximum lift coefficient has been reached, it is seen in figure 4.2 that after the lift loss a region of lift recovery occurs. This is estimated to be around 50 degrees angle of attack. The results with respect to this angle of attack can be found in figure 4.32. At this angle of attack it is seen how the flow pattern is showing increased regions of separation and decreased regions of vorticity and cross-flow.

For the primary vortex, it is seen how the separation line moved down and decreased the size of the vortex. The separation line is not a straight line any more and shows a curve pattern, where on the one side the vortex flow separates from the surface and on the other side the separated flow from the leading edge is moving towards the oil towards to separation line. Where the vortex on the surface first showed streamlines almost vertical towards the tip, the streamlines are now more parallel to the trailing edge, indicating the strength has decreased. At the start point of the primary vortex, the separated line and the attachment line come to a point, and do not let the vortex start at the root any more. This region is now fully dominated by the boundary layer of the splitter plate and shows a large region of separation near the trailing edge.

At the control surfaces it can be seen that all control surfaces have an attachment line at their leading edge, indicating the air from the pressure side is being pushed towards the suction side. After the renewal of the boundary layer, the air flow goes directly into a trailing edge separated flow and do not show any sign of aligned flow. The leading edge separated vortex has grown a bigger by the attachment line being vanished, although it is still blocked by the attachment lines of the control surfaces. The wingtip itself shows regions of separation, where at the leading edge regions of aligned flow towards the separation line of the leading edge separated vortex are observed.

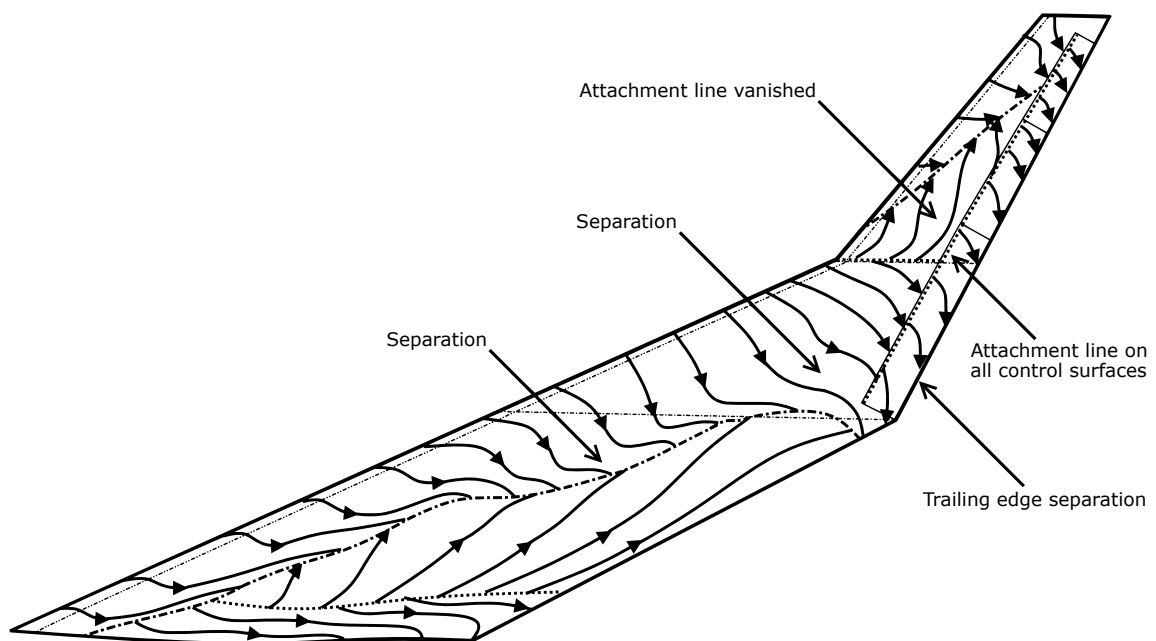


Figure 4.32: Oil visualisation for 50 degrees angle of attack

4.2.3. Tufts

Besides the experiments performed with the ultraviolet dyed oil, runs have been performed with tufts equipped on the suction side of the wing. The experiment with the tufts are conducted in order to verify the data gathered from the oil visualisation runs. The data from the oil visualisation pictures taken during the experiment led to the topology layouts for a wide range of angles of attack, providing argumentation on how the flow behaves and the lift and pitching results can be explained. By placing tufts on the surface of the wing, the same topology layouts can be made and be overlapped with the topology layouts of the oil visualisations to compare the effect of the wall shear stress factors by the flow direction of the boundary layer just above the wall. Furthermore, a video of the tufts had been made in order to check the vibrations of the tufts to provide information about unsteady and shedding flows.

The tufts in practise work the same as the ultraviolet oil and give a visualisation of how the wall shear stress factors at the surface of the wing are directed. During the experiment, the videos taken are shot with a photo camera on a stand in High Definition at a 100 frames per second to maximise data quality. Before the experiment was run, a list of angles of attack at specific time interval was made to ensure synchronisation with the camera and the angle of attack of the wing.

For the results of the tufts, two different angles of attack are chosen to investigate the results of the tufts. The angles of attack chosen are 15 and 29 degrees, for which at both angles a topology layout of the tufts has been made. The velocity set during the experiment was 18 meters per second, as is the same as performed during the experiments for the oil visualisations. An impression of the tufts layout at an angle of attack of 11 degrees can be found in figure 4.33. The tufts are made out of white coloured wool and is positioned by long stripes of yellow tape. The local velocity and direction of the flow make the tufts turn into the correct direction.



Figure 4.33: Impression of the tuft configuration at 11 degrees angle of attack

For the comparison of the tufts with respect to the oil flow visualisation, a topology layout is made. This layout for the angle of attack of 15 degrees can be found in figure 4.34. Here it is seen how the tufts are aligned to the local flow direction. As some tufts show shedding behaviour, the average of the tuft position is taken in order to show the averaged direction of the tufts at this angle of attack.

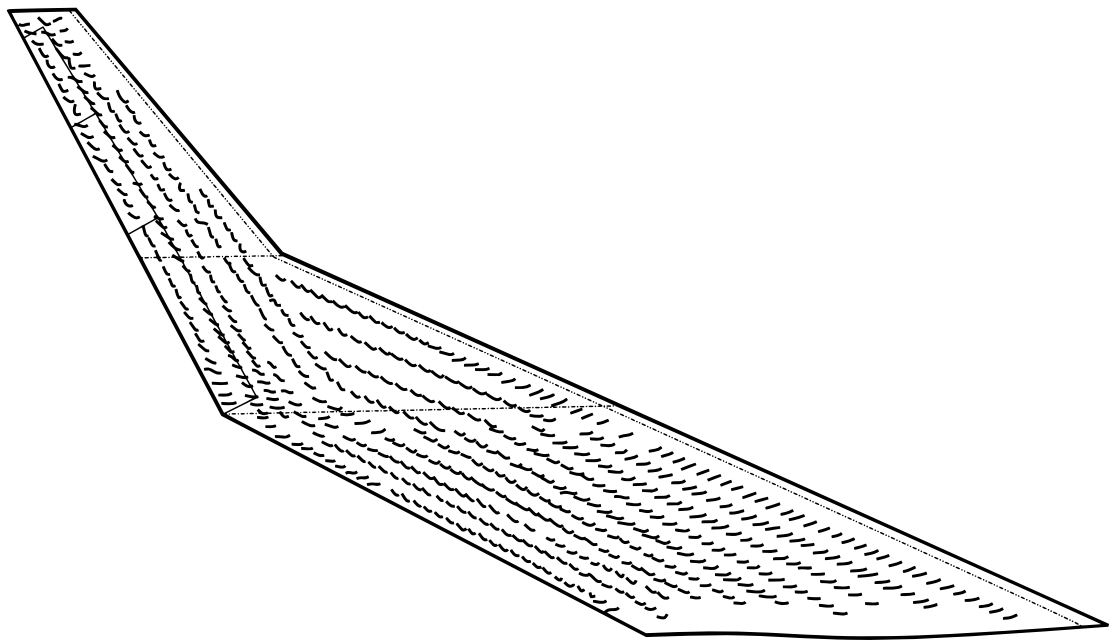


Figure 4.34: Topology layout of the tuft configuration at 15 degrees angle of attack

In figure 4.35 the comparison between the results of the tufts and the oil visualisation can be found. For the comparison, the tufts are coloured in red to show the direction of the flow. The tufts are put over the streamlines to clearly show the differences in direction of the tufts with respect to the streamlines from the oil visualisation.

In the figure it is seen that the direction of some tufts are not the same as the direction of the streaks from the oil visualisation. Five different areas are found where the direction of the tufts do not match the direction of the oil flow on the surface of the wing. The first area is from the root till the first attachment line near the lower local airfoil location. From middle chord direction towards almost the trailing edge of the wing, the tufts show a behaviour of cross-flow, while this is not the case seen from the oil. The oil runs down a little, while the tufts have the opposite direction. A second region is noticed at the trailing edge just below the trailing edge kink. Here in the oil flow it is observed how a vortex rolls up from the trailing edge onto the surface, whereas the tufts show a behaviour where the direction of the flow is away from the surface into the direction of the undisturbed flow.

A third region is located at the upper local airfoil location. In this region, the attachment line of the leading edge separated vortex creates a vortex towards its lower placed separation line. Seen from the tufts, this behaviour does not occur and the flow is towards the tip of the wing. A fourth area noticed is at the leading edge, halfway between the leading edge kink and the wingtip. According to the oil flow, the flow is aligned in a direction almost parallel to the undisturbed flow, but the tufts show a pattern which is in the direction towards the tip. A fifth and last region is noticed near the leading edge of the lower airfoil location. The oil flow indicated that the flow parallel to the direction of the undisturbed flow, while the tufts show a vortex or cross-flow behaviour parallel to the leading edge towards the leading edge kink.

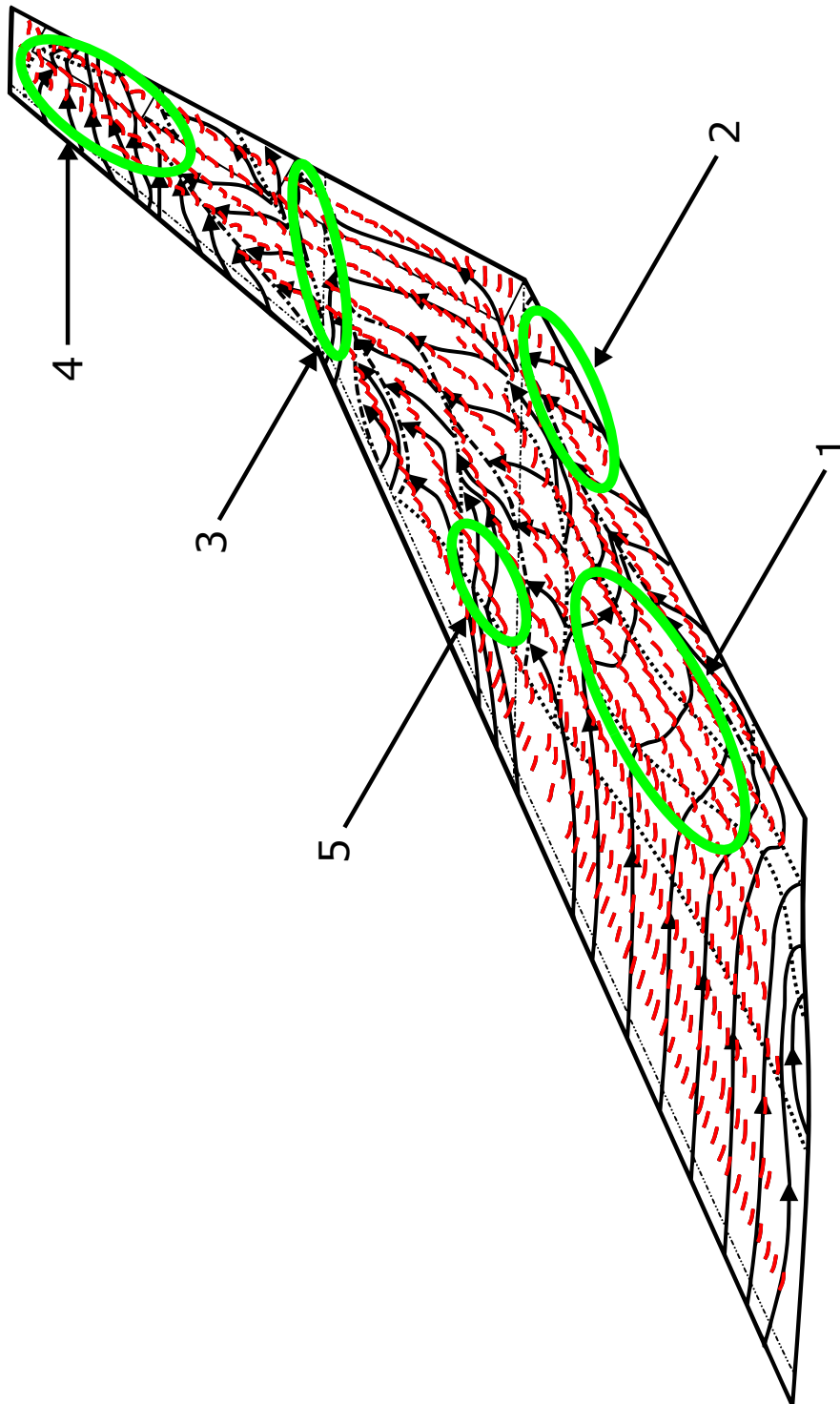


Figure 4.35: Comparison of the tuft configuration and oil visualisation at 15 degrees angle of attack

To see whether the tufts provide a correct visualisation compared to the oil flow results, another angle of attack at 29 degrees is chosen to compare the result to each other. The topology layout of the tufts at this angle of attack can be found in figure 4.36. In this figure it is seen how the tufts are put more into the direction of the wing, indicating the cross-flow behaviour observed earlier during the oil flow experiments as well.

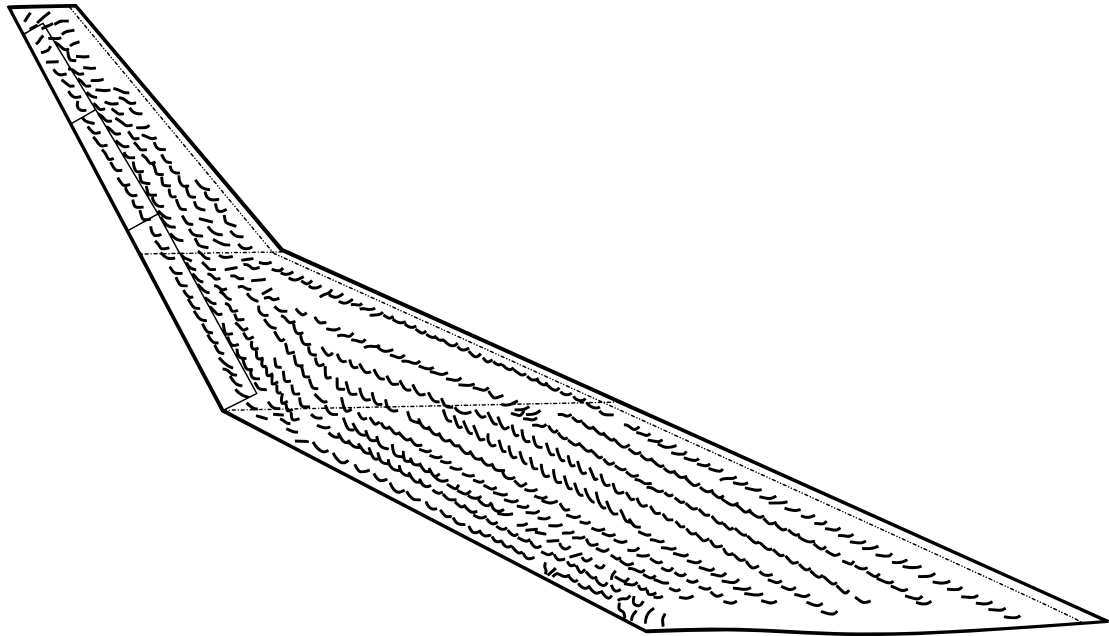


Figure 4.36: Topology layout of the tuft configuration at 29 degrees angle of attack

In figure 4.37, the comparison between the results of the tufts and the oil visualisation can be found. Again, in this figure the topology layout of the tufts is placed onto the topology layout of the oil visualisation. The tufts are coloured in red, while the streamlines from the oil visualisation are coloured in black. Also the attachment- and separation lines are indicated to make a better understanding if the comparison is made.

Comparing the tufts and the oil visualisation at this angle of attack results in a better matching overlap as was the case at the angle of attack of 15 degrees. Especially in the second and fourth region, improvements between matching directions of the tufts and the oil streaks have been observed. Between the root and the upper airfoil location, the tufts in the centre of the surface are well aligned compared to the streamlines from the oil visualisation. The only differences observed between the root and the upper airfoil location are the leading edge and the trailing edge. In the first region at the leading edge, the streamlines from the oil are in the upper direction away from the surface. The tufts however show a different direction and are directed into the separation line. In the second region at the trailing edge of the wing, the direction of the tufts are all into a cross-flow pattern, while the streamlines from the oil show a direction which indicate signs of trailing edge separation. The third region above the upper local airfoil location still shows a difference in direction between the tufts and the oil flow streamlines. The tufts show a direction towards the tip, while the oil streamlines are directed towards the trailing edge of first and second control surface.

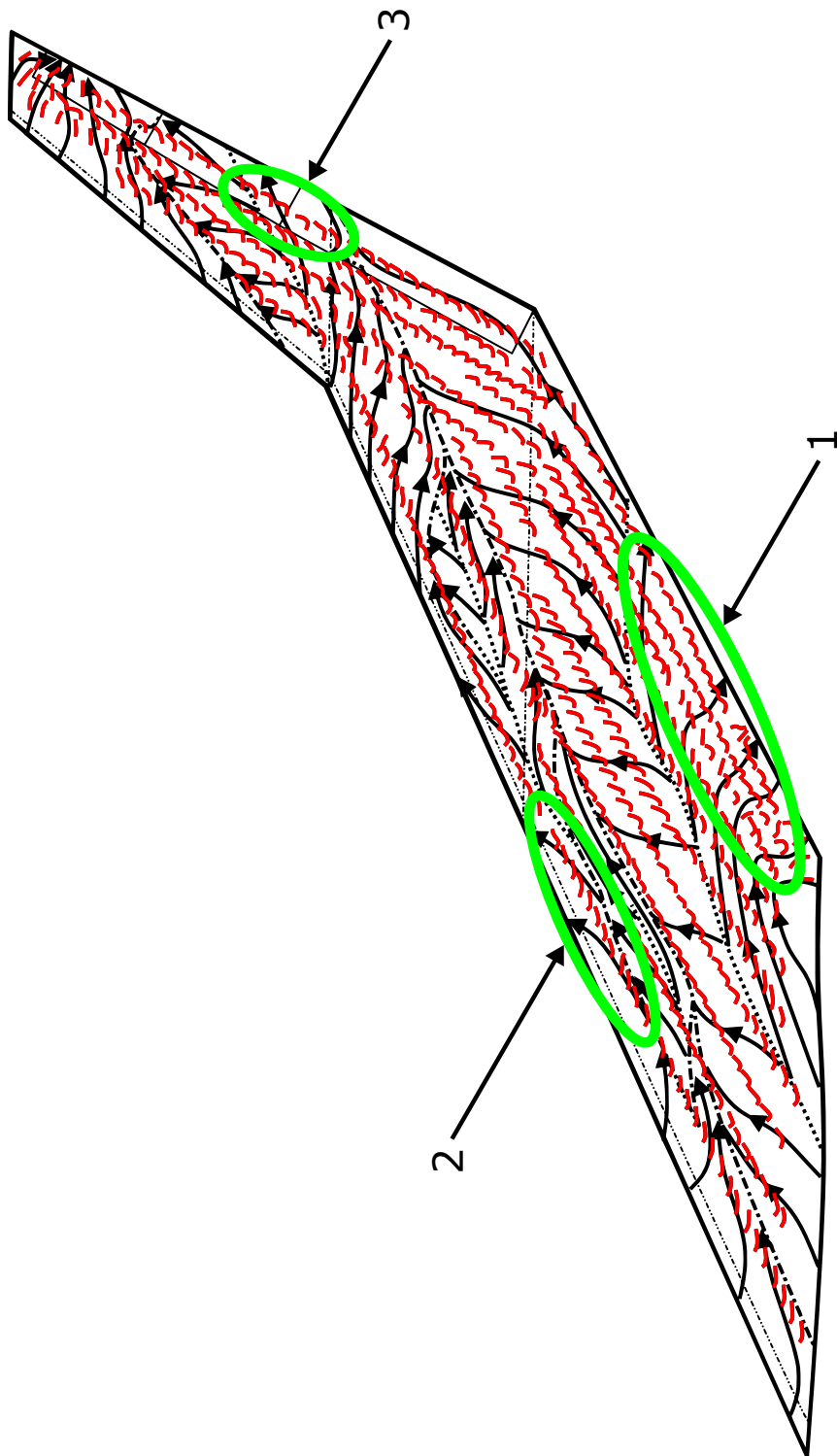


Figure 4.37: Comparison of the tuft configuration and oil visualisation at 29 degrees angle of attack

The differences in the direction between the tufts and the oil flow visualisation can be explained by the boundary layer. The first explanation is the thickness of the boundary layer, where the height of the tufts may be larger than the boundary layer thickness. It is therefore more dominated by the flow outside the boundary layer instead of within the boundary layer itself. The other explanation is that in the lower part of the boundary layer, the flow at the surface behaves differently compared to the upper part of the boundary layer. Therefore, the tufts may show a different direction compared to the oil streaks. This was also discussed by Vos and Farokhi [39], where it was shown how the flow direction within a boundary layer turned with the height of the boundary layer itself. In figure 4.38 an impression of the rotating boundary layer due to a cross-flow component can be found.

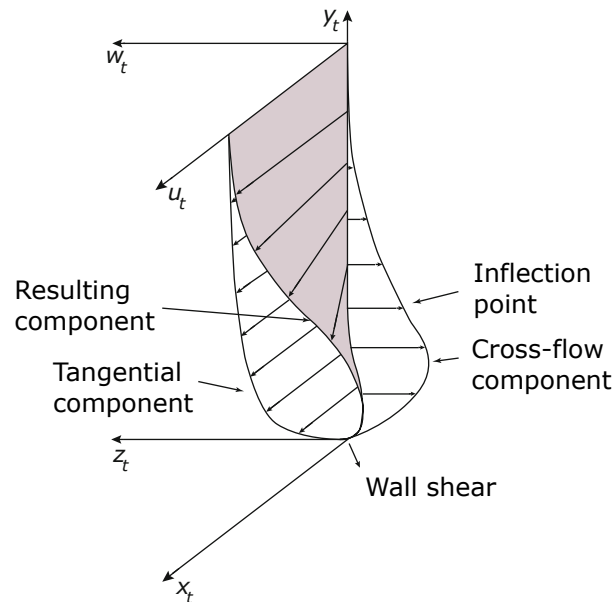


Figure 4.38: Impression of rotating boundary layer [39]

4.2.4. Smoke

The last flow visualisation method applied during the experiments was the smoke. The smoke was injected into both the undisturbed flow and the boundary layer for a range of angle of attacks at the air speed of 18 meters per second. By playing around with the amount of smoke produced and injected into the flow, the quality of the data can be adjusted. By manually fine tuning the right amount of smoke and the best layer of smoke was produced, videos of the smoke have been taken at High Definition at 100 frames per second to maximise the quality of the recorded data.

It is observed during the test that the injection of the smoke into the flow is rather sensitive to the location. As the smoke is expanded as it travels downstream, the smoke is transformed from a single line of smoke into a wider cloud. By manually trying different settings and injection location, it was observed that the cross-flows observed during the oil flow and tuft experiments are indeed vortices. This can also be seen in figure 4.39, which features the wing at 41 degrees angle of attack.

In this figure it is seen how a single line of smoke enters from the right side of the picture. The smoke follows the streamlines of the wind and visualises how the flow behaves over the surface of the wing. It is clearly seen how the smoke enters over the leading edge of the wing and changes direction due to the isobars as explained earlier by figure 4.13. Following the streamline towards the trailing edge of the wing, it is seen how the flow curls down towards the surface and into the direction of the wingtip. This creates the primary vortex which swirls over the surface in a cross-flow direction towards the tip. It is also seen that the flow is stopped by the attachment line of the leading edge separated vortex, seen earlier in figure 4.16. At the trailing edge of the wing the vortex leaves the surface and flow further downstream with the wind.

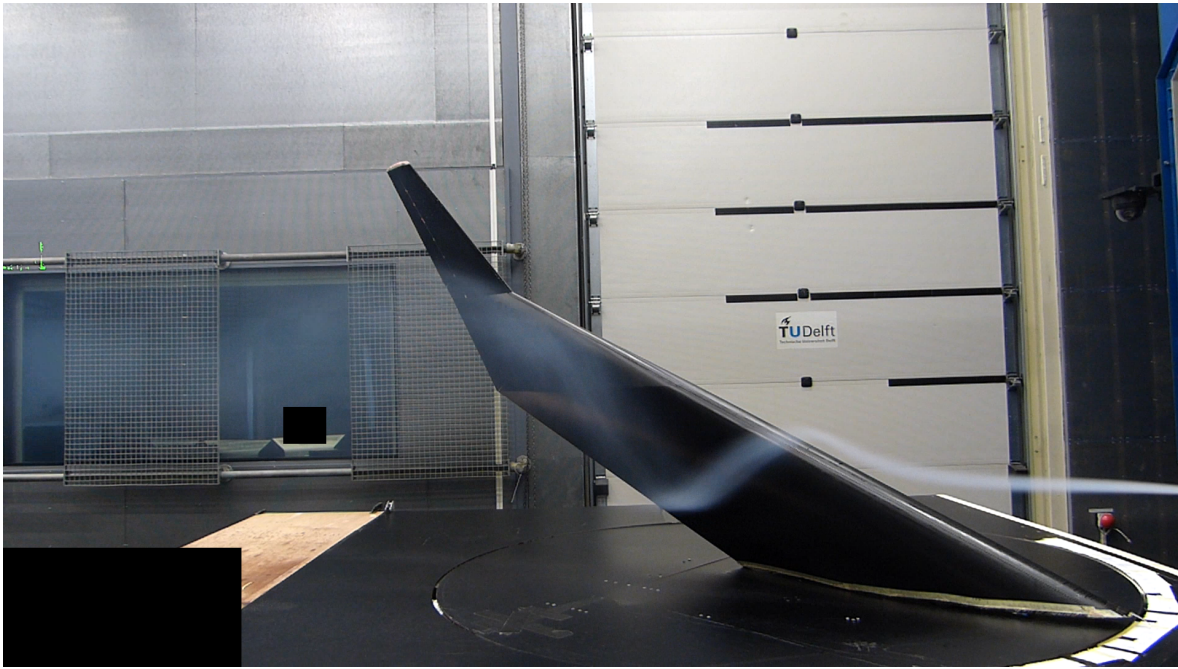


Figure 4.39: Primary vortex visualisation by means of smoke

By looking at the vortex, it is seen in figure 4.40 and 4.41 that at the pressure side of the wing a counter-rotating vortex rolls compared to the suction side of the wing at the angle of attack of 41 degrees. By looking at how the smoke curls over the suction side of the wing, it is seen how it moves towards the tip, as it leaves the surface and continues as a vortex. At the pressure side of the surface, it is not visible what happens on the surface, but seen how the smoke behaves at the trailing edge of the wing, at the surface the smoke has to go into a cross-flow direction towards the tip as well. Then it rolls up in the counter-rotation motion compared to the vortex from the suction side of the wing. In figure 4.42 an impression can be found where the smoke goes over both sides of the surface. Here it is also seen how the vortices at both sides of the surface move in a counter-rotating motion.



Figure 4.40: Vortex at the suction side of the wing visualised by means of smoke

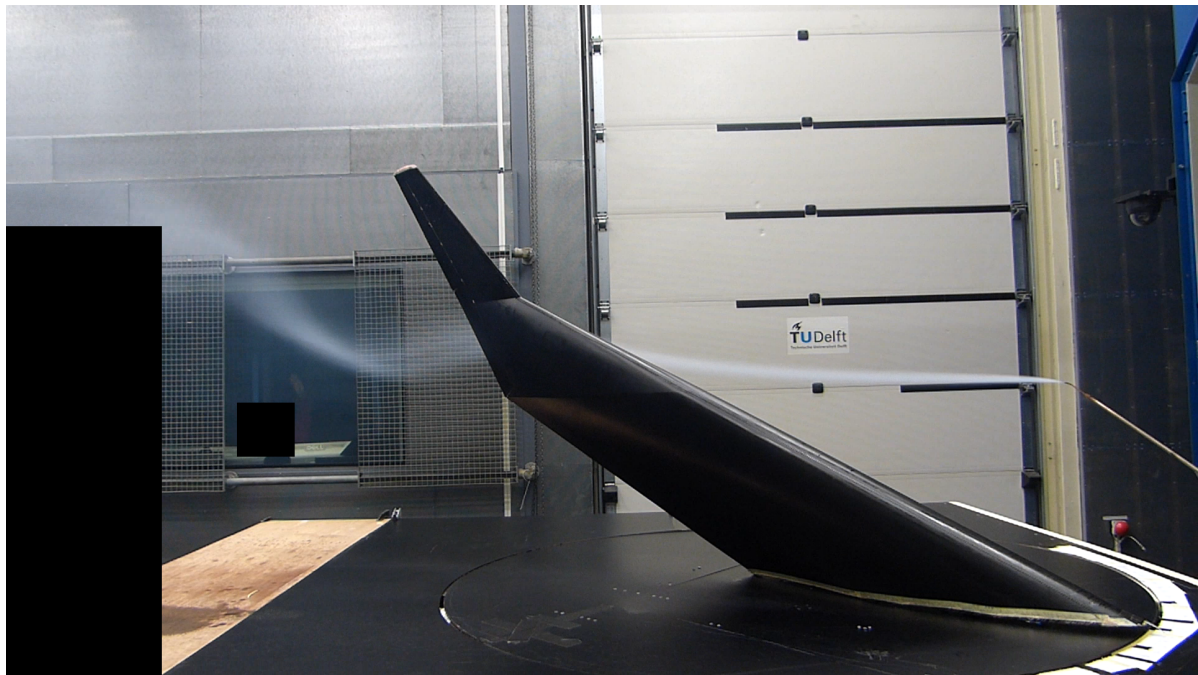


Figure 4.41: Vortex at the pressure side of the wing visualised by means of smoke

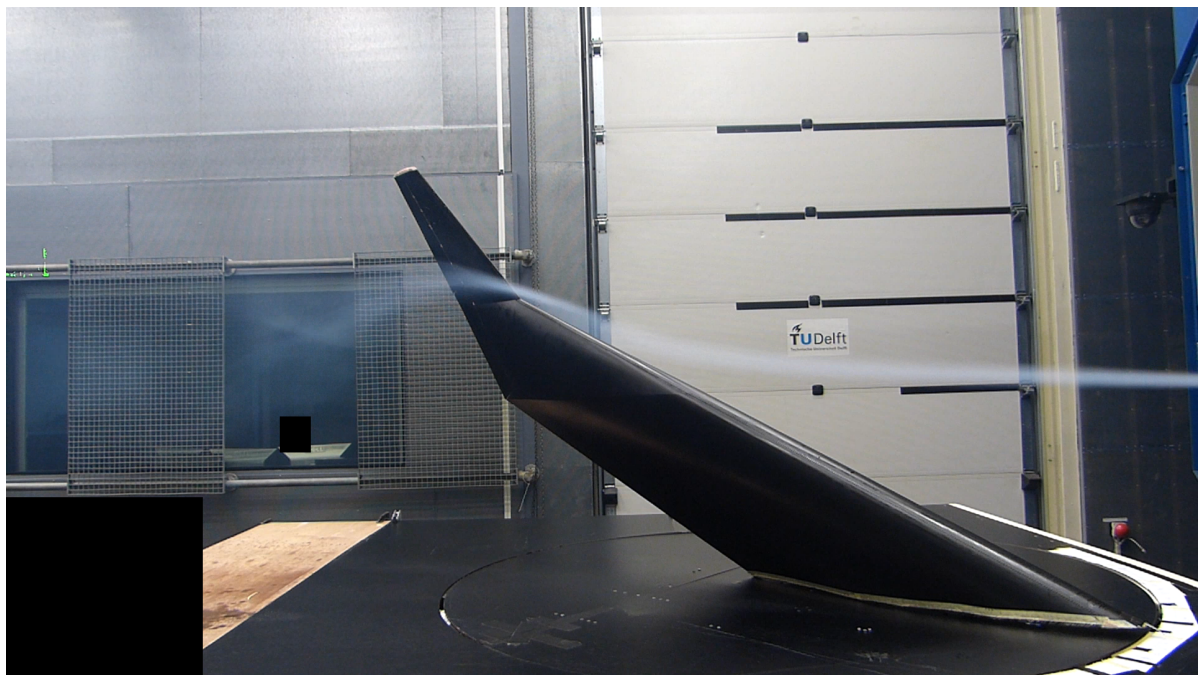


Figure 4.42: Counter-rotating vortices at both sides of the wing visualised by means of smoke

Looking into the leading edge separated vortex, in figure 4.43 at 12.5 degrees angle of attack it is seen how the smoke is positioned at the location where the separation line is located. In the picture it is shown how the smoke is not visible in the middle section between the two fronts of smoke. This indicates that the lower part of the smoke is curling away from the surface into the leading edge separated vortex. The upper side of the smoke front is aligned flow and moves into the separation line. Seen from the oil this front should go into the separation line, but with the smoke it is clearly seen that a region of clean air without smoke is located above the separation line.

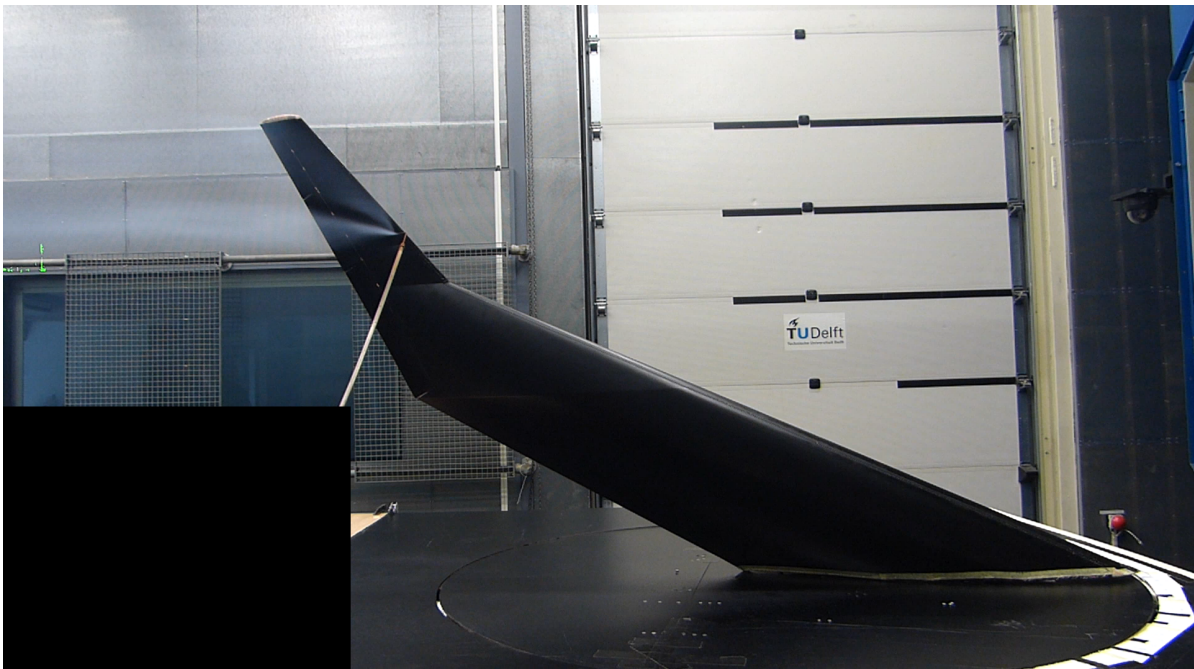


Figure 4.43: Leading edge vortex visualised by means of smoke

In figure 4.44 the smoke around the wingtip is shown. By looking into the picture it is observed how the smoke visualises the wingtip vortex which is present at 41 degrees angle of attack. At the tip is also seen how the smoke expands away from the tip. The vortex behaviour at the tip is explained by the interaction of the suction and pressure side of the wing by the finite tip.



Figure 4.44: Wingtip vortex visualised by means of smoke

From the smoke visualisation results it is confirmed that the cross-flow behaviour with the attachment and separation lines observed in the oil flow pictures in section 4.2.2 are indeed vortices curling over the suction side of the wing. Also the separation line of the leading edge separated vortex is clearly visible and confirms that the vortex is separated at this line. During the experiment the location of the core of the vortex was also observed and confirms the cross-flow over the surface are vortices.

5

Preliminary Flight Discussion

The wind tunnel results are known and therefore in this chapter an interpretation in the form of a discussion towards the preliminary flight is made. First, the stall behaviour is analysed in section 5.1. Then, in section 5.2 the trimmed flight is discussed, followed by the discussion on the implication on approach in section 5.3.

5.1. Stall Behaviour

As the results from the balance and the flow visualisations have been presented and discussed in chapter 4, in this section the results are combined to discuss the stall behaviour of the wing. For the discussion on the stall behaviour, the wind tunnel experiment results of the half wing model are used. During the flight test, a slightly different stall behaviour may occur than is discussed in this section. As this is a preliminary discussion, the discussion must therefore be considered as an indication towards the first flight instead of a pilots handbook.

During the wind tunnel experiments, the reference angle of attack was attempted to be positioned at the geometrical zero angle by means of lasers. Since it was not possible to verify this angle with the flow direction from the nozzle, during real flight there may be a slight difference in true angle of attack. This means that both the lift and moment curves are shifted by the error in angle of attack, but are not changed in magnitude.

From section 4.1.1 it was seen how the lift curve behaves for each angle of attack. From the results it was seen that the lift curve at low angles of attack below ten degrees had a lift slope of about 0.03. The lift slope was constant and the lift coefficient could therefore be computed by the linear behaviour at low angles of attack. From the results of the oil visualisation it was seen that up to the angle of attack of nine degrees, no vortices and minor cross-flow at the trailing edge was observed on the suction side of the surface.

From eleven degrees onward, a leading edge separated vortex was seen originating from the leading edge kink. This small vortex between the leading edge kink and the wingtip introduced a small increase in the lift slope [49]. From thirteen degrees onward, a vortex was observed at the trailing edge of the wing below the trailing edge kink. This vortex evolved with increasing angle of attack into the primary vortex and became a leading edge vortex. The primary vortex showed signs of the vortex described by Luckring [10] coming from a blunt leading edge. These vortices were not created at the nose and originated more aft at the leading edge in the direction towards the tip of the wing. From his investigation it was also shown how a constant chord wing with an ONERA D airfoil at 50 degrees sweep angle had a very large increase in angle of attack range compared to conventional aircraft with highly swept wings. The experiment was performed at a Reynolds number of $2.3 \cdot 10^6$. This way, the Flying V can be compared to delta wings, which feature the same kind of lift characteristics based on the leading edge vortices, vortex lift and the large range of angles of attack before the wing stalls [50].

As the vortex at the trailing edge increased in strength with increasing angle of attack and the flow over the surface kept on developing, the centre of pressure was moved in the aft direction. The direction caused the stability derivative to be negative and the moment curve to have a negative trend as well. This trend was present till the angle of attack of 20 degrees. From this angle onward, the various small vortices became one larger vortex and was referred to as the primary vortex. The development of the primary vortex with increasing angle of attack was that it moved forward and therefore placed the centre of pressure more forward as well. This caused the stability derivative to be positive and the moment curve to change direction.

As the primary vortex was formed from the smaller surrounding vortices as the angle of attack was increased from 20 degrees onward, the lift slope was decreased in magnitude. This caused the lift curve to rise slower with increasing the angle of attack. Compared to the wing without any vortex lift, the lift coefficient on the Flying V due to the vortex lift at 21 degrees angle of attack was increased by 0.128, which was a lift increase due to the vortices of about 19%. From this angle onward, the lift gradient lowered as the primary vortex moved forward and more separation was localised at the trailing edge and the root of the wing.

This is also clearly seen in figure 5.1. In this figure, the lift and moment coefficient are plotted against the streamlines from the oil visualisation. It is seen how the leading edge separated vortex initiates the lift slope increment and how the formation and development of the vortices towards the primary vortex gives additional vortex lift. From this point onward as the primary vortex moves forward and more separation is acting on the trailing edge of the wing, the lift increases at a smaller rate towards the maximum lift coefficient at 41 degrees angle of attack. The maximum lift coefficient of the model used during the wind tunnel experiment is estimated at 1.09.

At the angle of attack of 41 degrees, the lifting forces are maximised and the increase in angle leads to a decrease in lifting forces with an increase in separation. This is seen at the angle of attack of 48.5 degrees, where the separation over the middle section of the surface and the control surfaces becomes more dominant and decreases the size of the primary vortex. Some lift recovery is present at this angle of attack, but increasing the angle further leads to complete separation of the air from the surface and loss of lift.

As can be seen in the figure 5.1, the centre of gravity location for the moment coefficient is set at a distance of 1.365 meters behind the nose. The reason for this distance is found in the section 5.2, where the trimmed flight is discussed. In this section, the optimal centre of gravity location is investigated by the influence of the deflection of the control surfaces. Therefore, these results have already been applied to figure.

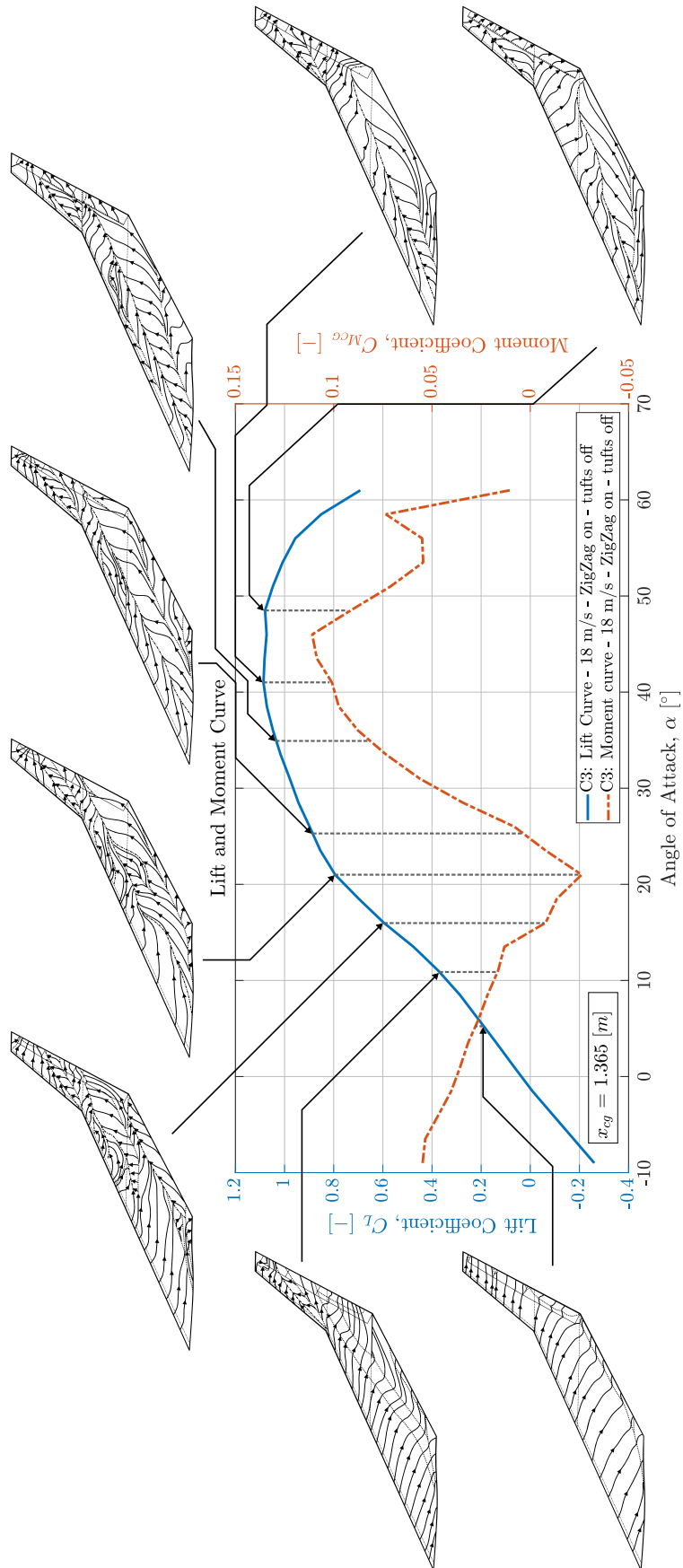


Figure 5.1: Lift and moment curve combined with the streamlines from the oil flow visualisation

5.2. Trimmed Flight

In the moment curve in figure 4.6 it was seen how the moment coefficient around the quarter mean aerodynamic chord was positive below five degrees angle and negative above five degrees angle of attack. Only at one specific angle of attack, at five degrees, the moment coefficient is zero and the aircraft is 'trimmed'. In the moment curve showed earlier, the moment coefficient was only plotted against the angle of attack for the control surfaces in zero deflection position. The trim of the aircraft can be decided by changing the angles of the control surfaces. This way, the control surfaces create an additional moment around the centre of gravity and change the shape of the moment curve. During the wind tunnel experiments, several balance measurements have been taken with respect to the variation in control surface deflection.

In section 4.1.2 it was seen how the pre-determined centre of gravity position at the location of the quarter mean aerodynamic chord, which was located at 1.234 meters behind the nose, resulted in a stable pitching derivative until twenty degrees angle of attack. From this angle onward, an increase in angle of attack led to an unstable pitching derivative. Looking into the moment curve in combination with the variation of deflected control surfaces, it was found that a complete negative deflection of the two inner control surfaces (CS1 and CS2) is not sufficient to trim the aircraft at twenty degrees angle of attack. Further investigation resulted in a new position for the centre of gravity, at 1.345 meters behind the nose. This new location of the centre of gravity makes it possible to trim the aircraft up to to 32 degrees angle of attack, even though the stability derivative at an angle of attack higher than twenty degrees is positive. In figure 5.5 the results for the moment coefficient by the variation in control surface deflection for the centre of gravity location at 1.345 meters behind the nose can be seen.

The velocity set during the experiment was twenty meters per second. During the experiment, the first and second control surface, representing the two most inner control surfaces, were taken as the control surfaces controlling the pitching of the aircraft. For the test flight, the two inner control surfaces will be used for pitching purposes, while the outer control surface will be used for roll. In figure 5.5 it is seen how the control surfaces are deflected in percentages. For the controller system the deflection input is given in percentages and this will also be used during the flight test, therefore no deflection angles are given. In table 5.1 a scheme is given of what percentage corresponds to what deflection angle. For the moment curve, it can be seen that a positive control deflection, which means the control surface is pointing downward and thus the angle of attack of the control surface is increased, leads to a stronger maximum negative pitching moment. This makes sense in the way by looking into figure 4.5, where an additional lifting force pointing in the negative y-direction makes the resultant force larger. This in combination with the increased centre of pressure distance to the centre of gravity location results in a stronger negative moment around the centre of gravity. The other way around, if the control surfaces are deflected upward, which is referred to as a negative deflection in the figure, the resultant force is smaller and thus the moment coefficient around the centre of gravity is less negative.

Table 5.1: Deflection angles for the inputs of the control surfaces

CS input value [%]	-125	-100	-75	-50	-25	0	25	50	75	100	125
CS1 deflection, α [°]	-10.5	8.3	6.4	4.2	2.1	0	2.3	4.9	6.8	10.0	12.3
CS2 deflection, α [°]	-15.2	-12.8	-9.8	-6.4	-2.8	0	3.7	7.2	10.3	14.2	17.9

For trim it is required that the sum of moments around the centre of gravity are set to zero. This way, the aircraft is stable at a certain flight state. By looking into figure 5.5, it is seen that for the deflections used during the experiment the aircraft can be trimmed between -2 and 32 degrees angle of attack for the given centre of gravity location at 1.345 meters behind the nose. As explained in section 4.1.2, the moment curve can be changed by moving the location of the centre of gravity. The movement of the centre of gravity causes the static margin to change as well. A smaller margin leads to more a quicker response from the control surface deflection against a smaller natural stability. A

larger static margin leads to more natural stability against a slower response from the control surface deflection.

By moving the centre of gravity more forward, the moment coefficient in the figure will move more down. In other words, the stability derivative is stronger in negative magnitude and gives a stronger negative maximum moment coefficient. As a result, the control surface at 125% negative deflection presented in figure 5.5 which allows the aircraft to be trimmed at twenty degrees angle of attack will not be sufficient. The point will move under the zero moment coefficient line and a larger negative control surface deflection is required to bring the moment back to zero.

The other way around, if the centre of gravity is moved more aft, the moment coefficient curves will move more up towards the positive moment coefficients. During the investigation, it was found that if the aircraft needs to be trimmed up until twenty degrees angle of attack, the most aft position of the centre of gravity is located at 1.425 meters behind the nose. The results can be found in figure 5.6. In this figure it is seen how the moment curve is moved up by moving the centre of gravity more aft. In fact, the movement of the centre of gravity leads to the fact that only three of the control surface deflections can be used to trim the aircraft, which are 75%, 100% and 125% positive deflection angle. Furthermore, it is seen how the lines up until twenty degrees angle of attack are almost horizontal to each other, which means that the stability derivative is just slightly negative and the aircraft almost becomes unstable if the centre of gravity is moved aft even further.

By looking into the centre of pressure of pressure, it is seen that with increasing angle of attack the location of the centre of pressure is moved aft. This can be seen in figure 5.2. The red dashed-dotted line indicates the location of the centre of gravity as it lies at 1.345 meters behind the nose. In the figure it can be seen that the centre of pressure is in front of the centre of gravity below ten degrees angle of attack. As the angle of attack is further increased, the centre of pressure moves aft of the centre of gravity. The behaviour is reversed from twenty degrees angle of attack onward, where the centre of pressure moves forward and eventually lies in front of the centre of gravity again.

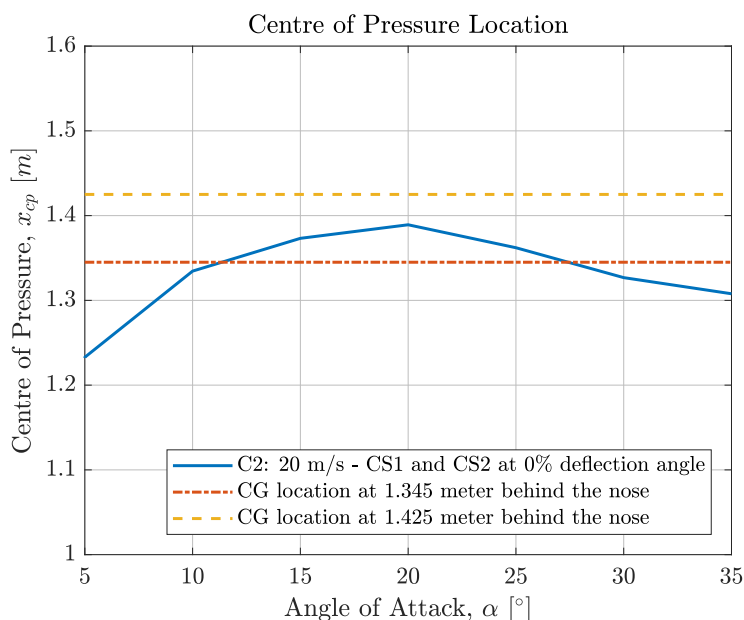


Figure 5.2: Centre of pressure compared to the centre of gravity locations for no control surface deflections

This can be very well seen in figure 5.5, where it is seen how much control deflection is required to trim the aircraft as the centre of pressure moves with the angle of attack. Below ten degrees angle of attack, the centre of pressure is in front of the centre of gravity, which means the resulting force creates a positive pitching moment. To counteract this moment, the control surfaces are deflected down to

create a positive angle of attack. This additional force of the control surfaces sets all the summed moments to zero and the aircraft is trimmed. As the angle of attack is increased towards ten degrees angle of attack, the positive deflection of the control surfaces is decreased. As the centre of pressure lies on the centre of gravity, the control surfaces are set to zero deflection and the aircraft is trimmed. As the centre of pressure moves further aft as the angle of attack is increased even more, the control surfaces need to be deflected up, providing a negative deflection angle and thus a positive moment to counteract the negative moment by the lifting force. If the angle of attack is increased from twenty degrees onward, the deflections of the control surfaces must be performed in reversed order in order to trim the aircraft.

The procedure as described above shows how the resultant force must be counteracted by means of the deflections of the control surfaces in order to trim the aircraft. In reality, as the control surfaces are deflected, the control surfaces create a lifting force, which results in the fact that the centre of pressure will move further aft with each positive deflection and will move forward with each negative deflection. This can be seen in figure 5.3.

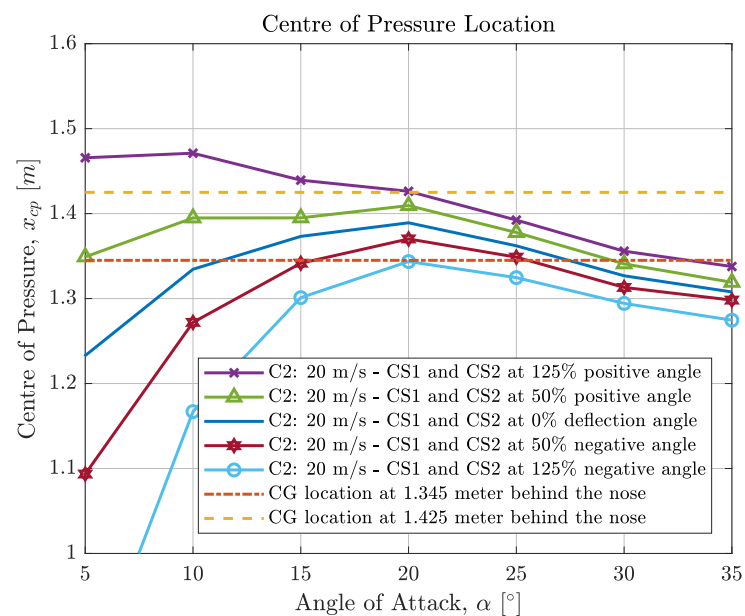


Figure 5.3: Centre of pressure compared to the centre of gravity locations for multiple control surface deflections

In this figure it is also directly seen why the most aft limit of the centre of gravity is at 1.425 meters behind the nose. It can be seen that the maximum positive deflection at 20 degree angle of attack is at the centre of gravity line. This means that from this point onward as the angle of attack is increased, no further centre of pressures are crossing the centre of gravity line to make the moment coefficient as seen in figure 5.6 zero. If the centre of gravity is put further aft, the centre of pressure of the resultant force (which includes the lifting force of the wing and the control surfaces) will never cross the centre of gravity line. This way the aircraft can never be trimmed.

Putting it the other way around, by moving the forward centre of gravity position more forward, the centre of pressure location of the resultant force for negative deflections will not cross the centre of gravity position any more. This way, there is a region in the flight performance where the aircraft can not be trimmed. In theory, the control surfaces should allow for more negative deflection angles in order for the aircraft to be trimmed if the centre of gravity is moved more forward than 1.345 meters behind the nose.

Seen from flight point of view, it is important to achieve high angles of attack up to twenty degrees for approach. This will also be discussed in section 5.3. From cruise point of view it is important to

fly with as less control surface deflection as possible to minimise drag. Therefore an investigation has been made where the centre of gravity needs to be located in order to trim the aircraft at different flight speeds, by keeping the control surfaces at zero deflection angle.

For the flight speed of 25 meters per second, the aircraft without using any control surfaces needs a lift coefficient which is reached at 9.6 degrees angle of attack. For a flight speed of 30 meters per second it is flying at 6.6 degrees angle of attack, while for a flight speed of 35 meters per second it is flying at 4.6 degrees angle of attack. This means that for each different cruise speed, there is an optimal point for the centre of gravity where the drag of the aircraft is minimised. Flying with a flight speed of 25 meters per second, the optimal centre of gravity location is at 1.330 meters behind the nose. For a flight speed of 30 meters per second, the optimal location is at 1.275 meters behind the nose, while for a flight speed of 35 meters per second the optimal location of the centre of gravity is at 1.220 meters behind the nose. The curves for the moment coefficients at these centre of gravity locations can be found in Appendix B. Using the data from the moment coefficients, it is seen that as the centre of gravity is positioned at 1.330 meters behind the nose, the aircraft can be trimmed from -2 to 17 degrees angle of attack. If the the centre of gravity positioned at 1.275 meters behind the nose, the aircraft can be trimmed between -2 and 13 degrees angle of attack. By placing the centre of gravity at 1.220 meters behind the nose, the aircraft can be trimmed between -2 and 11 degrees angle of attack. In table 5.2, a summary of the results discussed above is presented.

Table 5.2: Centre of gravity location investigation

Flight speed, V [m/s]	25	30	35
Optimal CG location, x_{cg} [m]	1.330	1.275	1.220
Horizontal flight angle, α [°]	9.6	6.6	4.6
Minimum trimmed angle, α_{trim} [°]	-2	-2	-2
Maximum trimmed angle, α_{trim} [°]	17	13	11

As the aircraft does not have a tail, it is for this purpose assumed that the neutral point coincides with the aerodynamic centre. As earlier explained in section 4.1.2, the neutral point represents the point where the centre of pressure of the resultant force creates either a pitch up or a pitch down moment. In figure 5.4 the neutral point of the twenty meters per second experiment can be seen for the wing with no control surfaces deflected. In here, it is also seen how the neutral point is located with respect to the two centre of gravity locations which were earlier identified for pitching control reasons.

In the figure it is seen how the neutral point lies aft of both the centre of gravity locations. Furthermore it is shown that the forward centre of gravity location has an increased distance with respect to the neutral point compared to the aft centre of gravity location. This increased distance leads to a bigger static margin. The static margin is a reference in percentages to indicate how the stability and control surface deflection strength are for the aircraft. It is commonly used that an aircraft needs to be designed with a centre of gravity which lies with a 5%-15% static margin in front of the neutral point. The static margin is taken as the distance between the centre of gravity and the neutral point over the length of the mean aerodynamic chord. If the forward centre of gravity location of 1.345 meters is used, the averaged static margin up to 15 degrees angle of attack is estimated to be about 11%. For the aft centre of gravity location of 1.425 meters the averaged static margin up to 15 degrees angle of attack is estimated to be about 1.5%.

As the static margin of the most aft location is too low for stability and handling purposes, it is advised to put the centre of gravity more forward. The most forward centre of gravity location has the disadvantage that at 20 degrees angle of attack the control surfaces are at their limit to set the moment coefficient to zero. Furthermore, this also means that because they act as trim and elevators, they can not be further deflected. Therefore it is advised to put the centre of gravity more aft in order to create more deflection space for the control surfaces to trim and pitch at 20 degrees angle of attack. It is not advised to put the centre of gravity too far aft, as the static margin may get too small. Furthermore, a centre of gravity position which is too far aft results in higher drag as well. An investigation into this

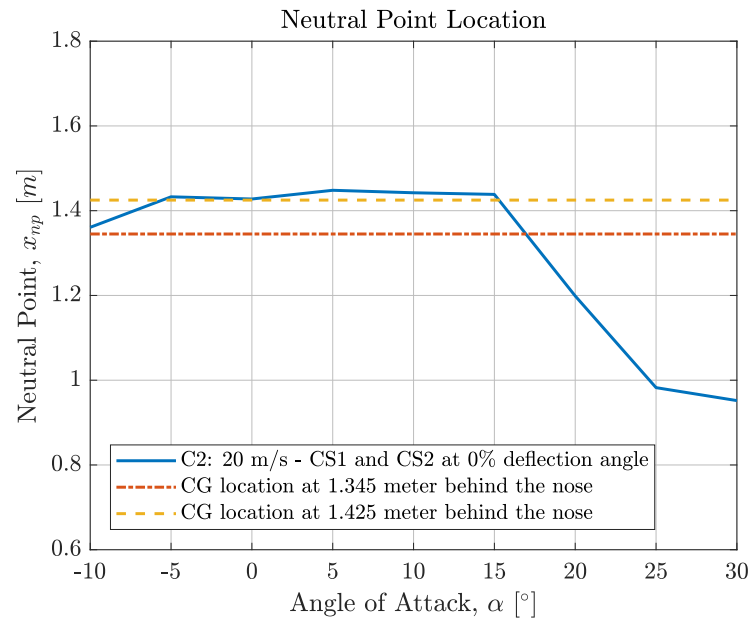


Figure 5.4: Neutral point compared to the centre of gravity locations

optimised location has been made and it is advised to put the centre of gravity at 1.365 meters behind the nose. This results in an averaged static margin of about 9%, while enough room is left for the control surfaces to give additional deflection for pitch control when they are trimmed at high angles of attack. An overview of the static margins found during the analysis can be found in table 5.3.

Table 5.3: Static margin investigation

	Most forward CG location	Opt. CG location	Most aft CG location
CG location, x_{cg} [m]	1.345	1.365	1.425
Static margin, SM [%]	11	9	1.5
Min. trim angle, α_{trim} [°]	-2	-2	-2
Max. trim angle, α_{trim} [°]	32	28	20

In figure 5.7 the moment curves for all the control surface deflections for the optimal centre of gravity location can be found. In here it can be seen that round twenty degrees angle of attack the aircraft has enough control left to manoeuvre, while the static margin is placed at around 9%. In the figure it is seen as well that the aircraft is trimmable from -2 up to 28 degrees angle of attack.

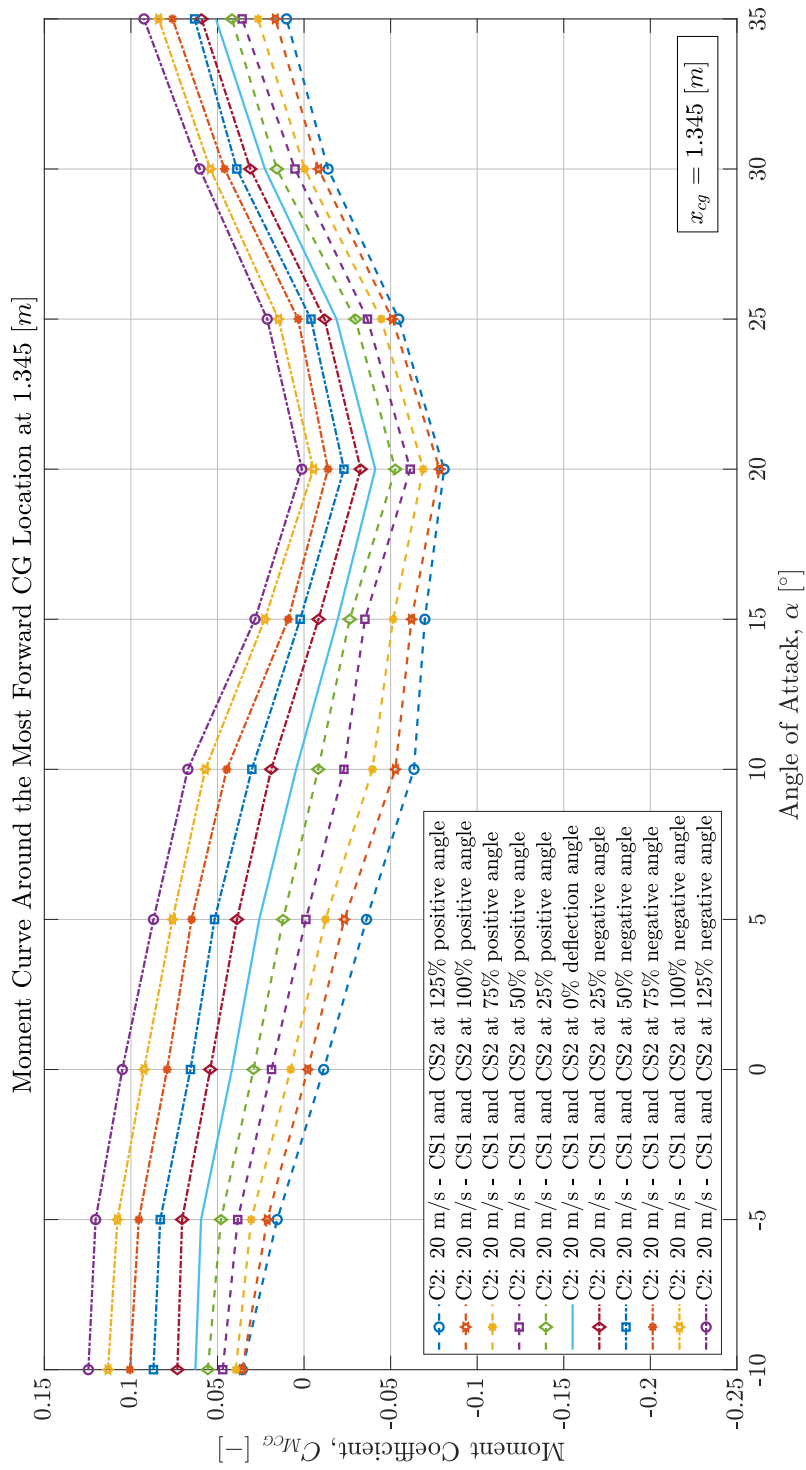


Figure 5.5: Moment coefficient comparison for the control surface deflections with the CG at 1.345 meters behind the nose

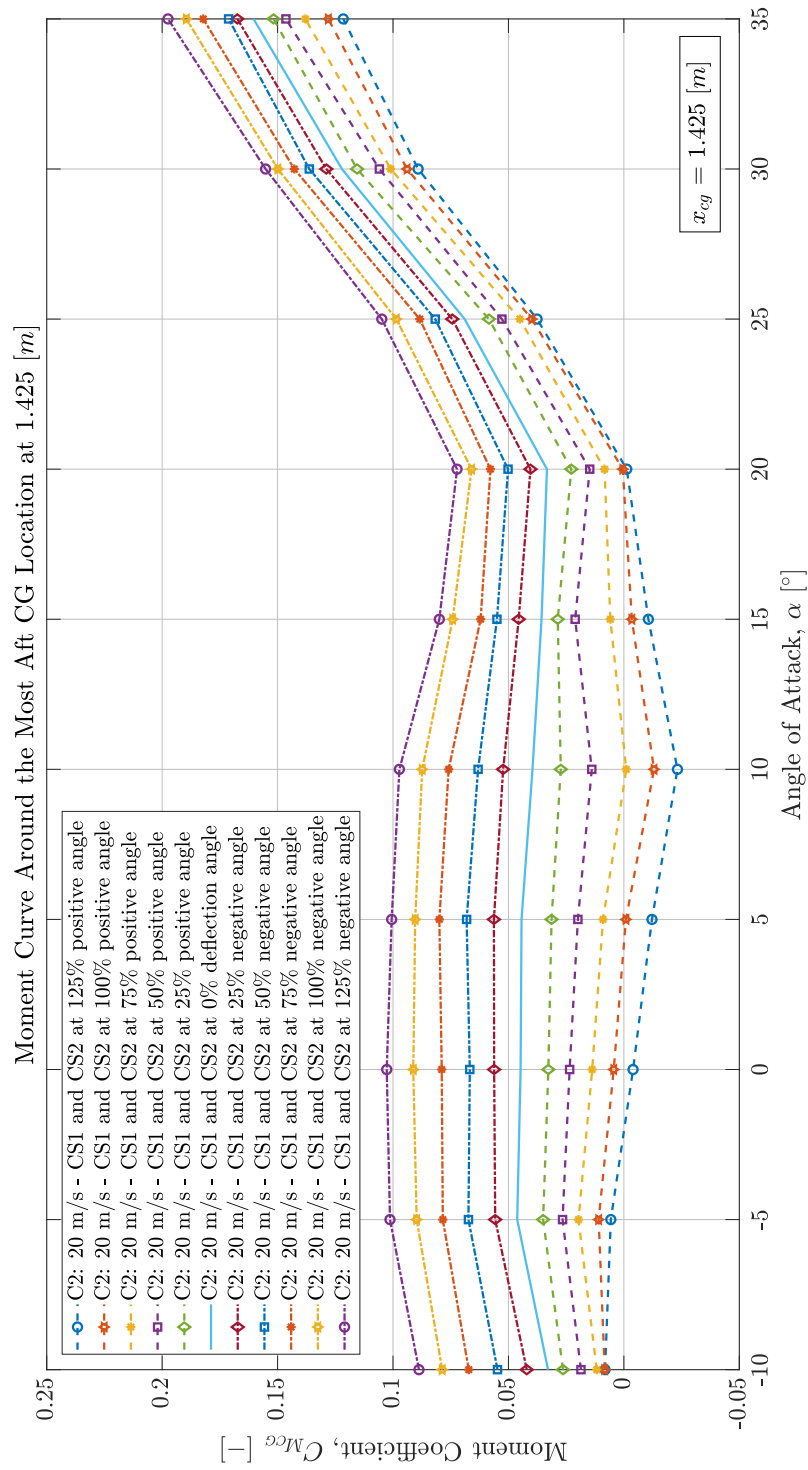


Figure 5.6: Moment coefficient comparison for the control surface deflections with the CG at 1.425 meters behind the nose

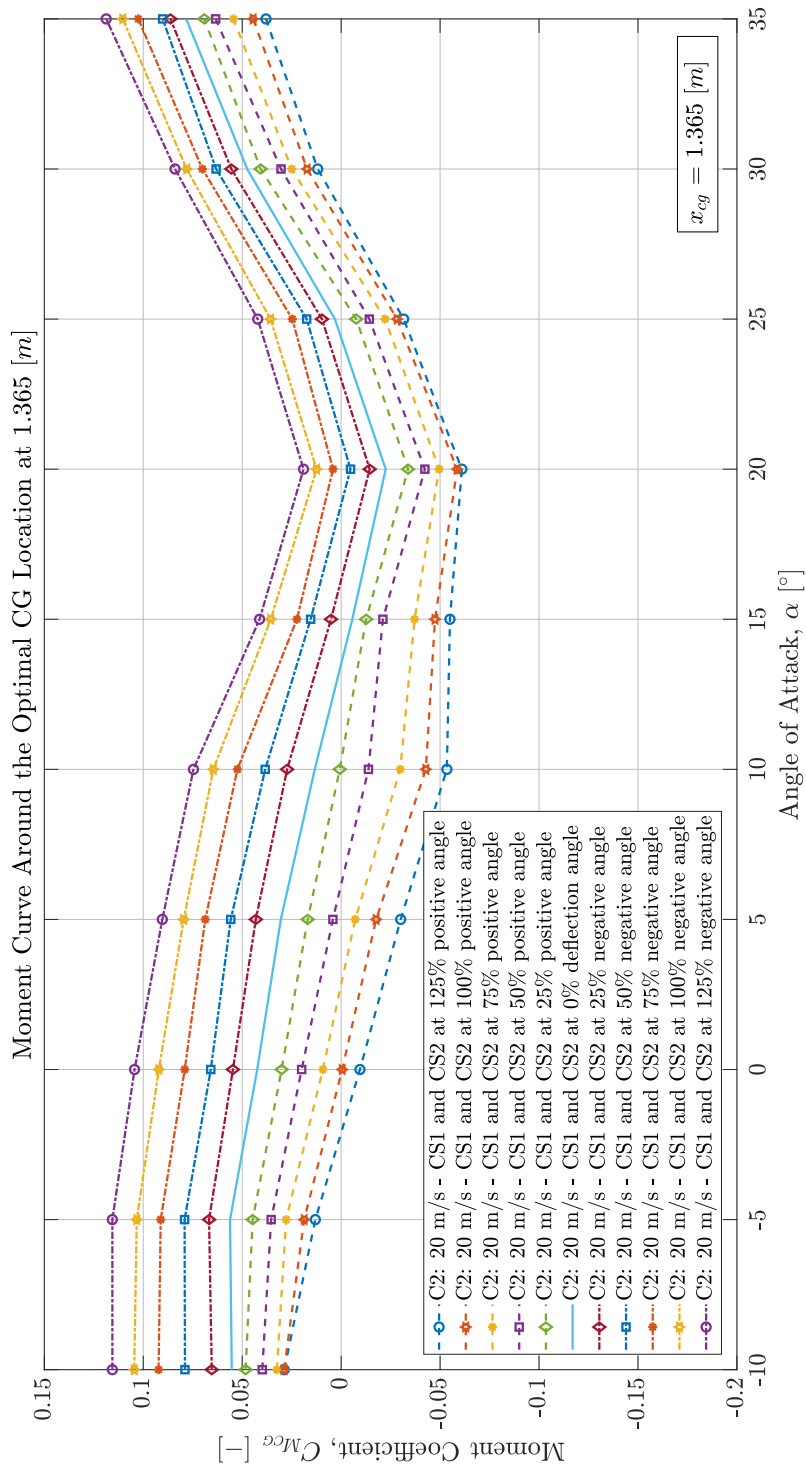


Figure 5.7: Moment coefficient comparison for the control surface deflections with the CG at 1.365 meters behind the nose

5.3. Approach Implications

In this section the approach implication with respect to the findings from the stall behaviour in section 5.1 and the trimmed flight in section 5.2 will be discussed. In the last section it has been discussed how the aircrafts centre of gravity influences the trim. The trim of the aircraft makes the lift of the aircraft change as well. This therefore means that the centre of gravity influences the lift of the aircraft as well. Furthermore, as the stall behaviour is known, it leads to a way to combine the lift and trim properties of the aircraft to identify what happens during approach.

By looking into the trim of the aircraft, it is found that a positive deflection of the control surfaces leads to an increase in lift, while a negative deflection leads a decrease in lift. To see how the lift changes for trimmed conditions at each angle of attack, an investigation has been made into the trimmed lift. For each angle of attack, the trim angle has been found, which corresponded to a certain lift coefficient. This was done for three different centre of gravity locations, namely the two centre of gravity limits for the most forward and aft position and the optimal centre of gravity location as suggested in the previous section. The results can be found in figure 5.8, where it is seen how the lift coefficient varies for each angle of attack for different centre of gravity locations.

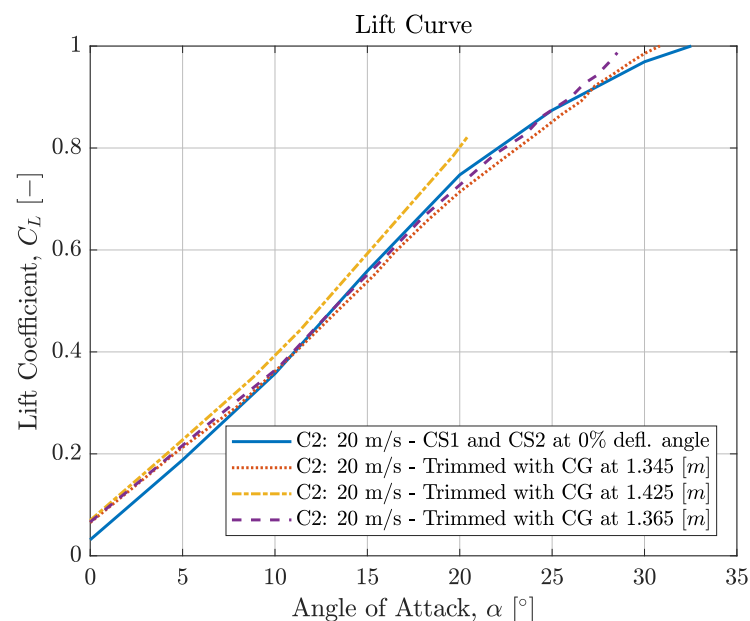


Figure 5.8: Trimmed lift curve

The results for the trimmed lift curve with a centre of gravity at the most forward position leads to a different lift curve compared to the aircraft where the control surfaces are held in neutral position. At low angles of attack, the lift coefficient is increased with respect to the original wing without control surfaces deflected. At about eleven degrees angle of attack, the behaviour is reversed and the lift is decreased with respect to the original wing. At about 27 degrees angle of attack, the behaviour is reversed into an increased lift coefficient compared to the original wing. The explanation for this behaviour can be found in figure 5.5, where it is seen that both positive and negative control deflections are required to trim the aircraft. At low angles of attack, the control surface deflections are positive, which leads to an increased lift coefficient. From eleven degrees onward, the control surfaces are switched from a positive deflection into a negative deflection in order to trim the aircraft. The maximum negative trim at twenty degrees angle of attack also leads to the largest decrease in lift coefficient of about -4.5%. From this angle onward, the control surfaces are deflected into the positive direction, leading to a reversal into the positive lift from 27 degrees angle of attack onward.

By looking into figure 5.8, it is seen how the most aft centre of gravity position leads to an increased lift coefficient. The increased lift coefficient is explained by the continuously positive deflected control surfaces. This is required, otherwise the aircraft can not be trimmed, as seen in figure 5.6. What can

be seen as well, is that the aircraft can only be trimmed up to twenty degrees angle of attack, while the moment coefficient drastically increases and not enough control deflection can be given in order to trim the aircraft. The averaged increase in lift coefficient is estimated to be about +7% compared to the untrimmed lift curve of the aircraft.

The trimmed lift curve for the optimal centre of gravity location found in figure 5.8 leads to a behaviour compared to the most forward centre of gravity location, but then with less lift deviations with respect to the untrimmed aircraft. At twenty degrees angle of attack, the difference with respect to the untrimmed aircraft is estimated to be about -2%. Seen from figure 5.7, the control surface deflections are optimised to fly at high angles of attack with the possibility to allow pitch input as well, against the lowest possible drag during flight. At five degrees angle of attack, the lift difference with respect to the untrimmed aircraft is about +13%, while this is about zero at thirteen degrees angle of attack. The reversal from a negative lift to a positive lift difference is made around 25 degrees angle of attack. By looking into the lift coefficient of the optimised centre of gravity location at 1.365 meters behind the nose, the lift coefficient is slightly different compared to the non trimmed lift coefficient. Considering the equation for the lift required during flight, the flight speed and the lift coefficient are the only two variables which can still be influenced during this stage of the development of the aircraft. This is because the design of the aircraft is finalised and will not be altered. The formulation for the lift can be found in equation 4.2.

As the weight of the full wingspan aircraft is 25 kilograms and the surface area is estimated to be 1.86 squared meter, the lift coefficient at different flight speeds can be calculated according to equation 1.1 and 1.2. At 25 meters per second, the lift coefficient required for flight is 0.34, while for a flight speed of 30 meters per second the lift coefficient required is 0.24. At a flight velocity of 35 meters per second, the required lift coefficient is 0.18. Looking into the trimmed lift curve of the optimised centre of gravity location, the flight angles for a flight speed of 25, 30 and 35 are 9.4, 5.7 and 3.6 degrees angle of attack respectively. A comparison with the untrimmed aircraft can be found in table 5.4.

Table 5.4: Angles of attack during trimmed flight

	$V = 25 [m/s]$	$V = 30 [m/s]$	$V = 35 [m/s]$
Lift coefficient, $C_L [-]$	0.34	0.24	0.18
Untrimmed angle of attack, $\alpha [^\circ]$	9.6	6.6	4.6
Trimmed angle of attack, $\alpha [^\circ]$	9.4	5.7	3.6
Difference in angle of attack, $\Delta\alpha [^\circ]$	-2.1	-13.6	-21.7

Going from flight speed towards approach speed, the velocity of the aircraft decreases as it prepares for landing. Landing is not covered in this thesis research, as it is out of the scope of the research and is not experimentally tested for ground effects. The approach speed is defined as 1.3 times the stall speed of the aircraft [51, 52]. The stall speed of the aircraft is calculated by the angle at which the aircraft can still be trimmed, namely at 28.5 degrees angle of attack. At this angle, a lift coefficient of 0.98 is reached. As the aircraft is unstable due to the positive stability derivative, the last angle at which the aircraft can be trimmed in stable flight is at twenty degrees angle of attack. The corresponding lift coefficient to this angle is 0.73. The actual 'stall angle' of the aircraft can therefore not be achieved. As seen in section 5.1, the flow reaches a maximum lift coefficient around 41 degrees angle of attack. As this angle is not achieved due to trimming limitation as shown in section 5.2, the 'stall angle' is therefore set by the maximum angle for trim, which is at 28.5 degrees. Taking this number into account, the lowest flight speed attained at 28.5 degrees is by equation 4.2 calculated to be 14.8 meters per second. The flight speed at the angle of attack of 20 degrees is estimated to be 17.2 meters per second, which is referred to as the 'safe' stall speed. Taking the regulations for approach into account, the approach speed for the lowest flight speed is estimated to be 19.2 meters per second, which is faster than the speed set at 20 degrees angle of attack. At the flight speed of 19.2 meters per second, the aircraft flies at a lift coefficient of 0.58 at the angle of attack of 15.9 degrees. According to figure 5.7, during approach the aircraft will therefore fly with the control surfaces deflected at about -25%. As a result, the aircraft will fly statically stable with enough deflection angle left for the control surfaces to control the pitch. An overview of the results for the stall and approach speed can be found in table 5.5.

Table 5.5: Flight speed and angle of attack for trimmed approach

	Approach speed	'Safe' stall speed	Stall speed
Velocity, V [m/s]	19.2	17.2	14.8
Trimmed angle of attack, α [°]	15.9	20.0	28.5
Trimmed lift coefficient, $C_{L_{trimmed}}$ [-]	0.58	0.73	0.98

Based on the results presented in table 5.5, the advised location for the centre of gravity and the analysis into the flow behaviour of over the wing, the flight characteristics during flight and approach have been investigated. The approach and stall speed in combination with the trimmed angle of attack and lift coefficient are determined, along with the location for the centre of gravity for a statically stable flight. Together with the analysis into the flow behaviour, the flight characteristics of the aircraft in preparation for the test flight are known and have led to a first impression of the handling of the Flying V. In figure 5.9, the overview of the location for the centre of gravity investigation can be found.

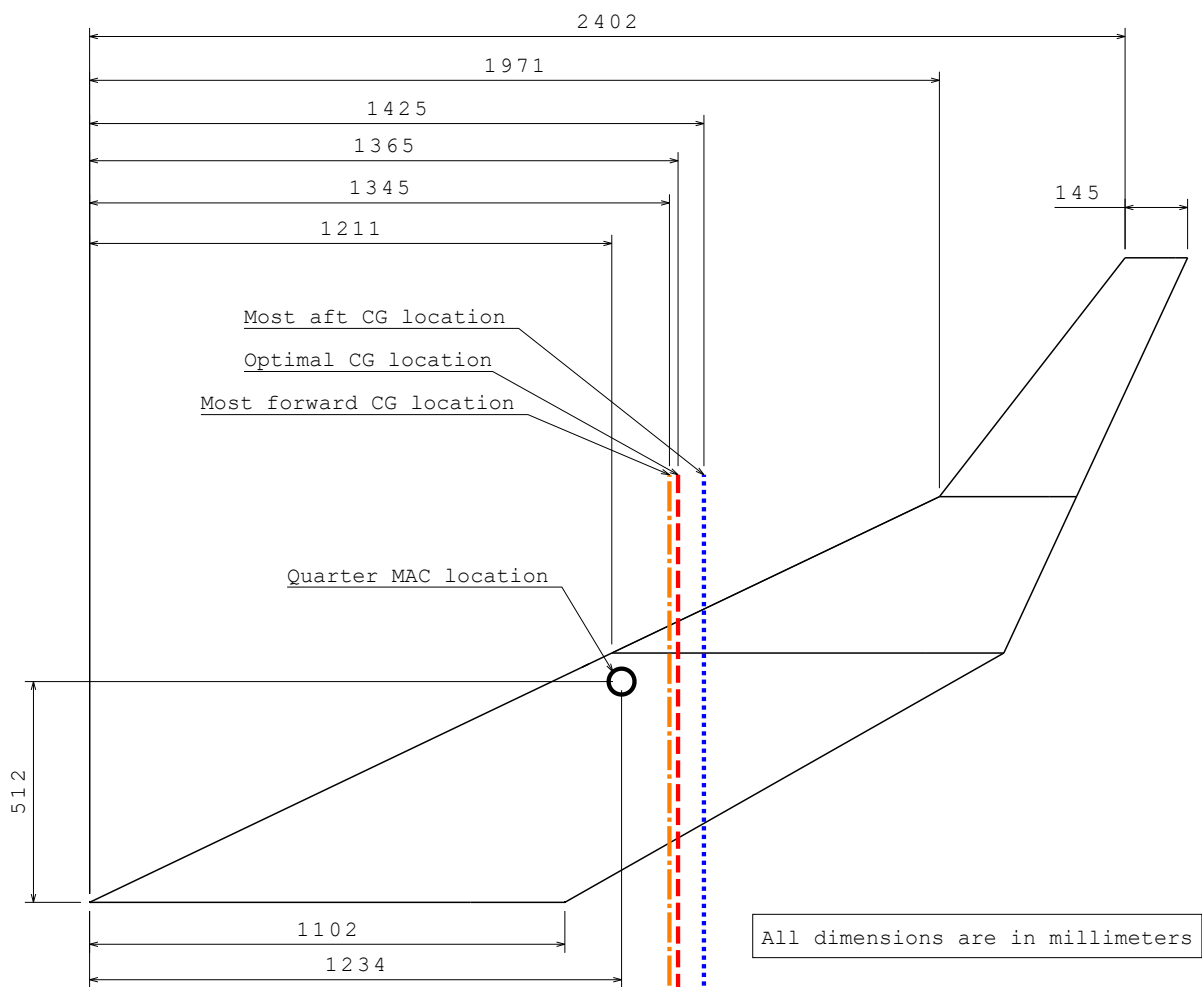


Figure 5.9: Overview of the investigated CG locations

6

Conclusions

For assessing the flight characteristics of the Flying V aircraft for approach speed and high angles of attack, three distinct wind tunnel experiments were conducted at the Open Jet Facility of the Delft University of Technology. Balance measurements showed the aircraft had an untrimmed maximum lift coefficient of 1.09 at 41 degrees angle of attack. The reason for the high angle of attack at maximum lift may be explained by the blunt leading edge and the very highly swept wing of the Flying V. Investigations into the pitching moment concluded the stability derivative is negative up to 20 degrees angle of attack, measured at the quarter mean aerodynamic chord. The neutral point was estimated at around 1.430 meters behind the nose.

The results from the oil flow and tuft visualisation experiments showed that a combination of cross-flow, attachment and separation lines on the surface of the wing indicated that from eleven degrees angle of attack onward, a leading edge separated vortex was spreading from the leading edge kink over the wingtip. From thirteen degrees angle of attack onward, the formation a set of vortices over the main part of the wing from the direction of the root towards the wingtip confirmed the vortex lift behaviour observed in the balance measurements. From 22 degrees angle of attack onward, the vortices over the main part of the wing formed a stable leading edge vortex, which was present from this angle of attack onward. Smoke visualisations confirmed that outside the boundary layer large vortices were indeed rolling over the surface of the wing.

An investigation into the trimmed flight of the aircraft showed that due to trim limitations the centre of gravity location is bound between 1.345 and 1.425 meters behind the nose. Taking the trim and pitch during approach into account, the centre of gravity is optimal to be put at 1.365 meters behind the nose, resulting in a static margin of about 9%. This way, the aircraft could be trimmed, while it has pitch control at all angles of attack as well. By taking the optimal centre of gravity location into account, during flight with a speed of thirty five meters per second the trimmed angle of attack was estimated at 3.6 degrees, which is about 22% lower compared to the untrimmed angle of attack.

The stall speed for trimmed flight is estimated at 14.8 meters per second at an angle of attack of 28.5 degrees, which corresponds to a maximum lift coefficient of 0.98 and is directly the limit of the control surface deflections for trimmed flight. At the angle where the stability derivative switches from negative into positive at 20 degrees angle of attack, the flight speed is estimated at 17.2 meters per second at the lift coefficient of 0.73. This is seen as the 'safe' stall speed due to the switch from positive into negative static stability. Taking the regulations from the FAA and ICAO for approach into account, the approach speed is, based on the absolute stall speed, estimated to be 19.2 meters per second at an angle of attack of 15.9 degrees with a lift coefficient of 0.58.

Verification and validation of the balance data led to the conclusion that the maximum lift coefficient is estimated within a 0.72% error margin using three times the standard deviation over the second and third wind tunnel campaign. The largest deviation recorded is at ten degrees angle of attack, which leads to a triple standard deviation error margin of 0.043. The averaged triple standard deviation is estimated to be 0.016 over the entire angle of attack domain.

6.1. Recommendations and Future Work

While the objective of the thesis research has been completed and the research questions have been answered, additional research is required for the validation of the data acquired during the wind tunnel experiments. Moreover, additional research into the wind tunnel corrections is required, as the results will be more accurate. For the results itself, it is recommended to perform higher fidelity studies in the form of flight testing. This way, the data from the wind tunnel experiments can be set into a new light and be compared to a more realistic scenario. Since CFD was not an option for the assessment of the flight characteristics, no validation was possible for the acquired wind tunnel data.

Differences between the wind tunnel results and the flight test results are expected because of multiple reasons. First of all, the comparison between ideal flow from the wind tunnel and real flow during flight can be made. Secondly, differences will be found by the fact that the flight model features a full wingspan aircraft, while the wind tunnel model featured a half wingspan aircraft. Last of all, the wing used during the wind tunnel experiments was a simplified version of the flight model. Therefore it did not feature any engines, landing gear, winglets and other systems, which may lead to different results compared to this research.

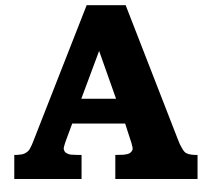
For the flight model, focus has to be put into the distribution of the weight to ensure an accurate location for the centre of gravity. Large deviations of the centre of gravity location may cause the aircraft to be unstable or untrimmable during flight. As the aerodynamic geometry of the wing is fixed in the design, the only variables into the stability and trim of the aircraft are the manufacturing and calibration of the control surfaces, the placement of the centre of gravity location and the influence of all systems on the flow over the wing. Further attention has to be put into the effect of the thrust force of the engine onto the pitching moment.

Bibliography

- [1] R. Martinez-Val, *Flying Wings. A New Paradigm for Civil Aviation?* *Acta Polytechnica* **47**, 12 (2007).
- [2] S. Ammar, C. Legros, and J.-Y. Trépanier, *Conceptual design, performance and stability analysis of a 200 passengers Blended Wing Body aircraft*, *Aerospace Science and Technology* **71**, 325 (2017).
- [3] G. Larkin and G. Coates, *A design analysis of vertical stabilisers for Blended Wing Body aircraft*, *Aerospace Science and Technology* **64**, 237 (2017).
- [4] A. L. Bolsunovsky, N. P. Buzoverya, B. I. Gurevich, V. E. Denisov, A. I. Dunaevsky, L. M. Shkadov, O. V. Sonin, A. J. Udzhuhu, and J. P. Zhurihin, *Flying wing - Problems and decisions*, *Aircraft Design* **4**, 193 (2001).
- [5] V. Denisov, L. Shkadov, and S. Chernyshev, *The Flying Wing Concept - the Challenge for the Future*, in *AIAA International Air and Space Symposium and Exposition: The Next 100 Years* (American Institute of Aeronautics and Astronautics, 2003).
- [6] R. E. Nasir, W. Kuntjoro, and W. Wisnoe, *Aerodynamic, Stability and Flying Quality Evaluation on a Small Blended Wing-body Aircraft with Canard Foreplanes*, *Procedia Technology* **15**, 783 (2014).
- [7] P. Dehpanah and A. Nejat, *The aerodynamic design evaluation of a blended-wing-body configuration*, *Aerospace Science and Technology* **43**, 96 (2015).
- [8] R. H. Liebeck, *Design of the Blended Wing Body Subsonic Transport*, *Journal of Aircraft* **41**, 10 (2004).
- [9] AGARD, *High Angle of Attack Aerodynamics*, in *AGARD Conference Proceedings No. 247* (Technical Editing and Reproduction Ltd, Sandefjord, Norway, 1978) p. 550.
- [10] J. Luckring, *A Survey of Factors Affecting Blunt-Leading-Edge Separation for Swept and Semi-Slender Wings*, in *28th AIAA Applied Aerodynamics Conference* (American Institute of Aeronautics and Astronautics, Reston, Virginia, 2010) p. 34.
- [11] C. E. Brown, *Effect of Leading-Edge Separation on the Lift of a Delta Wing*, *Journal of the Aeronautical Sciences* **21**, 690 (1954).
- [12] M. GAD-EL-HAK and R. F. BLACKWELDER, *The discrete vortices from a delta wing*, *AIAA Journal* **23**, 961 (1985).
- [13] M. Lee and C. M. Ho, *Lift Force of Delta Wings*, *Applied Mechanics Reviews* **43**, 209 (1990).
- [14] J. Benad and Airbus Operations GmbH, *a New Aircraft Configuration for Commercial Passenger Transport*, *Deutsche Gesellschaft für Luft- und Raumfahrt* , 1 (2015).
- [15] D. Stanescu, M. Hussaini, and F. Farassat, *Aircraft engine noise scattering by fuselage and wings: a computational approach*, *Journal of Sound and Vibration* **263**, 319 (2003).
- [16] M. Reshotko, J. H. Goodykoontz, and R. G. Dorsch, *Engine-Over-the-Wing Noise Research*, *Journal of Aircraft* **11**, 195 (1974).
- [17] J. Weissinger, *NACA Technical Memorandum No. 1120*, Tech. Rep. (National Advisory Committee for Aeronautics. Langley Aeronautical Lab., Langley Field, VA, United States, 1947).
- [18] F. Faggiano, R. Vos, M. Baan, and R. Van Dijk, *Aerodynamic Design of a Flying V Aircraft*, in *17th AIAA Aviation Technology, Integration, and Operations Conference* (American Institute of Aeronautics and Astronautics, Reston, Virginia, 2017) p. 25.

- [19] I. Staack and D. Lundström, *Subscale Flight Testing at Linköping University*, in *27th International Council of the Aeronautical Sciences* (2010) p. 7.
- [20] F. Faggiano, *Aerodynamic Design Optimization of a Flying V Aircraft*, Tech. Rep. (Delft University of Technology, Delft, 2016).
- [21] K. Jongkind, A. Falkmann, and H. van der Veer, *Open Jet Facility*, Present Press Publishers, 13 (n.d.).
- [22] M. Palermo, *The Longitudinal Static Stability and Control Characteristics of a Flying V Scaled Model*, Tech. Rep. (Delft University of Technology, Delft, 2019).
- [23] J. B. Barlow, W. H. Rae, and A. Pope, *Low-speed wind tunnel testing*, 3rd ed. (John Wiley & Sons Inc, New York, 1999) p. 728.
- [24] R. D. Buehrle, C. P. Young, A. W. Burner, J. S. Tripp, P. Tchong, T. D. Finley, and T. G. Popernack, *Dynamic response tests of inertial and optical wind-tunnel model attitude measurement devices*, *NASA Technical Memorandum*, 44 (1995).
- [25] C. P. Young, R. D. Buehrle, S. Balakrishna, and W. A. Kilgore, *Effects Model of Vibration on Inertial Attitude Measurement Devices*, *NASA Technical Memorandum*, 34 (1994).
- [26] H. H. Heyson, *Linearized Theory of Wind-tunnel Jet-boundary Corrections and Ground Effect for VTOL-STOL Aircraft*, *NASA-TR-R-124*, 286 (1962).
- [27] H. H. Heyson, *General Theory of Wall Interference for Static Stability Tests in Closed Rectangular Test Sections and in Ground Effect*, *NASA-TR-R-364*, L-7549, 331 (1971).
- [28] B. F. R. Ewald, *Wind tunnel wall corrections*, *AGARD-AG-336*, 560 (1998).
- [29] H. J. Alons, *OJF External Balance (NLR-CR-2008-695)*, Tech. Rep. (Nationaal Lucht- en Ruimtevaartlaboratorium, 2008).
- [30] A. Sciacchitano, W. Terra, and Y. Shah, *Aerodynamic drag determination of a full-scale cyclist mannequin from largescale PTV measurements*, in *19th international symposium on application of laser and imaging techniques to fluid mechanics* (Delft University of Technology, Delft, 2018) p. 19.
- [31] E. N. Jacobs and A. Sherman, *Airfoil Section Characteristics as Affected by Variations of the Reynolds Number (NACA-TR-586)*, Tech. Rep. (National Advisory Committee for Aeronautics. Langley Aeronautical Lab., Langley Field, VA, United States, 1937).
- [32] A. E. von Doenhoff and N. Tetervin, *Investigation of the Variation of Lift Coefficient with Reynolds Number at a Moderate Angle of Attack on a Low-Drag Airfoil*, *Confidential Bulletin*, 1 (1942).
- [33] I. H. Abbott, A. E. von Doenhoff, and L. Stivers, *Summary of Airfoil Data*, *NACA Technical Report 824*, 270 (1945).
- [34] N. Gold and K. Visser, *Aerodynamic effects of local dihedral on a raked wingtip*, in *40th AIAA Aerospace Sciences Meeting & Exhibit* (American Institute of Aeronautics and Astronautics, Reston, Virginia, 2002) p. 15.
- [35] E. Torenbeek and H. Wittenberg, in *Flight Physics: Essentials of Aeronautical Disciplines and Technology, with Historical Notes* (Springer, 2009) p. 535.
- [36] S. E. Rogers, K. Roth, H. V. Cao, J. P. Slotnick, M. Whitlock, S. M. Nash, and M. D. Baker, *Computation of Viscous Flow for a Boeing 777 Aircraft in Landing Configuration*, *Journal of Aircraft* **38**, 1060 (2001).
- [37] M. V. Cook, *Flight Dynamics Principles: A Linear Systems Approach to Aircraft Stability and Control* (Butterworth-Heinemann, 2012) p. 608.

- [38] D. A. Caughey, *Introduction to Aircraft Stability and Control Course Notes for M&AE 5070* (Cornell University, Ithaca, 2011) p. 147.
- [39] R. Vos and S. Farokhi, *Introduction to Transonic Aerodynamics*, Fluid Mechanics and Its Applications, Vol. 110 (Springer Netherlands, Dordrecht, 2015) p. 555.
- [40] S. N. Skinner and H. Zare-Behtash, *Semi-span wind tunnel testing without conventional peniche*, *Experiments in Fluids* **58**, 163 (2017).
- [41] S. A. Glazkov, A. R. Gorbushin, I. A. Kursakov, and K. A. Yassenok, *Investigation of the influence of peniche and flow boundaries on the flow around a half-model using CFD simulation*, in *AIP Conference Proceedings*, Vol. 1770 (2016) p. 030010.
- [42] A. M. O. Smith, *High-Lift Aerodynamics*, *Journal of Aircraft* **12**, 501 (1975).
- [43] C. J. Obara and J. E. Lamar, *Overview of the Cranked-Arrow Wing Aerodynamics Project International*, *Journal of Aircraft* **46**, 355 (2009).
- [44] S. Watanabe, H. Kato, D. Y. Kwak, M. Shirotake, and K. Rinoie, *Stereoscopic PIV measurements of leading edge separation vortices on a cranked arrow wing*, *Measurement Science and Technology* **15**, 1079 (2004).
- [45] D. Y. Kwak, M. Shirotake, and K. Rinoie, *Vortex Behaviors over a Cranked Arrow Wing Configuration at High Angles of Attack*, *24th International Congress of the Aeronautical Sciences*, 10 (2004).
- [46] K. Hirai, D. Y. Kwak, and K. Rinoie, *Vortex Behaviors of Cranked Arrow Wing Configurations With Different Wing Planforms*, *26th International Congress of the Aeronautical Sciences*, 18 (2008).
- [47] R. Lock and E. Rogers, *Aerodynamic Design of Swept Wings and Bodies for Transonic Speeds*, in *Advances in Aeronautical Sciences* (Elsevier, 1962) pp. 253–275.
- [48] H. Pearcey, *the Aerodynamic Design of Section Shapes for Swept Wings*, in *Advances in Aeronautical Sciences* (Elsevier, 1962) pp. 277–322.
- [49] M. J. Hemsch and J. Luckring, *Connection between leading-edge sweep, vortex lift, and vortex strength for delta wings*, *Journal of Aircraft* **27**, 473 (1990).
- [50] J. Bartasevicius, A. Buzica, and C. Breitsamter, *Discrete vortices on delta wings with unsteady leading-edge blowing*, in *8th AIAA Flow Control Conference* (American Institute of Aeronautics and Astronautics, Reston, Virginia, 2016) p. 15.
- [51] International Civil Aviation Organization, *Doc 8168 OPS/611 Aircraft Operations Volume I - Flight Procedures*, in *Aircraft Operations*, Vol. I (2006) p. 279.
- [52] Federal Aviation Administration, *Airplane Flying Handbook (FAA-H-8083-3B)* (United States Department of Transportation, Federal Aviation Administration, Airman Testing Standards Branch, Oklahoma City, 2016) p. 348.



Original Oil Flow Visualisation Pictures

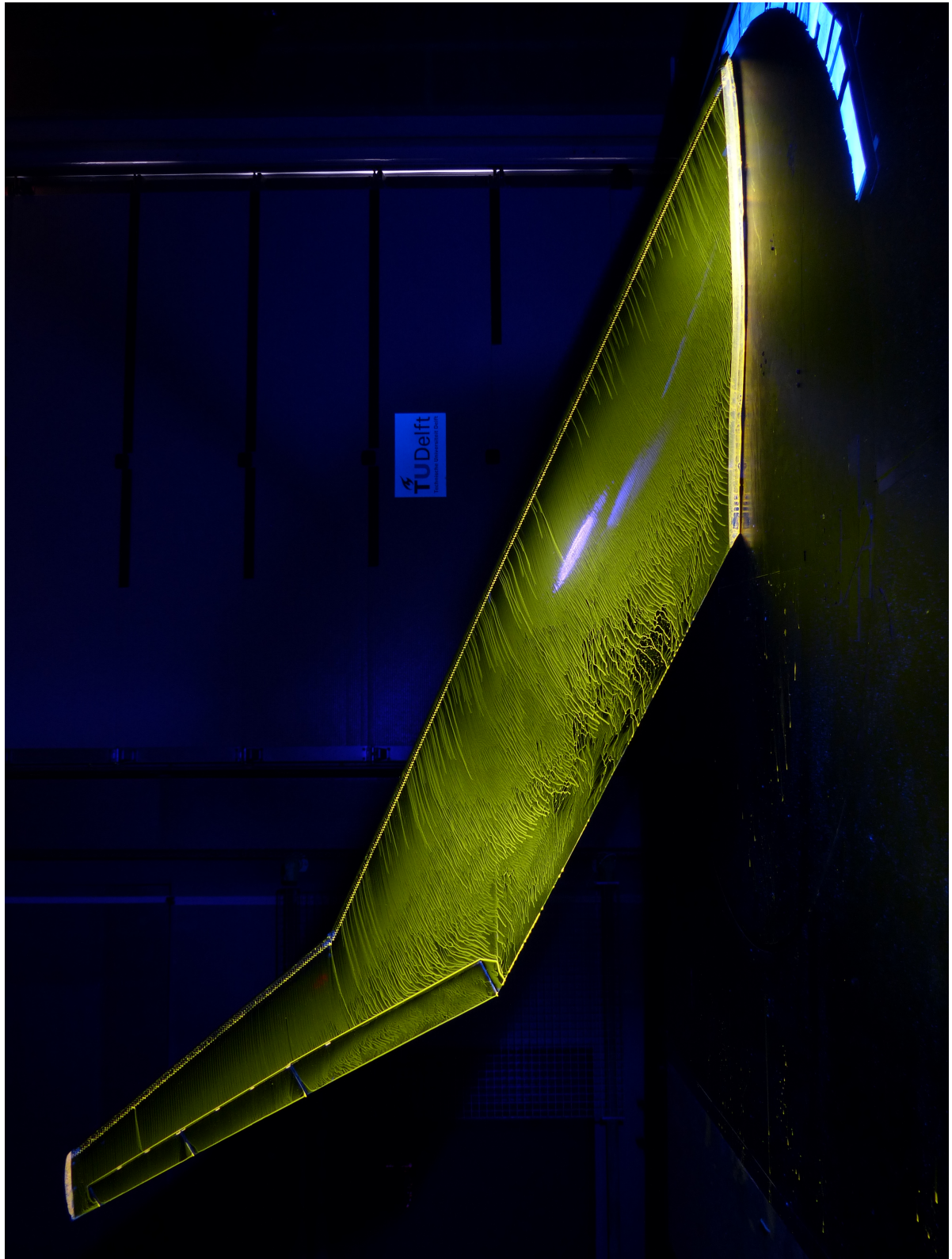


Figure A.1: Oil flow visualisation at 5 degrees angle of attack



Figure A.2: Oil flow visualisation at 7 degrees angle of attack



Figure A.3: Oil flow visualisation at 9 degrees angle of attack



Figure A.4: Oil flow visualisation at 11 degrees angle of attack



Figure A.5: Oil flow visualisation at 13 degrees angle of attack



Figure A.6: Oil flow visualisation at 15 degrees angle of attack

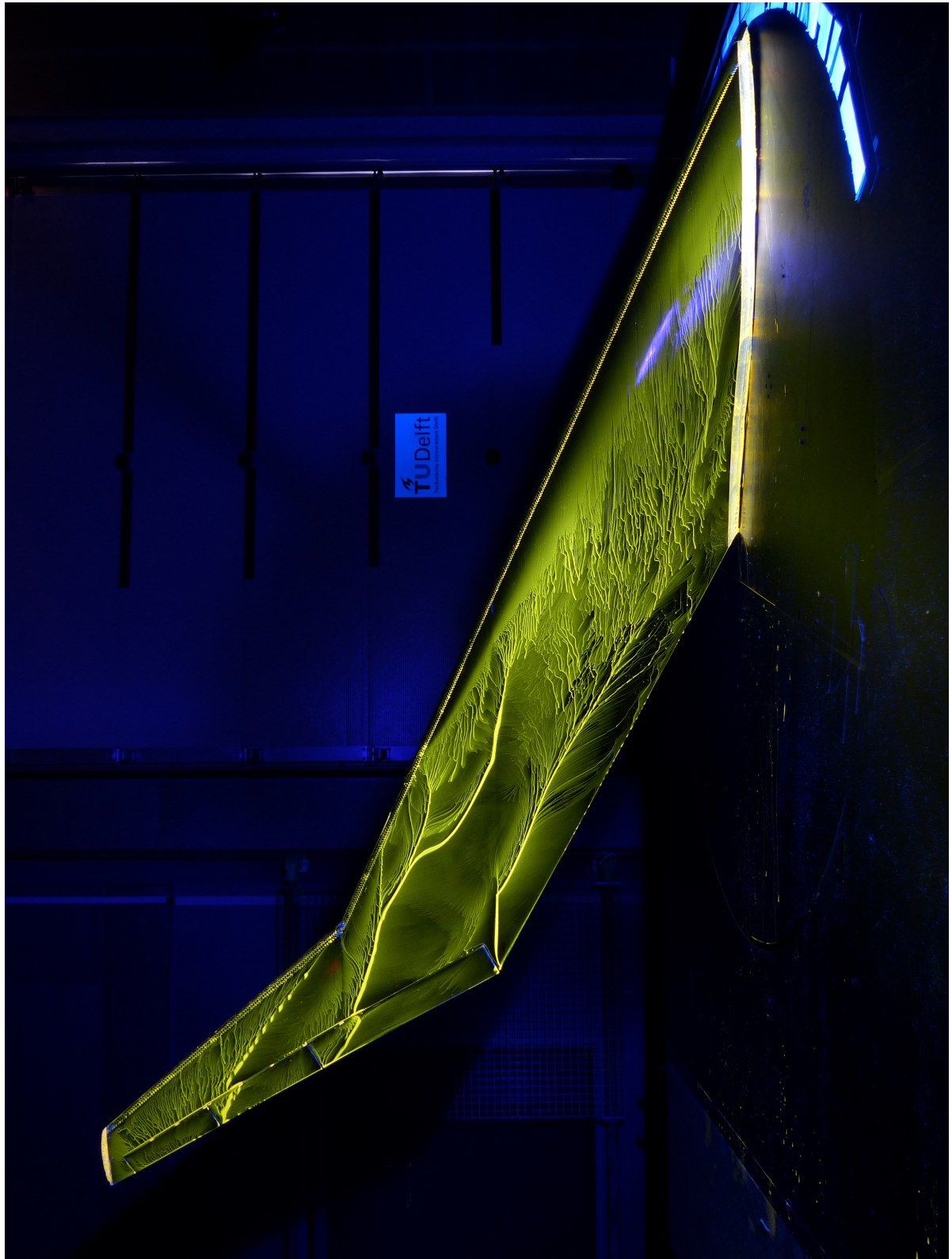


Figure A.7: Oil flow visualisation at 17 degrees angle of attack

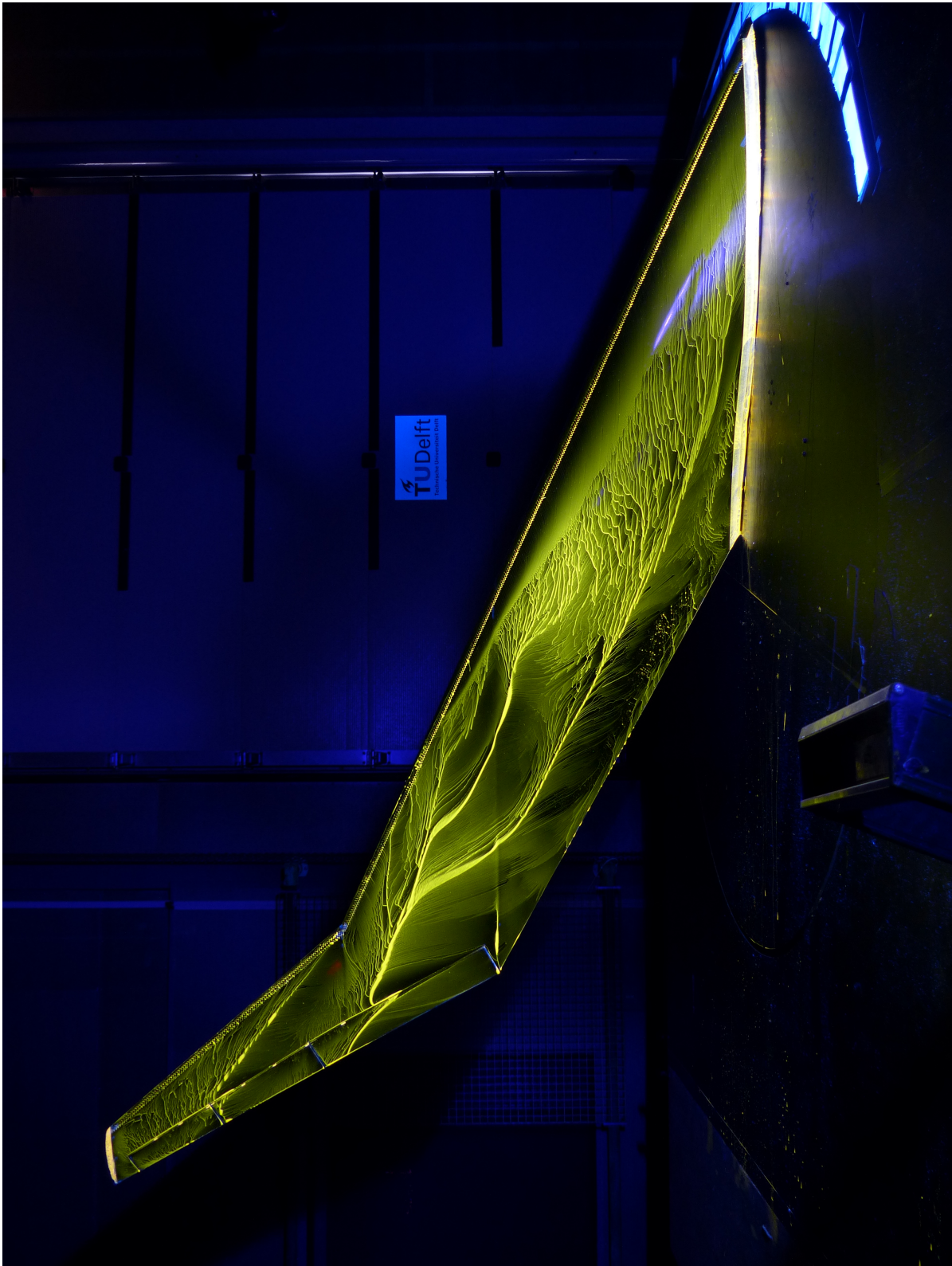


Figure A.8: Oil flow visualisation at 19 degrees angle of attack

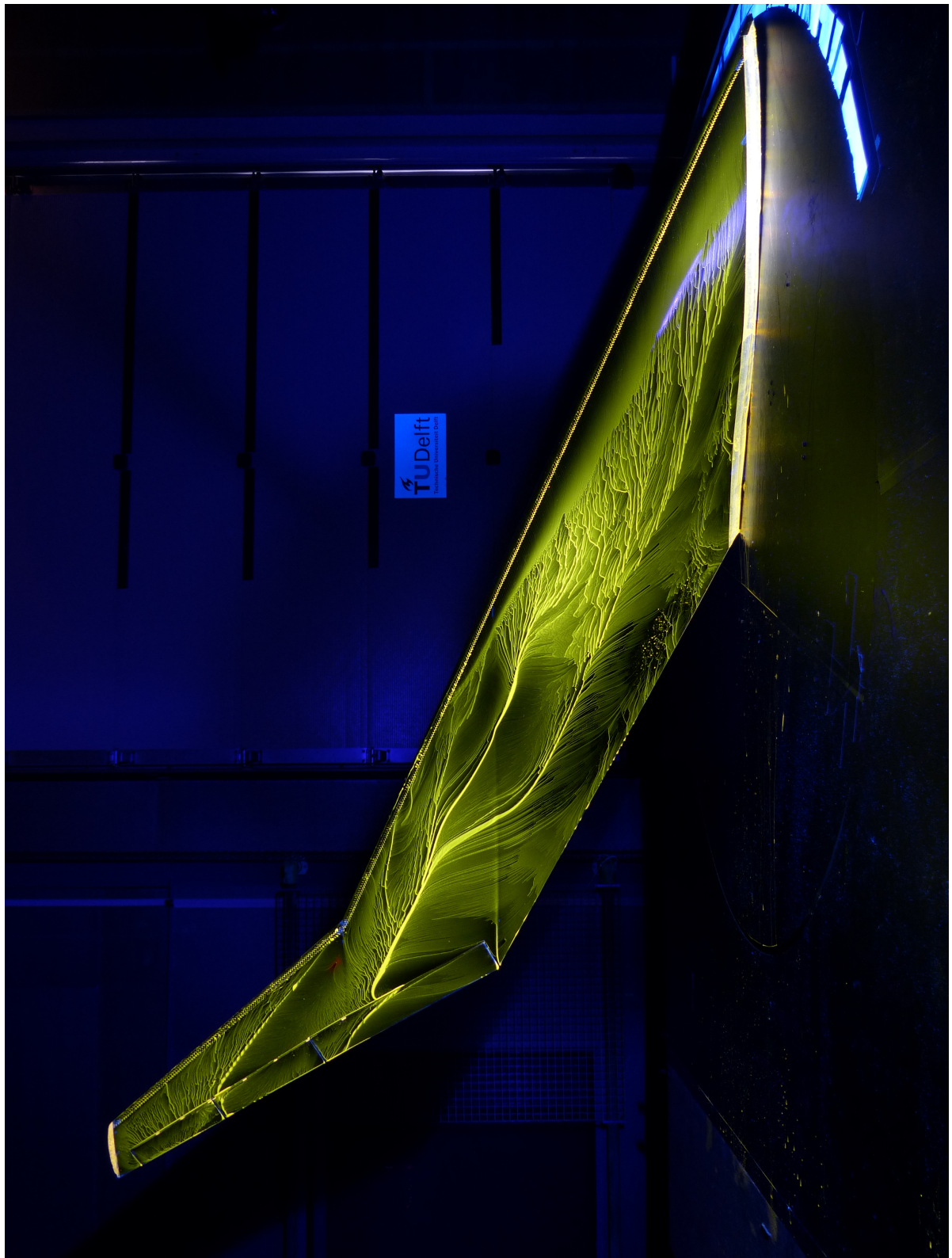


Figure A.9: Oil flow visualisation at 20 degrees angle of attack



Figure A.10: Oil flow visualisation at 21 degrees angle of attack

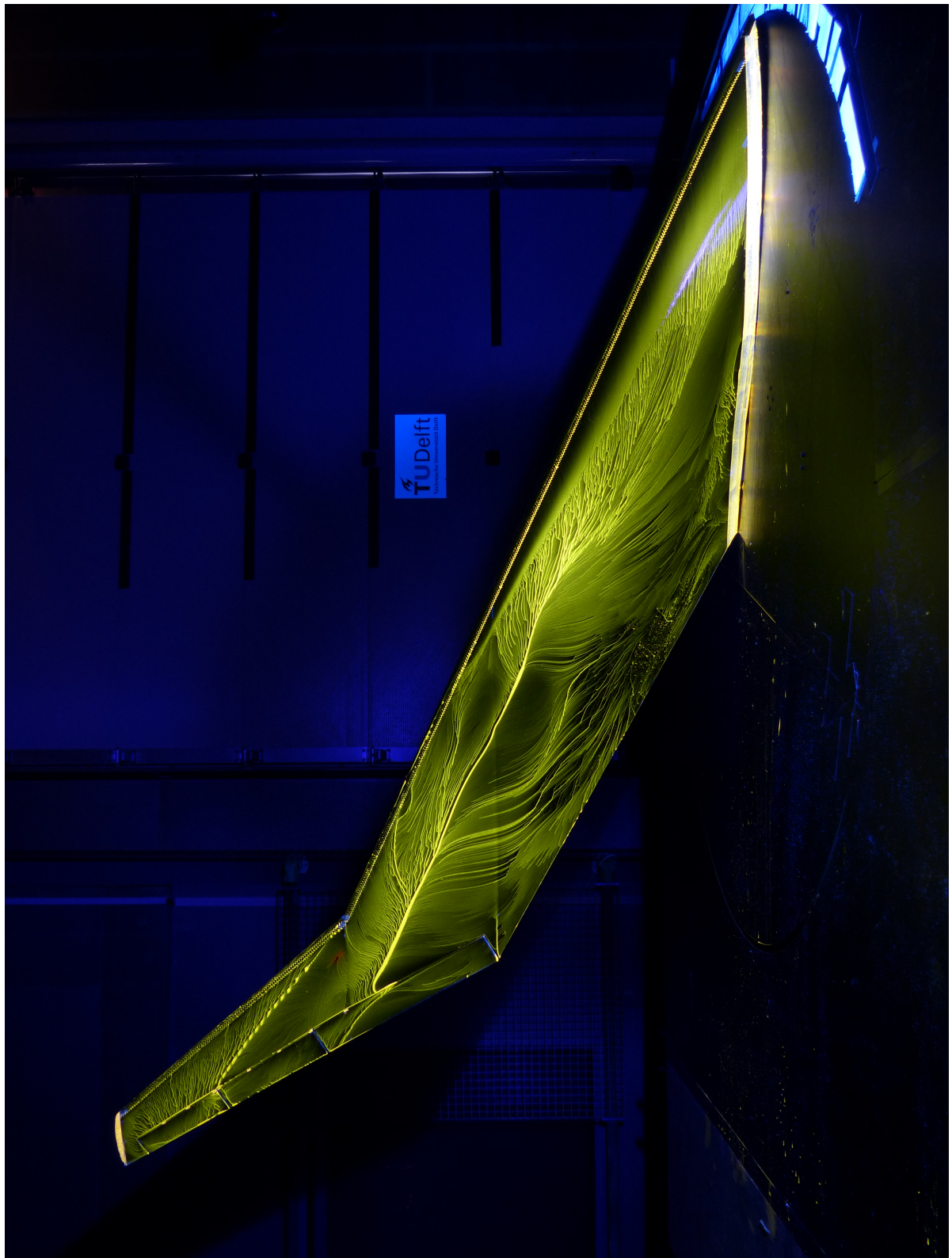


Figure A.11: Oil flow visualisation at 22 degrees angle of attack



Figure A.12: Oil flow visualisation at 23 degrees angle of attack

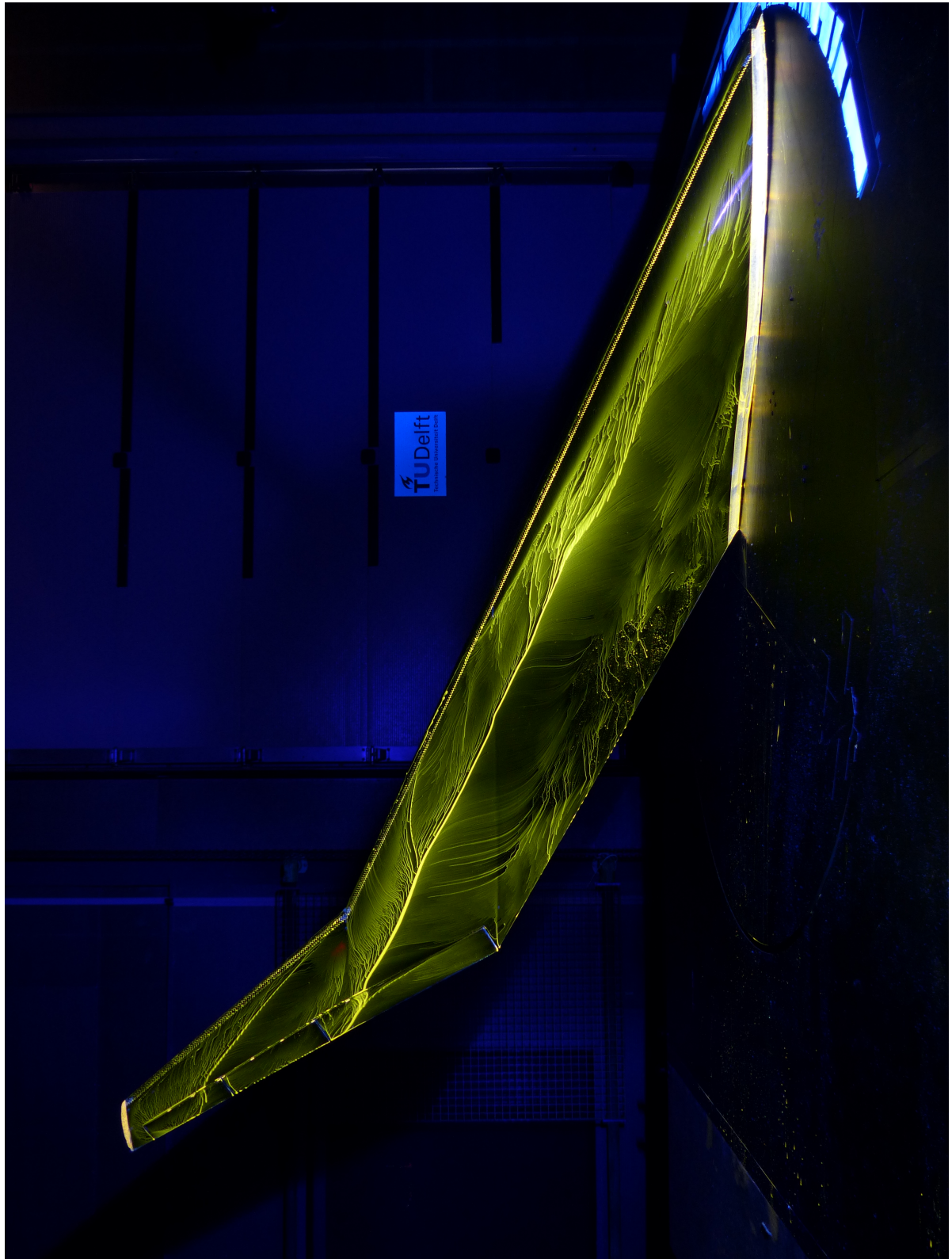


Figure A.13: Oil flow visualisation at 25 degrees angle of attack

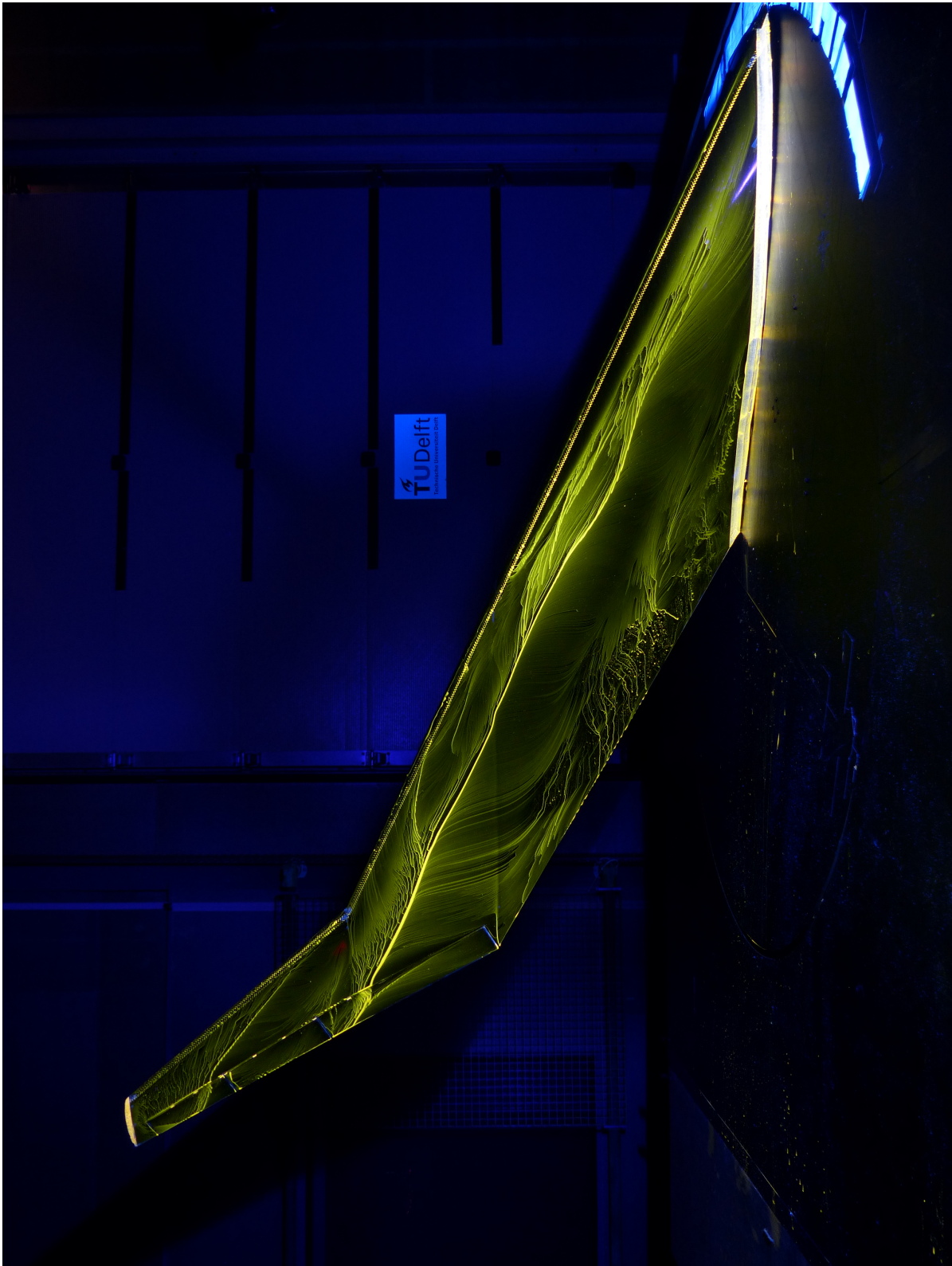


Figure A.14: Oil flow visualisation at 27 degrees angle of attack

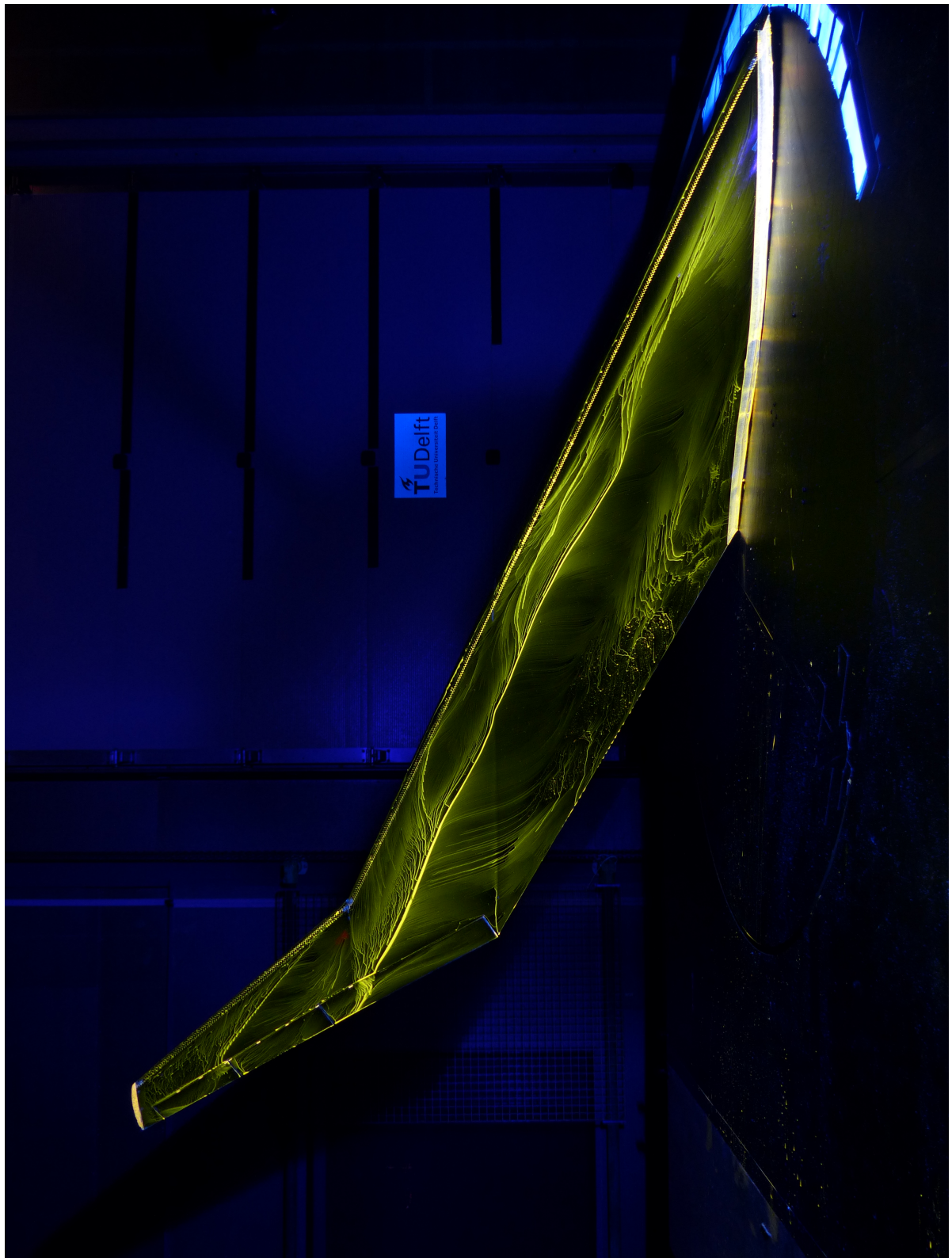


Figure A.15: Oil flow visualisation at 29 degrees angle of attack

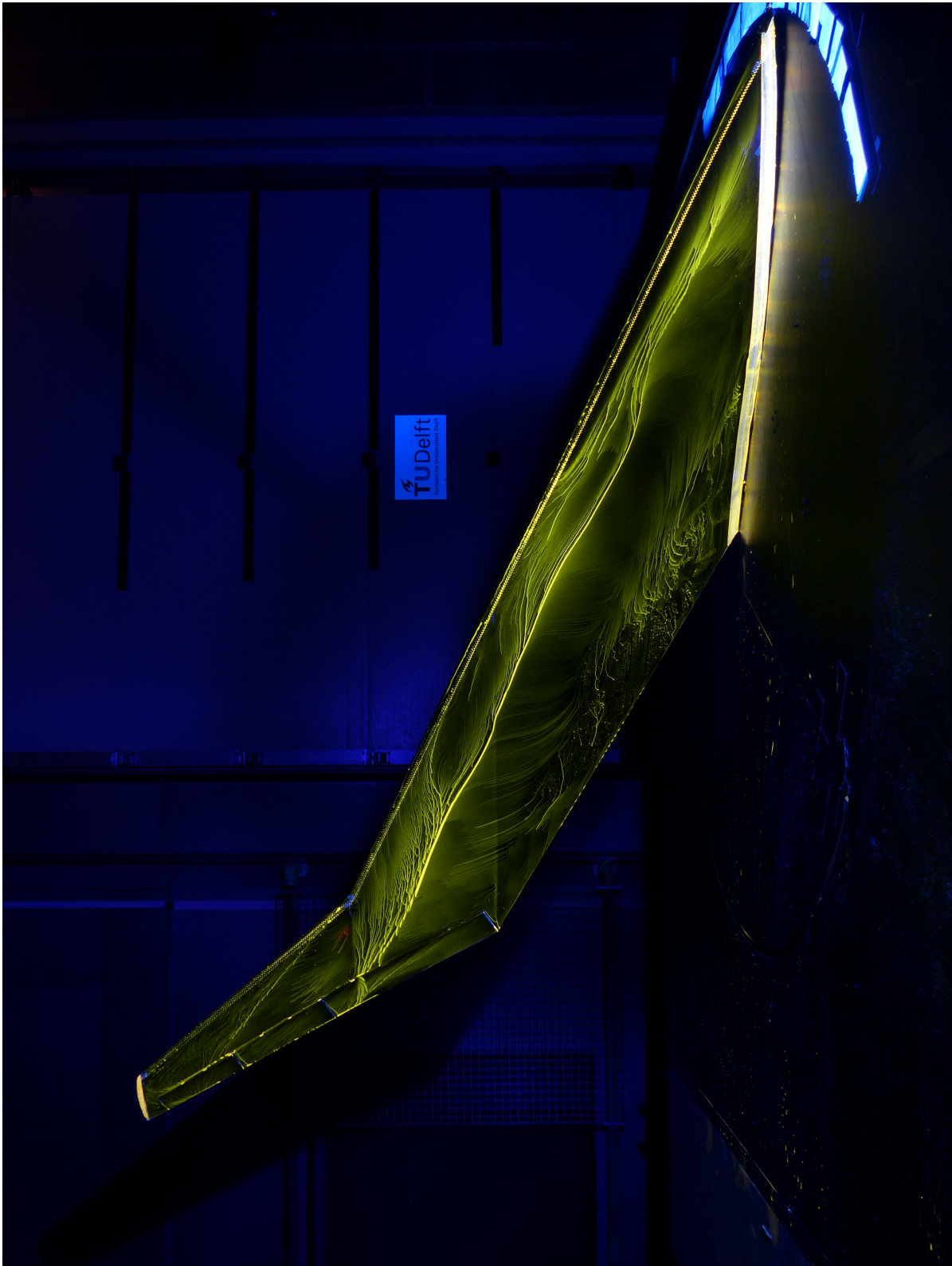


Figure A.16: Oil flow visualisation at 31 degrees angle of attack

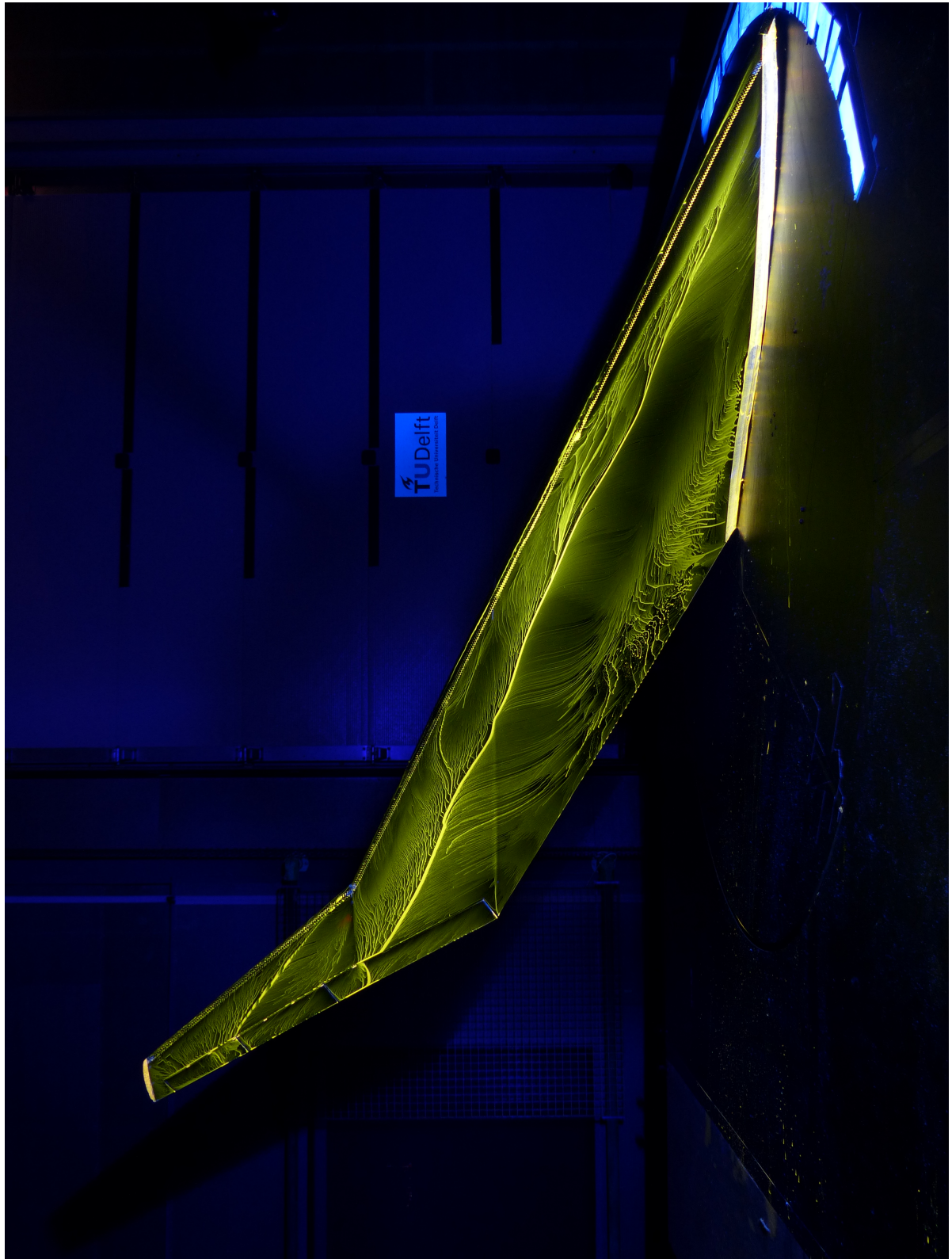


Figure A.17: Oil flow visualisation at 33 degrees angle of attack



Figure A.18: Oil flow visualisation at 35 degrees angle of attack

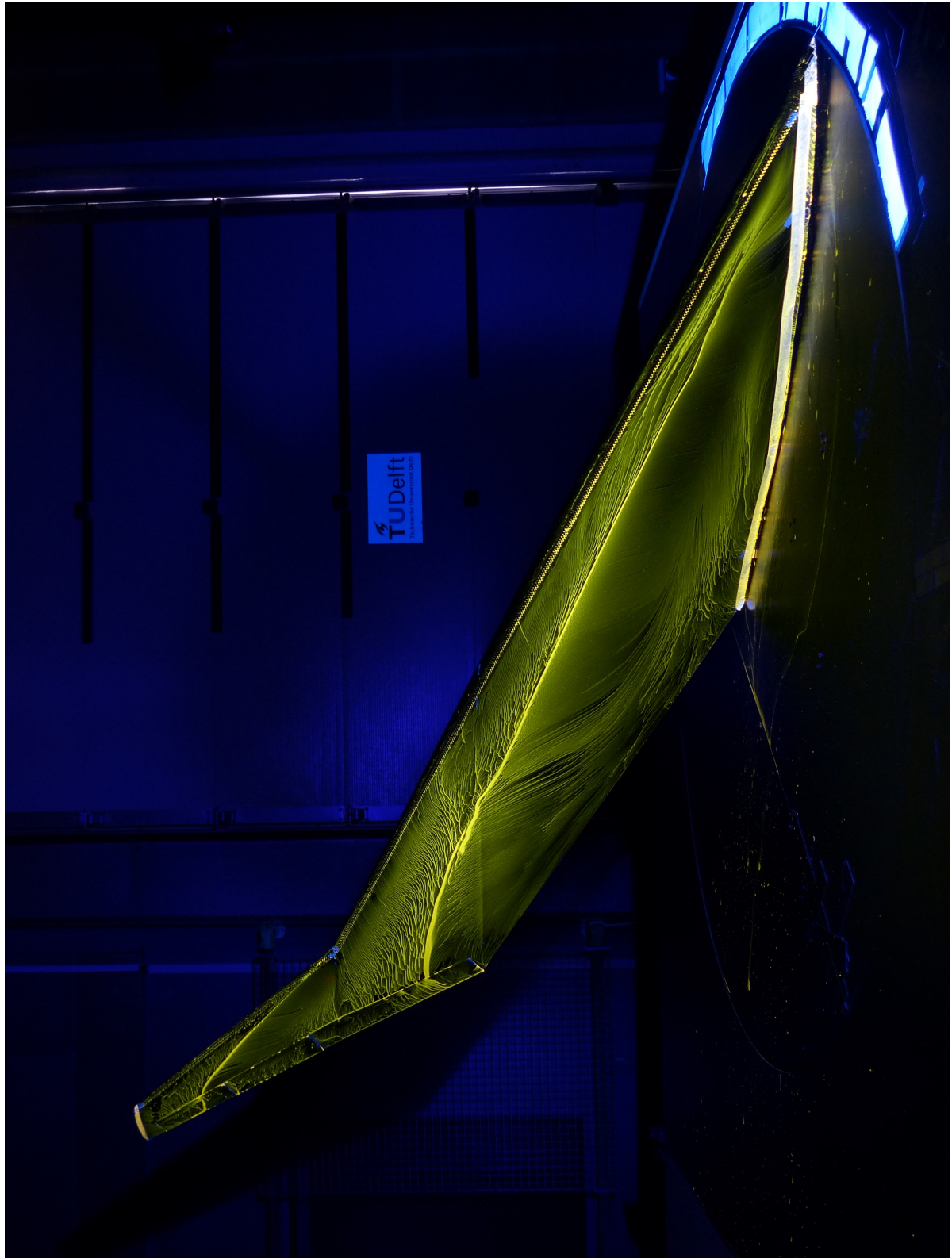


Figure A.19: Oil flow visualisation at 41 degrees angle of attack



Figure A.20: Oil flow visualisation at 50 degrees angle of attack

B

Additional Moment Curve Figures

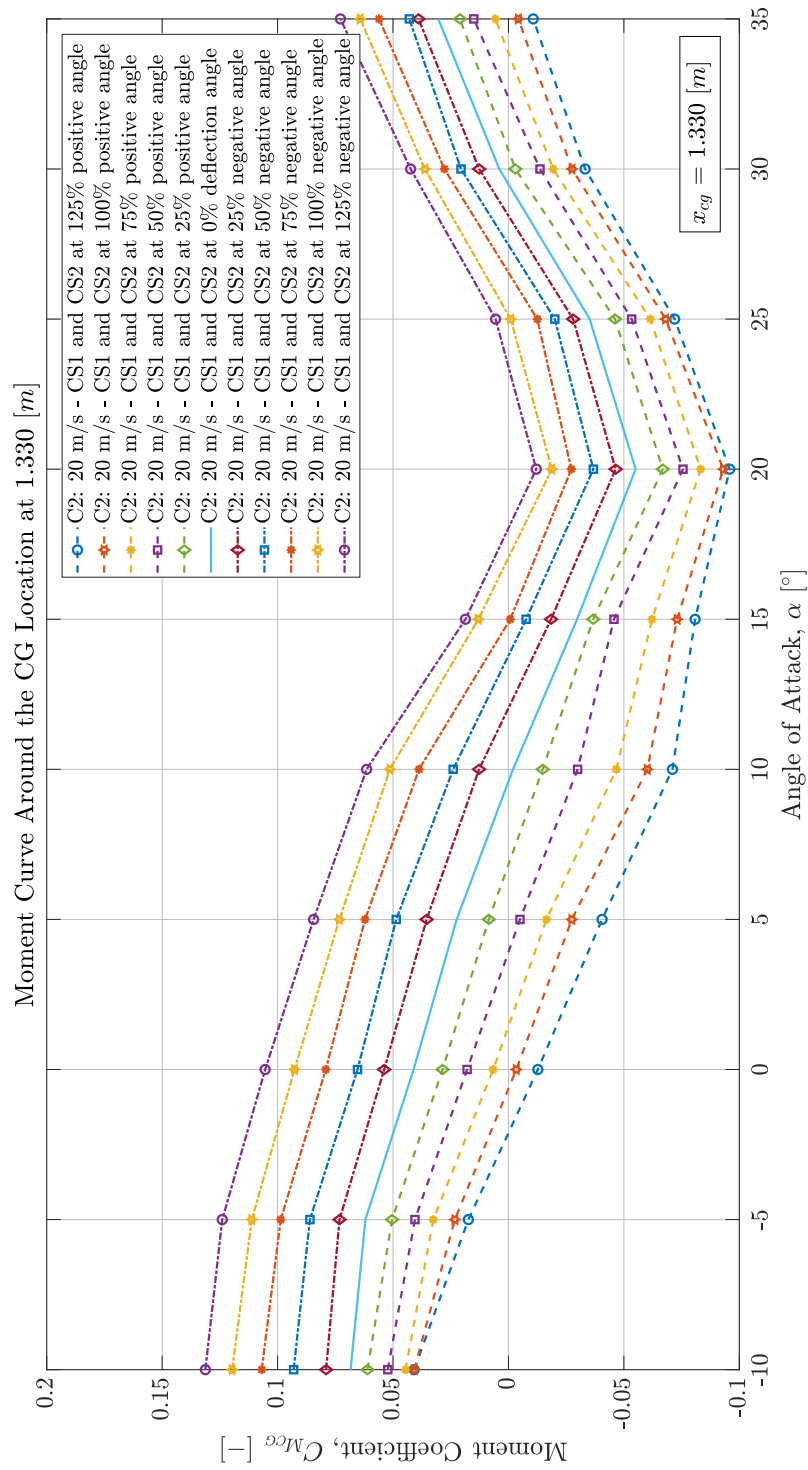


Figure B.1: Moment coefficient comparison for the control surface deflections with the CG at 1.330 meters behind the nose

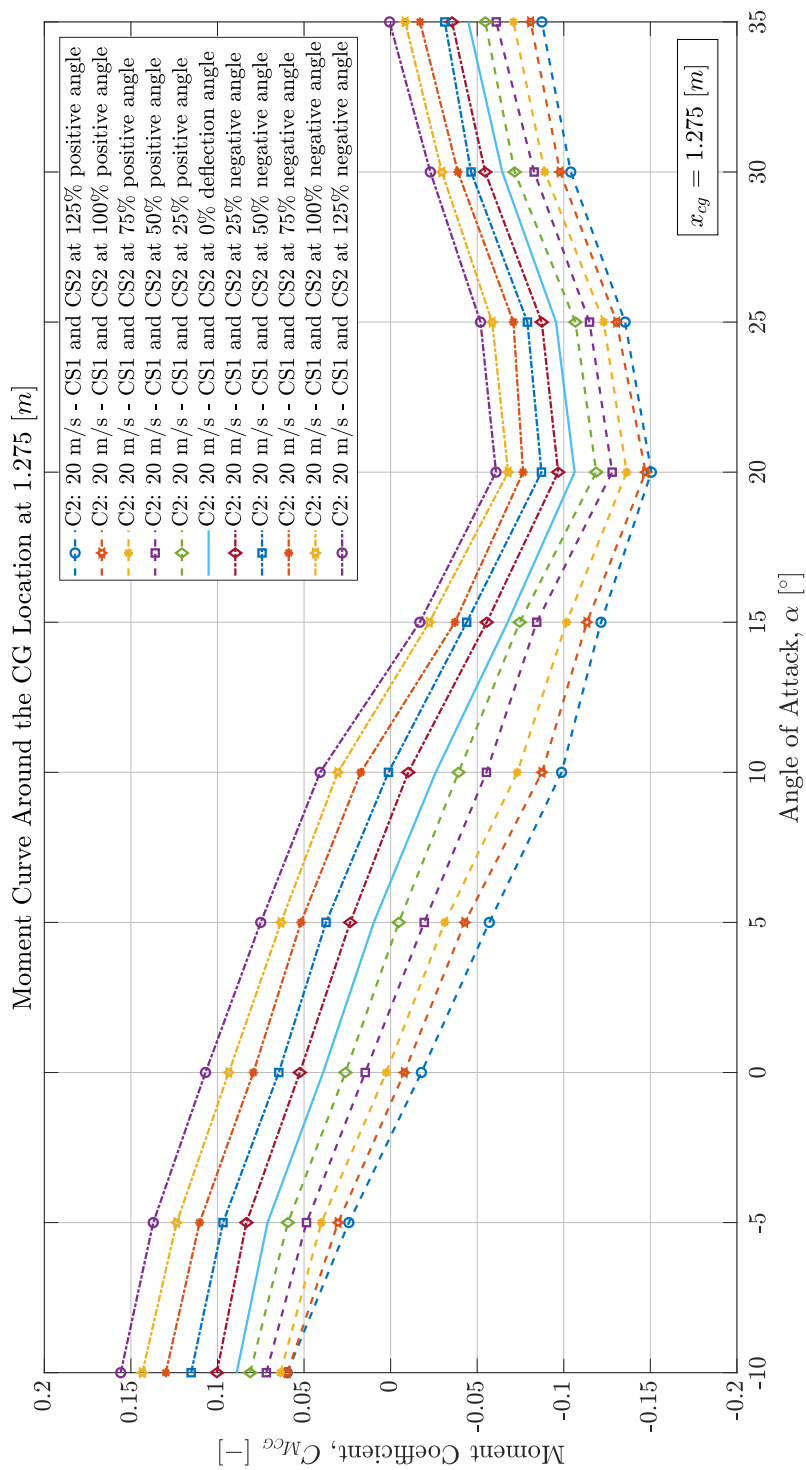


Figure B.2: Moment coefficient comparison for the control surface deflections with the CG at 1.275 meters behind the nose

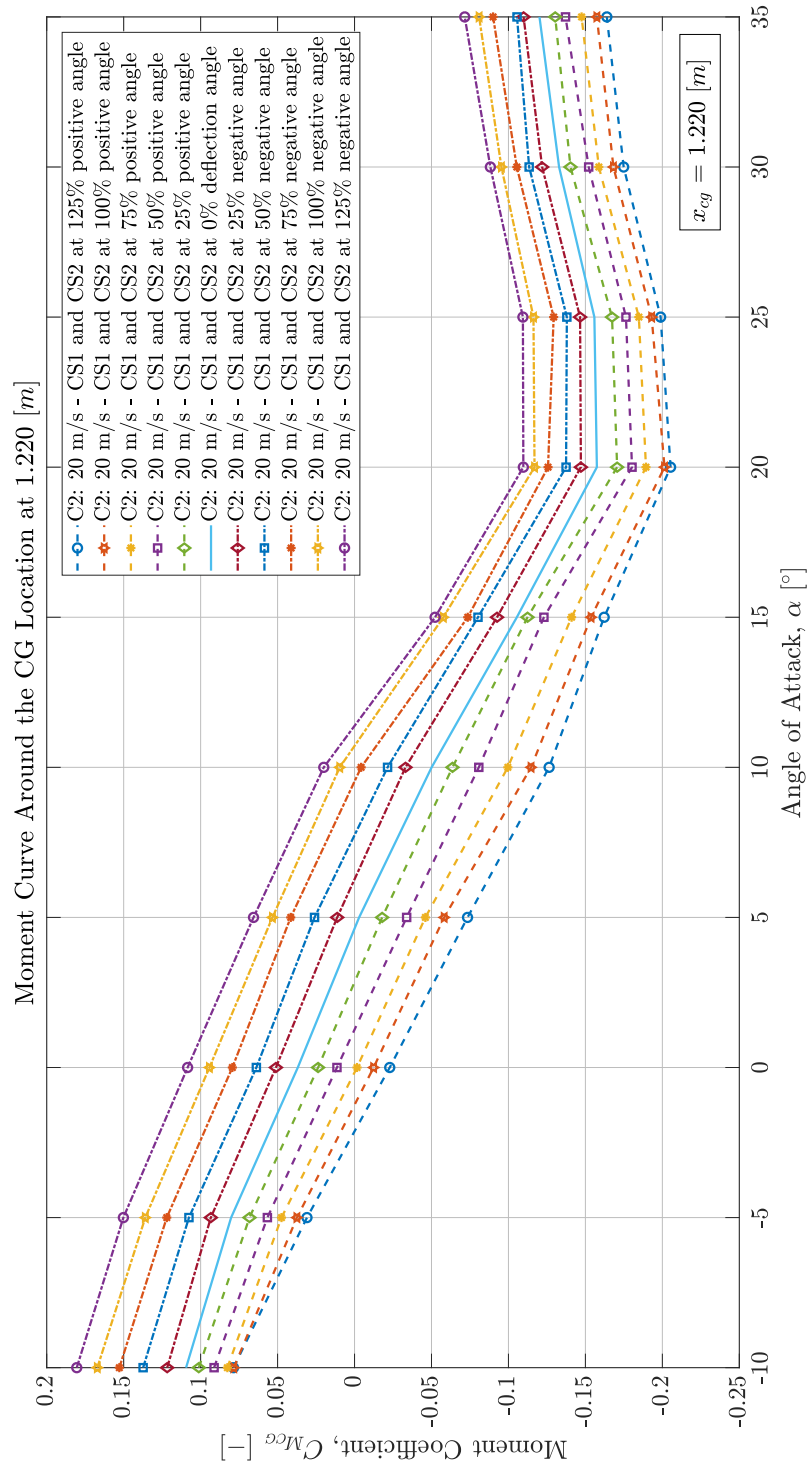


Figure B.3: Moment coefficient comparison for the control surface deflections with the CG at 1.220 meters behind the nose